UNIVERSITÀ DI PISA

Dipartimento di Fisica "E. Fermi"

Corso di Laurea Magistrale in Fisica

Elaborato finale

Confronting Degenerates: a panchromatic study of the recurrent nova T Pyxidis 2011 and the ONe γ-ray emitting V959 Monocerotis 2012

Candidato
Ivan De Gennaro Aquino

Relatore
Prof. Steven N. Shore

Anno Accademico 2012/2013

Abstract

Novae are violent explosions occurring on the surface of a white dwarf accreting material from a close companion, in binary stellar systems called *cataclysmic variables*.

Hydrogen-rich gas from the donor star accretes onto and mixes within the envelope of an electron degenerate star, a white dwarf (WD). With increasing pressure and temperature, a threshold can be reached at which proton capture on CNO nuclei ignites a thermonuclear reaction. This release of energy increases the temperature but, because of the degenerate environment, the pressure is not altered by expansion fro the overpressure. Eventually a thermonuclear runaway occurs, reaction rates go out of equilibrium, the envelope expands and the explosion throttles and stalls. Due to high temperature gradients, convective macro-scale motions mix the expanding envelope with the superficial layers of the WD. Expansion is finally driven by β-unstable nuclides, mainly CNO isotopes.

The photometric and spectroscopic evolution of the outburst is determined by the physical conditions and dynamics of the ejected envelope. Initially completely ionized and opaque, the freely expanding gas is continuously irradiated by the central hot WD: the luminosity finally reaches the Eddington limit. Once recombination becomes efficient, line absorption from metals becomes the main opacity source. The envelope steadily rarefies, eventually turning transparent, showing broad ($\sim 10^3\, km\, s^{-1}$) emission lines profiles.

Although these explosions release several orders of magnitude less energy (mass) than supernovae, the physical processes taking place deserve full attention. The complete modeling and comprehension of the outburst is a difficult task given the relevant number of parameters involved (the detailed properties of the WD and its companion, the orbital parameters of the system etc), and computational limits on three-dimensional models. However, with panchromatic high-cadence observations it is possible to build a solid evolutionary model for the outburst.

Among the hundreds (and counting) known novae in the Milky Way, only 10 are known to be *recurrent*: these novae have displayed two or more outbursts in the last $\sim$150 years. One of these systems, T Pyxidis, which sixth historical outburst occurred in April 2011, has been studied for this thesis. The analysis follows the evolutionary path of the nova from the early stage of the outburst to the late *nebular* phase (December 2012). The spectroscopic analysis suggests a bipolar geometry for the ejecta, a feature which seems omnipresent for classical and recurrent novae. The study of the interstellar medium along the line of sight has also been conducted.

The WD composition is determined by the evolutionary history of the star: naively, more massive stars develop oxygen-neon rich cores, instead of carbon-nitrogen-oxygen, hence defining two subclasses, *ONe* and *CO* novae. Nova Monocerotis 2012 (V959 Mon), a recent ONe nova, is discussed here. It is the first classical nova discovered as high-energy γ-ray source before optical discovery. The comparison with past ONe novae strongly supports the hypothesis of a specific evolutionary sequence for these objects, perhaps also a new candidate class of cosmologically significant standard candles.

The analysis for these novae has been conducted with multi-wavelength observations (from γ-rays to infrared) and archival data for comparisons with historical analogs.

The discussion concerns the hydrodynamic and evolutionary processes that are peculiar to this class of cataclysmic variables, their possible relation to supernovae Type Ia, and their importance as laboratories for processes encountered in other areas of astrophysics. The results of the analysis are discussed in the light of several aspects of the phenomenon currently under investigation, particularly radiative/dynamical processes taking place during the optically thick stage, and the maximum magnitude vs distance relation.

Saverio: *Lo sciaquone è un mistero, perché va via l'acqua poi ritorna da sè.*
Mario: *'Nu mistero, llà ci sarà 'nu sistema, comunicanti, vasi...*
Saverio: *C'è un sistema, anche nella lampadina c'è il sistema...*
Mario: *Ma llà è facile, è meccanico! L'acqua va via e altra acqua pij' 'o posto 'e chell'acqua...*
Saverio: *Lo sai fare o non lo sai fare?*
Mario: *'O sciaquone?*
Saverio: *Eh!*
Mario: *No. Cioè per adesso no, si m' c' mett' 'o riesco a ffà.*

Non ci resta che piangere - 1984 - Roberto Benigni & Massimo Troisi.

Un ringraziamento a tutti gli amici e colleghi,
in qualsiasi punto dello spazio-tempo voi siate.
Un caro saluto ai miei parenti, specialmente alle nonne.
Un "grazie!" speciale ad Ivana, Luigi e Matteo.
So long, Steve, and thanks for all the physics!
Un abbraccio alla mia famiglia, Luca, mamma e papà.
Un bacio a Roberta.

Contents

Chapter 1

Introduction

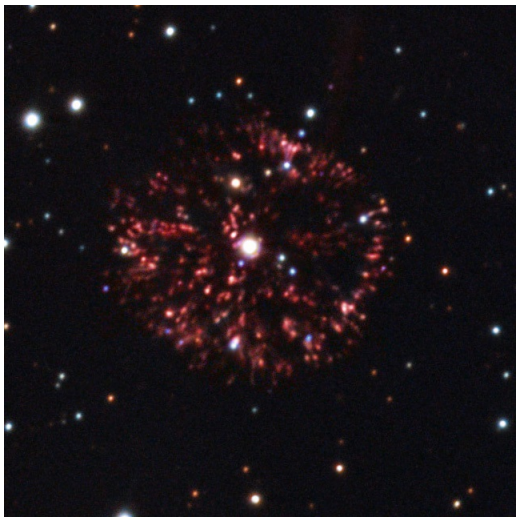

Figure 1.1: Nova GK Persei 1901 remnants, photographed at Mount Lemmon SkyCenter, 2011.

The name nova originates from the Latin words “stella nova” which means new star. Amongst the most notable definitions, Newton’s one (1726) elegantly sums up the phenomenon:

> *Hujus generis sunt stellae fixae, quae subito apparent, et sub initio quam maxime splendent, et subinde paulatim evanescunt*
>
> Of this kind are such fixed stars as appear on a sudden, and shine with a wonderful brightness-bat first, and after vanish by little and little.

Until the second decade of the twentieth century, there wasn’t any clear difference between novae, supernovae and other cataclysmic variables (CVs). In early 1920s, Curtis and other differentiated common variables and novae from supernovae, which were recognized to be much more energetic event. Amongst CVs, novae weren’t clearly distinguished from the other variables, even tough the basic phenomenology of the event was known at the time, as announced by Hartmann: *”Nova-Problem gelöst. Stern bläht sich auf, zerplatzt.”* (1925, *Astr.Nach.*, 226, 63), i.e. "Nova-problem solved. Star expands (fig. 1.1 for a notable example), and bursts"; this enthusiastic announcment was then followed by a detailed analysis of nova RR Pictoris (Hartmann, 1926).

A fundamental discovery for CVs was the binary nature of AE Aqr by Joy (1943), subsequently confirmed for nova DQ Her by Walker (1954), when became clear the presence of a compact object within the system. One of the most important comprehensive work on galactic novae was conducted by Payne-Gaposchkin (1957), who definitely refined the *speed class* parametrization still used nowadays: from the light curve decay

times t_2 and t_3, the times to decay by 2 and 3 magnitude respectively, novae can be *fast*, *slow* and so on. During the 1940s, McLaughlin (1942) established the spectral evolution scheme, then refined by Payne-Gaposchkin, that describes the changes taking place in novae spectra from the maximum of the light curve to quiescence state. There was already evidence for remarkable spectral differences for some novae, especially for the strength of [Ne III] 3869, 3968 Å lines.

The importance of runaway nuclear reactions as main cause for the explosion was firstly caught by Schatzman (1951). With Kraft and Paczynski hypothesis of hydrogen burning on the WD surface and the first numerical work during the 1960s, the modern picture of novae was ultimately defined. For a complete and detailed historical overview, see Duerbeck (2008).

In the modern picture, *classical novae* (CN) are explosive mass ejection events triggered by the ignition of a thermonuclear runaway on the surface of an accreting white dwarf (WD) under degenerate conditions. The accretion process occurs due to a close companion star that filled its Roche-lobe, so that material can flow through the inner Lagrangian point into the WD's lobe. Unlike Supernovae Type Ia, a similar scenario where a WD close to the Chandrasekhar limit is completely destroyed in the explosion, the nova event is non-disruptive, leading to a repetitive phenomenon, a *recurrent nova* (RN). Observationally, they are characterized by an increase in brightness, from 8 to 18 magnitudes, occurring in few days and a decaying phase to quiescence state lasting weeks or months. Even tough all novae share the same astrophysical origin (chapter 2) and present a common spectral evolution (chapter 3), it's fundamental to investigate the small differences between each object to properly understand the physical conditions and mechanisms of the phenomenon.

These cosmic explosions have caught the interest of astronomers and astrophysicists for more than a century. The complete description of these objects needs a deep knowledge of all the physical processes involved: nuclear physics, with the never ending requirement of precise nuclear cross sections; hydrodynamics and combustion theory, to describe the evolution of the explosion; atomic physics and radiative transfer, to analyze and understand the observations, from X-ray to radio wavelengths; chemistry, being novae known producers of molecules and dust. Everything sets in the great context of stellar physics. All these processes together leave their signatures in the spectrum: this is the reason to emphasize the multi-wavelength analysis, because what we see in a particular region of the spectrum is tightly, physically linked to the other. Novae are extremely good "experiments" for testing our knowledges, but different techniques have been developed to study them: 3D simulations, detailed atmospheric models, photoionization codes etc.

Today, the general picture of the phenomenon is well understood, but many details still need a comprehensive description, and from specific problems, which at first sight may seem related only for these "little" (when compared to supernovae or GRBs) explosions, we are actually questioning general astrophysical problems, found in many different contexts. Moreover, the advancements in astronomy, with new techniques and instruments, will always show unexpected features or completely new processes.

In this work, I summarize the nova phenomenon, its progenitor physical properties and outburst evolution, and finally report the analysis, mainly conducted with optical and ultraviolet observations, on two recent novae. The first is T Pyxidis (chapter 4), a recurrent nova, which sixth known outburst occurred in April 2011: the analysis reported here is included in Shore et al. (2013a), for which I collaborated, and De Gennaro Aquino et al. (2013). The second object discussed is Nova Mon 2012 (chapter 5), the first CN discovered as a high-energy γ-ray source: I collaborated to the analysis presented in Shore et al. (2013b), where archival observations of ONe novae have been reanalyzed and discussed in the light of the latest findings (chapter 6).

Chapter 2

Novae as cataclysmic variables

The evolution of stars in binary systems is one of the most important and constantly researched problem in astrophysics. Because of the huge number of binary stellar systems (roughly 50% of main sequence stars are binaries) and the extreme heterogeneity in physical parameters of these objects, we must deal with numerous different evolutionary paths.

Cataclysmic variables are binary stars in which one component is a white dwarf and the other is a Roche-lobe-filling, or nearly filling, star (fig. 2.1 for an artistic impression). Observationally they are usually recognized by optical brightness variations, which amplitudes and frequency define CVs classes: classical novae; recurrent novae; dwarf novae; nova-like variables.

2.1 The nova progenitor

To comprehend the properties of binary systems undergoing novae explosions, we must deal with stellar binaries evolution, which presents extreme differences with single stars evolution. In binary systems, a fundamental concept is the Roche lobe. The gravitational field of the system is characterized by constant potential surfaces, and a particular equipotential surface consists of two separate lobes, each one enclosing its stellar component, that touch in a single point along the jointing line of the stars center. The motion of particles in a Roche lobe is determined only by the star inside. The Roche lobes aren't spherical surfaces, but we define the Roche-lobe radius R_{iL} as the radius of the sphere for the i-component with the same volume, and it depends on the orbital separation A and masses of the stars

$$R_{iL} \sim 0.52\Big(\frac{M_i}{M_i + M_j}\Big)^{0.44} A \tag{2.1}$$

(Paczynski, 1971). Mass transfer is possible if particles are forced outside the lobe. In fig. 2.1, a main-sequence donor fills its Roche lobe, with gas streaming out from the first Lagrangian point, accreting on the white dwarf via an accretion disc.

It is not necessary here to completely discuss the evolutionary paths that binary sys-

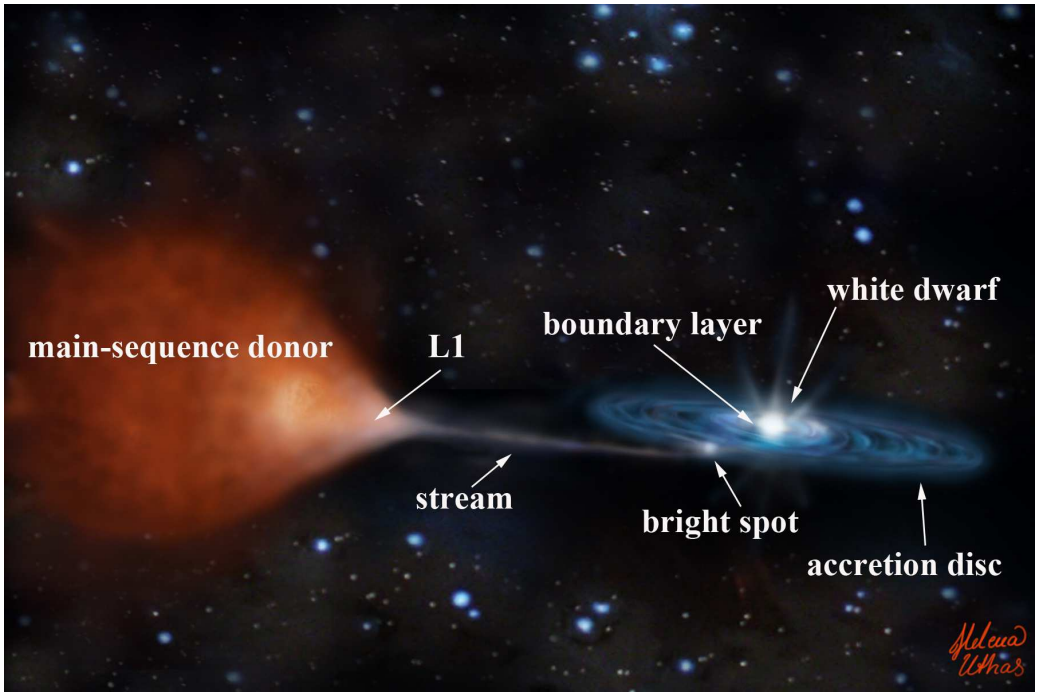

Figure 2.1: CV artistic impression by Helena Uthas (2011).

tems may follow depending on their initial physical conditions (fig. 2.2 for a schematic view) and we only concentrate on the birth of novae systems (fig. 2.3 for a compact diagram). See Iben (1991) for a complete review on binaries evolution.

The components of the system have different initial masses. At some time, which mainly depends on the mass, the more massive primary runs out of fuel (H and/or He) in the core. The orbital separation is large enough that the primary develops an exhausted core before filling its Roche lobe, but at the same time it is sufficiently small that once filled the Roche lobe, because of its extended atmosphere, a common envelope forms, a situation where both lobes are filled and matter definitely leaves the system. This eventually drives orbital shrinkage.

The initial primary mass is always sufficiently high that helium flash (i.e. the removal of the helium core electron-degeneracy by ignition of the triple-α reactions) settles, leading to a carbon-oxygen rich core (CO). In case of a single star, we would consider the case were the initial mass of the star was high enough ($\sim$8 $M_\odot$) to further ignite carbon fusion after the horizontal branch phase, leading to an oxygen-neon (ONe) rich core: this is partially true but must be contextualized for binary systems evolution.

Several mechanisms concur to decrease the orbital separation, which basically means angular momentum loss. As aforementioned, when the primary fills its Roche lobe, if the overflow on the secondary is slow enough that it does not fill its Roche lobe, the total angular momentum is substantially conserved. If instead both stars Roche lobes are filled, the system eventually goes through a common envelope phase, with mass spilling out from the system, taking away angular momentum. Another mechanism is magnetic braking, associated with magnetized stellar winds: the ionized wind is forced to corotate with the stellar magnetic field, inducing a spin-down torque on the star; for

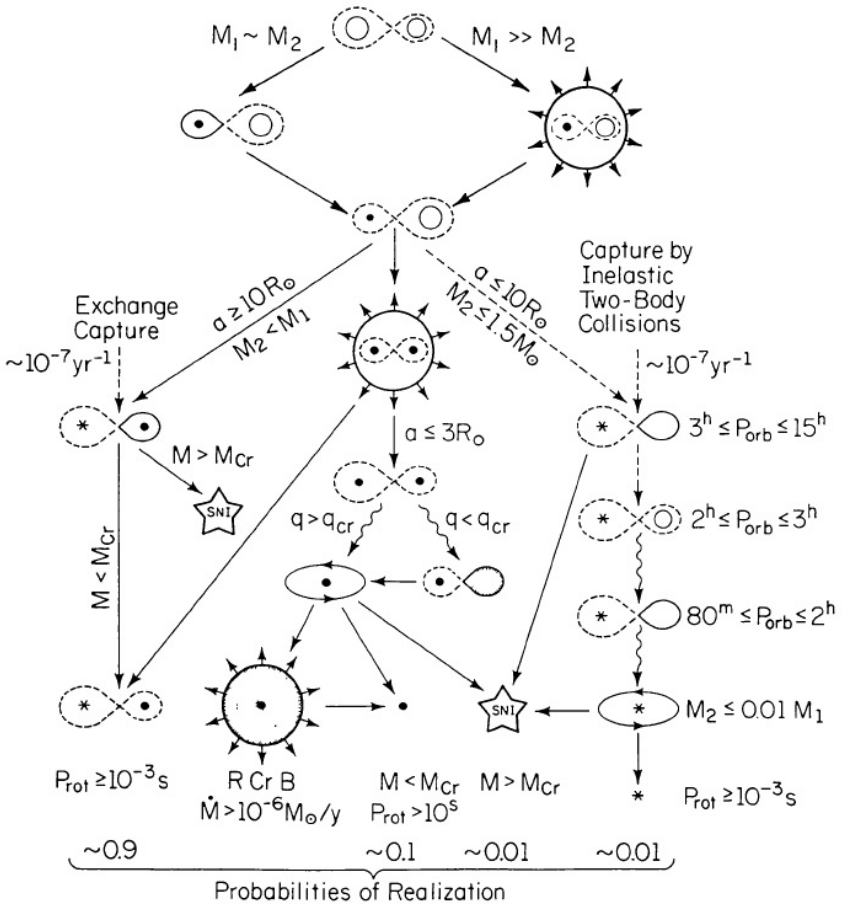

Figure 2.2: Scenarios for close binaries evolution (all the details in Iben, 1991).

these objects, tidal forces are so strong that synchronization is perfect, so the net effect of the wind is to extract angular momentum from the system. These two mechanisms concur to decrease the P_{orb} down to ∼2-3 hours. Angular momentum loss proceeds also via gravitational radiation waves, but it is efficient only for very tight systems ($P_{orb} \lesssim 2$ hrs).

2.2 Thermonuclear runaway

The modern picture describing the physical processes responsible for the explosions was understood in the 1960s' and modeled by pioneering computational works from Starrfield et al. (1972).

When the companion star evolves so that Roche lobe overflow allows accretion on the WD (slightly different scenario for symbiotic systems), a layer of H-rich gas with solar (or close) isotopic composition grows on the surface of the WD. If accretion is not extremely fast, the base of the accreted envelope becomes electron-degenerate and temperature raises due to continuous increase in pressure because of the growing layer, i.e. compressional heating. However, electron-degenerate gas pressure doesn't depend on temperature. It is still uncertain whether the accreted gas from the companion efficiently

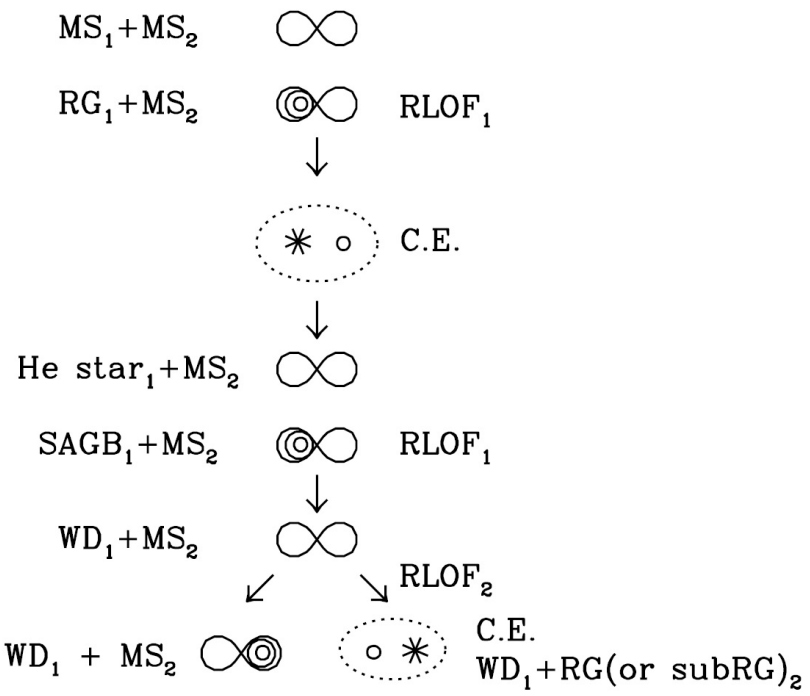

Figure 2.3: Schematic scenario of binary system evolution towards novae (Gil-Pons et al., 2003). *MS*: main sequence; *RG*: Red Giant; *RLOF*: Roche lobe overflow; *C.E.*: common envelope; *SAGB*: super asymptotic giant branch.

mixes, via diffusion and/or convection, with the WD external layers: this could bring metals in the H-rich envelope, increasing the opacity, hence the temperature.

At the core-envelope interface, hydrogen nuclear reactions are possible. Initially, nuclear reactions involving the Proton-Proton (1a-2-3) and P-e-P (1b-2-3) chains are the main contributors to energy generation, which rate is proportional to $T^4 - T^6$, so initially temperature rises slowly.

$$\begin{aligned}
&\text{1a)}\quad {}^1\mathrm{H} + {}^1\mathrm{H} \rightarrow {}^2\mathrm{H} + \mathrm{e}^+ + \nu_e \\
&\text{1b)}\quad {}^1\mathrm{H} + \mathrm{e}^- + {}^1\mathrm{H} \rightarrow {}^2\mathrm{H} + \mathrm{e}^+ \\
&\text{2)}\quad {}^2\mathrm{H} + {}^1\mathrm{H} \rightarrow {}^3\mathrm{He} + \gamma \\
&\text{3)}\quad {}^3\mathrm{He} + {}^3\mathrm{He} \rightarrow {}^4\mathrm{He} + {}^1\mathrm{H} + {}^1\mathrm{H}
\end{aligned}$$

Nuclear reactions involving H and He only cannot induce a nuclear flash on the WD, because the physical conditions for the helium flash are never attained. Reaction chains involving CNO nuclei (the Bethe-Weizsäcker-cycle) are indeed responsible for the TNR. The cycle works in a complex interplay of temperature dependence and nuclear cross sections and β-decay lifetimes. *Cold* CNO cycles are fundamental for stellar nuclear activity: in equilibrium conditions, the proton-captures and β-decays time scales are balanced and CNO isotopes abundances reach equilibrium ratios, with four protons fused into an helium nucleus. These chains become efficient at $\sim$15 MK, and predominant, over P-P and P-e-P chains, at $\sim$17 MK, and the energy generation rate is strongly dependent on temperature, being proportional to $T^{14} - T^{18}$, therefore a slight increase in temperature strongly enhances the hydrogen consumption by CNO cycles.

At the core-envelope boundary, with almost constant density ($\rho \sim 10^4$ g cm^{-3}), once the CNO cycles start, pressure increases. The medium doesn't respond to this augmented pressure with an expansion because of the degenerate conditions, hence it warms up. This enhances the CNO cycles, and eventually nuclear reaction rates go out of equilibrium because proton-captures are faster than β-decays (nucleosynthesis paths during the TNR are displayed in fig. 2.4). As the temperature gradient increases, the accreted material above the core-envelope boundary becomes convective unstable, bringing into the layer unprocessed material (CNO isotopes) from the WD surface.

Finally, a critical pressure at bottom of the envelope is reached,

$$P_{crit} = \frac{GM_{wd}M_{env}}{4\pi R_{wd}^4} \sim 2 \cdot 10^{19} dyn\, cm^{-2} \tag{2.2}$$

(Fujimoto, 1982) for which the degeneracy of the layer is removed. Temperature is close to $\sim 10^8$ K: during this very short stage, proton and α captures produce heavy elements, many being radioactive. Because of the sudden phase transition from degenerate to non-degenerate state, the hot envelope, rich of unprocessed H, He and radioactive isotopes produced by out-of-equilibrium CNO reactions, suddenly expands, but subsonically.

From equation 2.2 is clear that more massive WDs require less accreted mass in the envelope to rich P_{crit}. However, it does not take into account the metallic abundance, which is important for the duration of the pre-TNR phase: more metals means higher opacity, thus higher temperatures, requiring less mass accreted and lighter WDs for the critical pressure to be reached. As already mentioned, it is impossible for a helium WD to undergo a TNR because the envelope base never reaches the critical temperature to start triple-α processes. However, V445 Pup (Ashok & Banerjee, 2003) and other objects have been proposed to originate from such systems.

2.3 Convection and mixing

The correct comprehension and modeling (especially in one-dimensional code) of convection is fundamental but notoriously problematic.

The TNR produces a huge amount of energy which cannot be driven out of the envelope only by radiation: this is the basic reason for convection taking place, once the superadiabatic gradient is set in the layer. The core-envelope interface is convectively unstable: large scale motions bring freshly synthesized β-unstable isotopes (mainly ^{13}N,^{14,15}O,^{17}F) from the hot core-envelope interface towards the surface.

The convective turn-over time near the peak of the TNR is close to 1-10 sec: this allows the β^+-unstable isotopes to be mixed in the expanding envelope up to the surface before their eventual decay. The expansion lowers the density, so few protons can interact with these radioactive nuclei and nucleosynthesis is stopped.

Another possible effect of the sudden increase in temperature is the convective overshoot underneath the core-boundary envelope: this brings CNO elements outwards, enhancing the metallic abundances, and unprocessed H-rich gas from the envelope to the core, thus providing more reaction catalysts to the hot burning shell. Deep con-

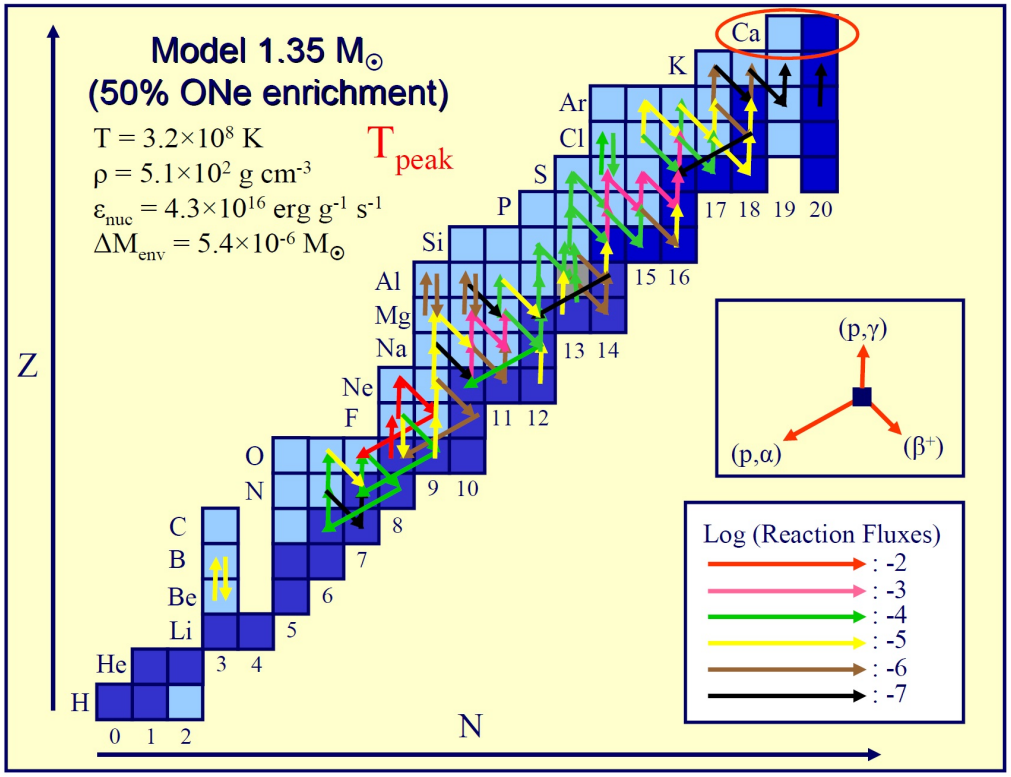

Figure 2.4: The main nuclear reactions taking place at the peak temperature (3.2×10^8 K) for a TNR with a 1.35 $M_\odot$ ONe WD. Reaction fluxes in number of reactions per unit volume and time (José, 2010).

vection is also responsible for the dredge-up of core metal rich material, the most clear example being the overabundances of neon, with respect to solar values, in ONe novae ejecta (chapter 5 and 6).

2.4 The ejection and dynamics of the envelope

The final ejection of the envelope is determined by the interplay between the convective timescales and the β^+-unstable isotopes lifetimes, mainly ^{15}O, but many other radioactive isotopes are produced during the peak of the TNR (for details, José & Hernanz, 1998). Once degeneracy is removed, the hot shell reacts expanding: density falls then proton capture rates drops. The convective motion, on timescales of $\sim 10^2$ seconds, have mixed, but not completely, the layer, with chemical inhomogeneities being spread all over the envelope; convective undershoot has also dredged-up metal-rich material from the WD top layers (fig. 2.5 shows the O mass fraction development over time during the initial stages of the TNR).

At this stage, convective motions bring up in the envelope, on time scales of $\sim$10 sec, the β-unstable nuclei. The lifetimes of the aforementioned isotopes are also close to $\sim 10^2$ sec, so that they act as a delayed source of energy, ultimately responsible for the ejection of the shell: approximately 10^{46} erg are released in few hundreds seconds.

When the β^+-unstable nuclei reach the surface, the luminosity increases, going up to $10^5 L_\odot$ or higher, and *Eddington luminosity* (next chapter) is frequently exceeded. The envelope is now expanding at velocity of few km s^{-1} , which means that the effective temperature is very high, close to 10^6 K. At this stage, the *bolometric maximum*, X-ray and EUV emission is very intense.

Once the shocks proceeds, maximum velocities from 10^3 to 10^4 km s^{-1} are achieved with a ballistic velocity profile: like in fireworks, the envelope is expanded in a very short time. With the surface area constantly increasing, the peak of the emission moves towards longer wavelengths. However, it has been predicted (Starrfield, 1972) that during this phase, the total luminosity of the system remains constant or slightly declines. This stage is known as *constant bolometric luminosity phase*, because the ejecta behave as a calorimeter.

In a ballistic flow with a fixed mass M_{ej}, the radial dependence of the velocity field is a linear relationship limited by a maximum velocity, so that the $r = r_{max} v / v_{max}$, and density decreases as $\rho \propto r^{-3} \propto t^{-3}$, because t and r are interchangeable. However, because of large scale hydrodynamic instabilities during the convective unstable phase, the shell is neither uniform or homogeneous. In the expanding shell, filaments and fragments interact and collide.

A portion of the expanding envelope, from 10 up to 90% of the initial mass (Starrfield, 1993), may have a velocity not sufficient to escape from the WD. The gas slows down, forming a quasi-static envelope around the WD. On the surface, temperature is still sufficiently high that hydrogen burning in a thin layer keeps going, with the stopped gas being a non-renewable resource, if we leave accretion from the companion aside. The WD is than observed as a *Super-Soft source* (SSS), if the ejecta are X-ray

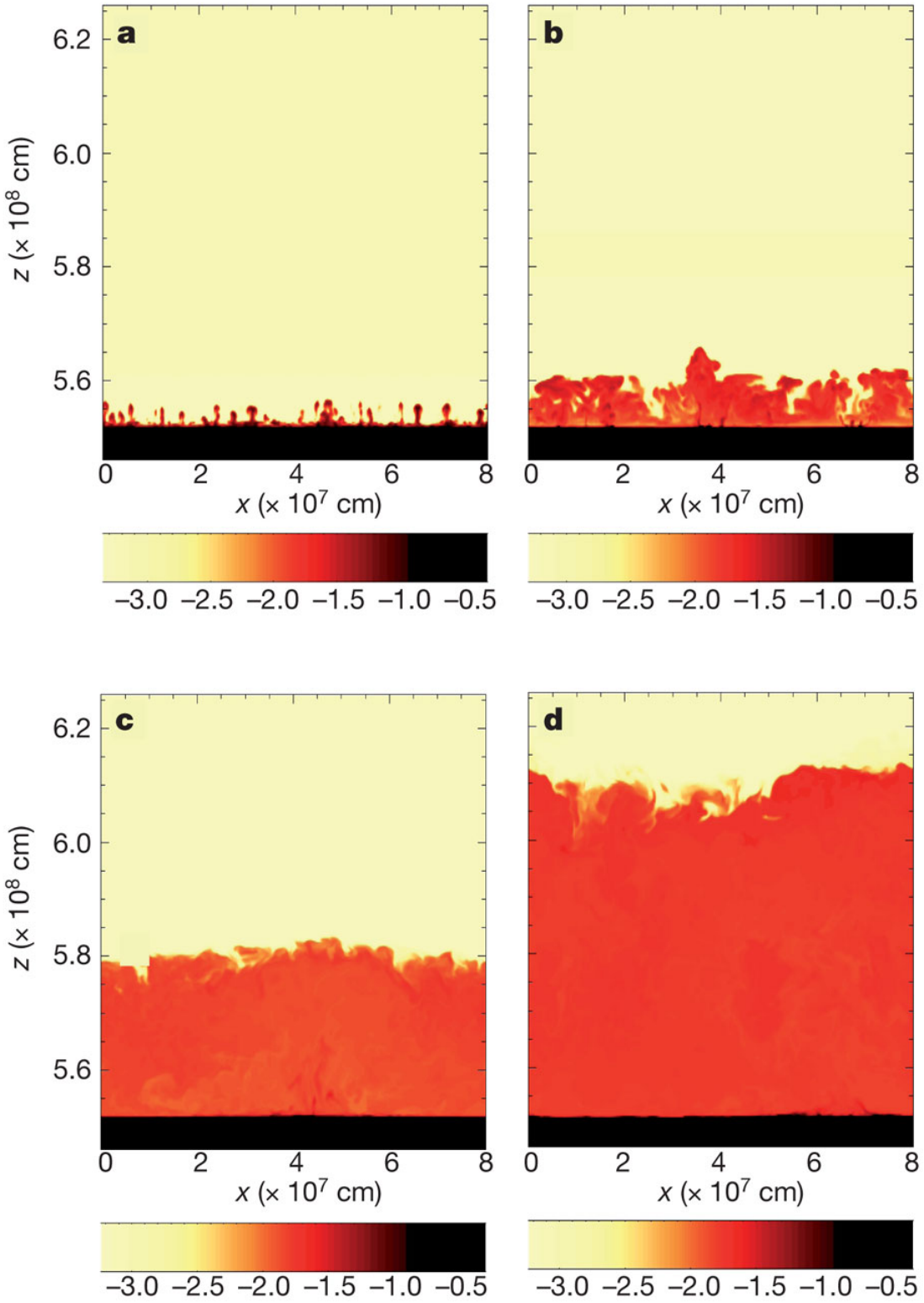

Figure 2.5: Three-dimensional simulation of mixing driven by Kelvin-Helmholtz instability at the core-envelope boundary at different instants after the (induced, with small temperature perturbations) explosion, $a = 151s$, $b = 193s$, $c = 296s$, $d = 379s$; the colors indicate the O mass fraction in each cell (Casanova et al., 2011).

optically thin.

2.5 Wind-like outflow

There has been a debated (since Kato & Hachisu, 1994) whether a wind-like outflow of mass takes place after the ejection and whether it is optically thick or not. The discussion actually touches the eventual outcome of the TNR explosion, arguing the reliability of the assumption of a ballistic ejection of the envelope. It is in fact suggested that there's no impulsive ejection at all, only an expanding envelope which photosphere, after reaching a maximum radius, recedes and effective temperature raises. Mass is continuously lost by wind, which optical depth reaches a maximum when log T (K) > 5.2. When the SSS turns off, the wind flow extinguishes too.

Observations and theoretical models support the presence of a *Hubble flow* velocity gradient (i.e. constant), which is a completely different solution than a wind-like outflow, with a profile $V(r) \propto V_{\rm inf}(1-1/r)^a$, where $V_{\rm inf}$ is the asymptotic velocity, which gradient goes to zero. One of the main argument against the optically thick wind is the presence in late stage of the expansion of very highly ionized species, like [Fe XIV], the "smoking-gun" for nebular optically thin conditions in the ejecta. Another clue comes from the observed optical depth development for the P Cyg profiles: for a wind-like flow, at $V_{\rm inf}$ the profile saturates, while for an ejected shell, it would initially display a P Cyg profile with a deep absorption but the density gradient imposed soon decreases its optical depth. This is known from highly detailed atmospheric models (Hauschildt et al., 1992): the velocity gradient in the line formation region for a wind-like outflow atmosphere is much narrower than in the ballistic ejection case, the latter being the closest model to the observed line profile.

It is possible though that during the SSS phase, strong radiation pressure could easily induce an outflow of material, but it would be ionized, therefore transparent.

From the analysis of T Pyx, I will show that several observed phenomena cannot be explained with an optically thick wind model.

2.6 Quiescence state

The detailed study of post-outburst activity is very useful to understand many properties of a CV, mainly the orbital parameters of the system and the accretion mechanism. For a general review on the properties of quiescent novae see Warner (2002).

With patience, ejecta become spatially resolved, thus providing important knowledge about their dynamical and chemical evolution and the interaction with the surrounding interstellar medium (for an extended review, O'Brien & Bode, 2008).

Observing the reset of accretion is a difficult task because the source is very bright. The post-outburst WD has a high effective temperature: the intensified flux on the secondary enhances the outflow of gas, resulting in a mass accretion rate higher then pre-outburst conditions. This is especially true for very close system (P_{orb} < 4 hr).

With continuous photometric observations, orbital modulation in the light curve is easily measurable for many novae. A very fortunate but infrequent situation happens for ecliptic systems, from which a very detailed description of the system can be obtained.

It is important then to investigate the dominant luminosity source and how the system responds to the accretion. In quiescence, the disc re-establishes and its signature is clearly seen spectroscopically, through Balmer lines diagnostics, and He II 4686Å being an important feature, because it probes the high ionization state of the gas. During this phase, the *dwarf novae* behavior may occur: if the accretion rate is low, mass can be stored in the disc and eventually a thermal instability starts, suddenly enhancing the accretion on the WD, resulting in a small brightness increase.

2.7 CO vs ONe novae

As mentioned above, the WD composition varies depending on the initial mass of the star. However, it is fundamental to interpret this assumption in the frame of binaries evolution: given the complex interplay between the two stars, any attempt to describe the evolutionary path followed by the system using single star theory is rather misleading or wrong.

Important studies have shed light on the evolution of binary systems (one of the first review was by Paczynski, 1971) and Law & Ritter (1983) suggested, before any observational claim, that an oxygen-neon-magnesium rich core is a possible, but rare (approximately 1/30), outcome. ONe cores also feature higher masses than CO ones. Gil-Pons et al. (2003) confirmed that the observational ratio of ONe vs CO novae, being $\sim$1/3, one order of magnitude higher than the expected ratio of ONe/CO WDs in these systems, originates from a strong selection effect on ONe novae being more energetic, thus observable in a larger galactic volume.

The chemical composition of the WD (actually of its outermost layers) is revealed in spectroscopic observations and the understanding of the nucleosynthetic and mixing processes between the envelope and the core is tightly connected with the interpretation of the spectra.

2.8 Dust and ashes

In the chemical history of the Galaxy, novae play a minor role as contributors to the interstellar medium with respect to other objects, for example supernovae. With a rough estimate, given a novae occurrence rate of 30 yr^{-}1 and an average ejected mass $2 \times 10^{-5} M_{\odot}$, in a Galaxy lifetime it means $\sim 10^{7} M_{\odot}$, which is $\sim$0.3% of the galactic disk mass. However, it is recognized their importance for certain stable isotopes abundances, i.e. ^{13}C, ^{15}N, and ^{17}O (José & Shore, 2008). Theoretical models, while being constantly updated and improved, still present some problems in matching the observed abundances with the predicted values: perhaps longstanding approximate physical inputs in the codes (diffusion, convection, nuclear cross sections) and poverty of multidimensional simulations are the main causes.

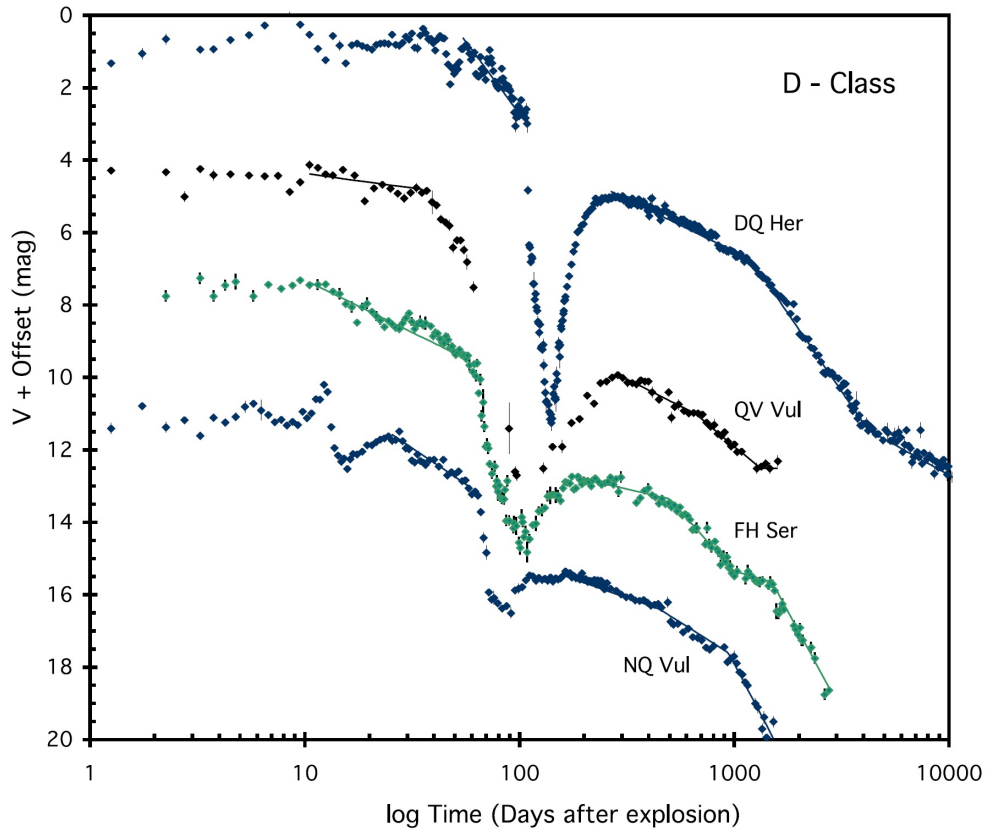

Figure 2.6: Proficient dust producers novae lightcurves (Strope et al. 2010).

During the TNR, ^{13}N,^{14,15}O,^{17}F isotopes represent the most abundant metallic species produced, with their β-decay activity eventually driving the expulsion of the envelope. However, the result of proton-capture and α-capture reactions during the peak temperature is more complicated but not impossible to model. From fig. 2.4, we see that reactions proceed mainly on the valley of stability, driven by proton-capture and β-decay, with α-capture being only marginal.

Dust formation is an interesting process that was observed back in 1933 with Nova DQ Her by McLaughlin who suggested that the sharp drop in V-magnitude was caused by copious amounts of dust formed in the ejecta, heavily extinguishing the nova but not changing the line profiles (McLaughlin, 1935). It was only in 1970 with the infrared observation of FH Ser (Geisel et al., 1970) that finally confirmed the production of dust in the ejecta. The observation of dust grains goes along with the presence of molecules in the ejecta.

2.9 A complicated case: symbiotic-like novae

Symbiotic stars are systems composed by a WD and a Red giant or Asymptotic Giant Branch (AGB) companion, both never filling their Roche lobes because of the great orbital separation ($P_{orb} \gtrsim$years), in fact accretion from the wind drives the mass transfer. *Symbiotic-like novae* are a very small subset of CVs (7 known, plus 5 known symbiotic-

like recurrent novae) and, although the mechanisms leading to the TNR and ejection are identical to CNe, the dynamics of the shock and ejecta are fundamentally different.

Once the shock reaches the top of the WD accreted envelope, it encounters a dense environment, the companion wind, which interaction extremely complicates the spectroscopic evolution of the nova (next chapter). High energy γ-rays emission was observed during the last outburst of the recurrent nova V407 Cyg, with a remarkable observation from Fermi/LAT (Abdo et al., 2010): the main source is thought to be the strong interaction between the shock and the wind (Hernanz & Tatischeff, 2012).

The shock expanding in the RG wind accelerates the gas, that has roughly solar composition, mixing with the nova envelope, thus any abundance determination is extremely complicated. The structure of the environment is also problematic, being not spherical (the Roche lobes are complex surfaces) neither uniform, so that the shock propagates differentially in the wind. The passage of the shock and photo-ionizing radiation establish the ionization state of the matter: after the *break out*, the wind is left highly ionized.

2.10 Concerning spectra

Our knowledge about the nova phenomenon strongly depends on observations, especially spectroscopy: it is only through detailed analysis of the whole electromagnetic spectrum, from γ-rays to radio, that we can test the models. In the last half-century the picture has become very clear, especially thanks to outstanding improvements in computational capabilities and very important observational achievements.

Chapter 3

Optical and ultraviolet spectral evolution

Nowadays novae are studied panchromatically thanks to ground-based observatories, for radio, infrared and optical astronomy, and space telescopes, pushing observations down to the ultraviolet, X and γ wavelength ranges, which for obvious temporal reasons, can't follow an outburst with high-cadence. Thanks to intense time coverage analysis for past novae and improved theoretical models, today we have a very detailed picture of each step of the outburst. See Shore (2008) for a complete review, Anupama & Kamath (2012) for an insight on optical evolution, or Starrfield (1993) for a general overview of the phenomenon.

As already introduced, after the explosion, the ejected material is basically a passive medium. The gas moves outward in free expansion, therefore density, temperature and ionization change in time, and at the same time the activity on top of the WD changes. The picture is different for symbiotic novae, where there is a strong interaction between the ejecta and the circumstellar medium, hence the gas is an active medium.

An immediate and effective way to describe the evolution of the outburst is looking at a nuclear weapon test conducted in space. Four snapshots of the Starfish Prime space test (one of the five high altitude tests in the Operation Fishbowl, a 1.4 Mt yield at 400 km above Johnston Island in the Pacific Ocean, on 1962 July 9th) easily describe the appearance of the system after the explosion: fig. 3.1a, caught $\sim$0.5 seconds after the detonation, shows a bright, optically thick surface, the photosphere; in fig 3.1b, c, and d, the debris of the bomb turn progressively more transparent, freely expanding, although there is a weak but observed interaction with Earth magnetic field (Defense Atomic Support Agency report, 1962), showing filaments and knots. This interesting but disquieting example is wrong for several details, for example the interaction of the bomb with the atmosphere, although very weak with respect to ground nuclear tests (at that altitude, in the *Low Earth Orbit Zone*, the background density is $\sim 10^{-12}$ kg m^{-3}, from *US Standard Atmosphere 1976*), and the complete destruction of the explosive core.

(a) 0.5 s after detonation. (b) 1 s after detonation.

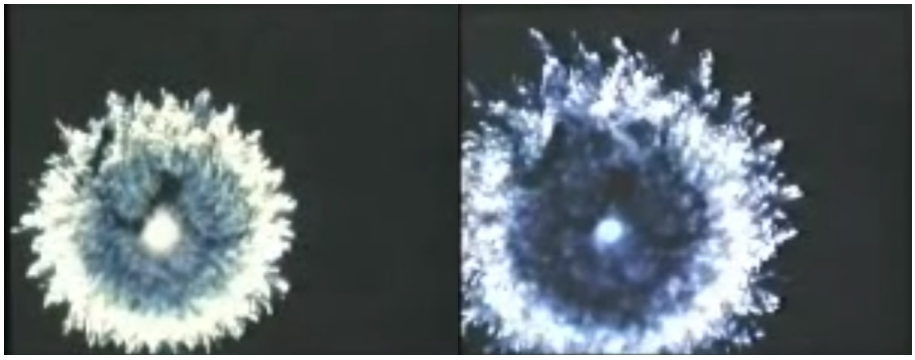

(c) 2 s after detonation. (d) 3 s after detonation.

Figure 3.1: Shots from the Starfish Prime Test.

3.1 The fireball stage

During the *fireball stage*, the system should be visually similar to fig. 3.1a. After the TNR and ejection, the ionizing shocks drives the expansion that proceeds adiabatically, because the envelope expands much faster than any radiative cooling timescale. In the frame of the expanding shell, the velocity field is imposed, but the medium is not uniform nor homogeneous. For the spectroscopic analysis, the *filling factor* f, i.e. the total volume occupied by the condensations or, naively, the ratio of filled and empty volume, is fundamental.

An optically thick *pseudo-photosphere* forms and expands until both recombination rate, and gas temperature and density drop sufficiently that the shock decouples from the radiating surface (the *breakout*). The optically thick surface eventually recedes, down to the WD surface, and the free expanding ejecta eventually turn optically thin.

During this phase, hard X-ray emission, energies >1 keV, is observed: it is thought that filaments and dense knots in the expanding envelope collide, undergoing internal shocks (Schwarz et al., 2011). The same mechanism is probably responsible for high-energy γ-ray emission too, as observed for Nova Mon 2012 (Shore et al., 2013b) and Nova Del 2013 (Hays et al., 2013). The geometry of the filaments/knots eventually freezes, similar to fig. 3.1c and d, and it is reconstructible from emission lines profile during the late nebular phase or, with a lot of patience, once the ejecta are spatially resolved.

The main source to the optical depth in this phase is photon-electron scattering, which is tightly linked to the luminosity of the novae frequently exceeding Eddington luminosity L_{Edd}: hydrostatic equilibrium for a (spherical) stellar atmosphere does not hold if the luminosity L of the star

$$L > L_{Edd} \simeq 3 \times 10^4 \Big(\frac{M}{M_\odot}\Big)\Big(\frac{0.4\, cm^2\, g^{-1}}{\kappa}\Big) L_\odot \tag{3.1}$$

where κ is the Rosseland mean opacity, which minimal value corresponds to pure photon-electron scattering. Super-Eddington luminosities have been observed for all classes of novae. This dynamically unstable phase may last for days, as for example in N LMC 1991 (Schwarz et al., 2001) or T Pyxidis (next chapter), and it is driven by the hot superficial shell of the WD combined to a porous medium, thus a low opacity.

The fireball phase, which photometrically coincides with the raise to maximum brightness, has been observed panchromatically in very few cases (the most notable being OS And 1986, V1974 Cyg 1992, Nova Cas 1995, Shore 2008 for details). The expanding envelope in this stage is sufficiently dense that collisional equilibrium is a reasonable approximation. The density is easily estimable if we assume pure Thompson scattering opacity, with a cross section $\sigma_{Th} = 6.65 \cdot 10^{-25}$ cm^{-2}, in the expanding envelope, with a volume comparable to a Red Giant (V$\sim 10^{40}$ cm^3), the mean free path for photon being $l_{mfp} \approx (n_e \cdot \sigma_{Th})^{-1}$, we get a value of electron density $n_e \sim 10^{11}$ cm^{-3}. Optical depth τ is roughly proportional to the density, which in the free expansion solution decreases with $r^{-3} \sim t^{-3}$, and inversely proportional to the mean free path for photons,

so that $\tau \sim r^{-2} \sim t^{-2}$.

3.2 The iron curtain

After the shock breakout, cooling proceeds adiabatically. Recombination initially enhances the emissivity, in fact UV emission slightly increases. But when temperature falls below $\sim 10^4$ K, recombination accelerates and opacity increases, mainly due to ultraviolet line absorption by low ionization species and CNO continuum absorption. During this phase, a complete NLTE treatment is necessary (Hauschildt et al., 1992): the velocity field and the large extension of the shell lead to a very large gradient in both temperature and particle density, radiative processes dominate over collisions, in a radiation field which is "non-gray". Absorption bands (in Hauschildt's models are included millions of lines) in the ultraviolet range redistribute the flux towards longer, less opaque wavelengths were the spectrum is characterized by Balmer lines and a complex population of absorption-emission lines mainly coming from neutral species, C^0, O^0, Mg^0, Na^0, and low ionization species near the iron peak, Fe^{+1}, Ti^{+1} etc.

In the UV range, the spectrum is characterized by very low integrated flux and many *pseudo*-emission features, which are portions of the spectrum relatively unaffected by optically thick bands. At the same stage, the optical spectrum presents P Cyg Balmer lines, a clear indication of ongoing recombination, and plenty P Cyg lines from Fe II and other low ionization elements: the UV bands copiously populate the levels involving these transitions.

With high resolution spectroscopy, it has been possible to study in details the P Cyg profiles development during the iron curtain phase (Hauschildt et al., 1995). When the gas sufficiently cools, the pseudo-photosphere recedes and a recombination front moves outward in the ejecta: the P Cyg absorption extension varies, initially tracing slow inner gas (where density is higher and recombination more efficient) and then expanding to high negative velocity, showing a complex system of absorption features caused by parcels of clouds on the line of sight.

Meanwhile, the expansion goes on: the ejecta continuously rarefies and recombination rate drops. The hot WD surface, heated by post-outburst nuclear activity, reionizes the ejecta.

3.3 The nebular stage

Commonly the *nebular stage* is defined by the appearance of forbidden lines from highly ionized species in the optical and infrared spectrum, such as [Al IX], [Ca VIII], [Fe VII] to [Fe XIV], [Ne VII], [S IX] etc. The ejecta are completely optically thin and are irradiated by ionizing X and far-UV emission from the hot and burning surface of the WD: because of the low density, atomic levels are excited and de-excited mostly through radiative processes, not collisions, therefore intercombination and forbidden lines appear, arising respectively from FUV pumped and collisionally excited states. The ionization

conditions of the ejecta tightly depends on the activity of the central ionizing source, i.e. the X-ray emission.

Comparing the P Cyg profiles during the optically thick phase (e.g. the Balmer lines), it is usually observed that the terminal negative velocity of the P Cyg absorption is higher than the optically thin emission profiles half-width-zero-intensity: this is a pure optical depth effect, in fact the P Cyg absorption is weighted on the column density, that varies as $r^{-2} \sim v^{-2}$, while the emission line flux is weighted on the ejecta density, that varies as $r^{-3} \sim v^{-3}$. (fig. 3.2)

The optically thin phase spectra perfectly show the chemical differences between CO and ONe novae. In the first case, CNO abundances are super-solar, He/H ratio is near solar and heavy elements are rare. CO novae are known to be efficient dust producer: this mechanism is clearly observed in infrared because the grains show up as black-body-like thermal continuum, and their major effect is to heavily extinct the luminosity of the nova, without changing the appearances of the emission lines. ONe novae present sub-solar C and super-solar O and Ne abundances, with the infrared [Ne II] 12.8μm line being the earliest signature of the peculiar WD composition.

The structure of ejecta is frozen at the ejection, but the ionization conditions may evolve with time, depending on the WD activity. Using very general diagnostic tools for nebular objects, e.g. [N II] or [O III] lines fluxes ratios (see appendix for details), we can study the electron density and temperature of the ejecta evolving with time, and with high resolution spectra, we can spatially reconstruct $n_e(r)$ and $T_e(r)$, with the underlying hypothesis of ballistic ejection ($v_{rad} \sim r$).

3.4 Late phase

When the X-ray emission luminosity and T_{rad} of the WD fall below the critical ionization level, the ejecta resemble a fossil H II region. The ionization stages are frozen in the gas, unless some ionizing radiation is emitted by the WD. The emission lines fluxes then evolve following pure recombination, thus being dependent on the temperature and density of the gas and the rate of the expansion.

The UV emission lines development clearly shows this behavior, a famous example being the late evolution observations with IUE of V1974 Cyg (Shore et al., 1996). It was observed that the integrated emission fluxes from resonance lines, after the initial rise, decreased initially quickly than, after the X-ray turn off, following a steady slow decline, similar to a fossil H II region. For example, the emission flux from He II 1640Å after SSS-turn-off was almost perfectly fitted by

$$ln(j_{1640}/j_0) = \frac{1}{2}\alpha n_{e,0} t_0 [(t_0/t)^2 - 1] \tag{3.2}$$

(Shore et al., 1996), with α being the He II recombination coefficient, n_e the electron density, and the subscript 0 indicating the turn-off time specific values. Vanlandingham et al. (2001) also demonstrated that, with no knowledge about the X-ray emission history, this behavior could give a confident estimate about the X-ray turn-off time.

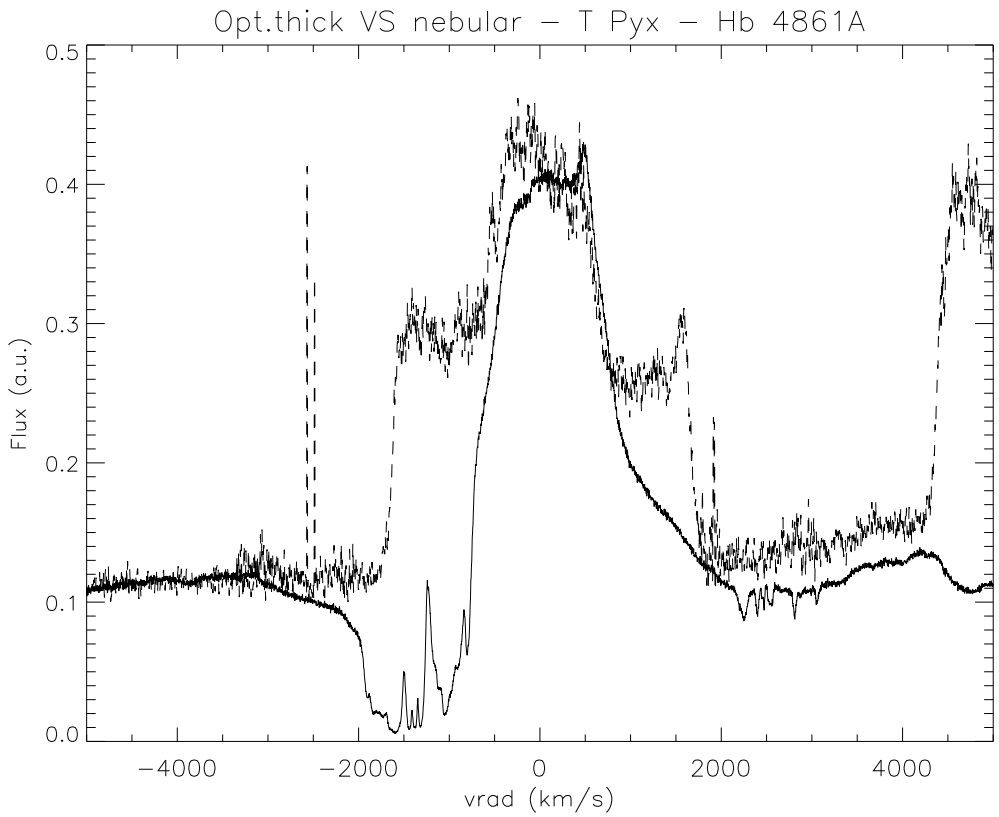

Figure 3.2: T Pyx Hβ line profiles comparison: solid lines during the optically thick stage, dashes during the nebular phase. The extension of the P Cyg (fragmented) absorption is 50% higher than the terminal velocity of the line in the nebular stage.

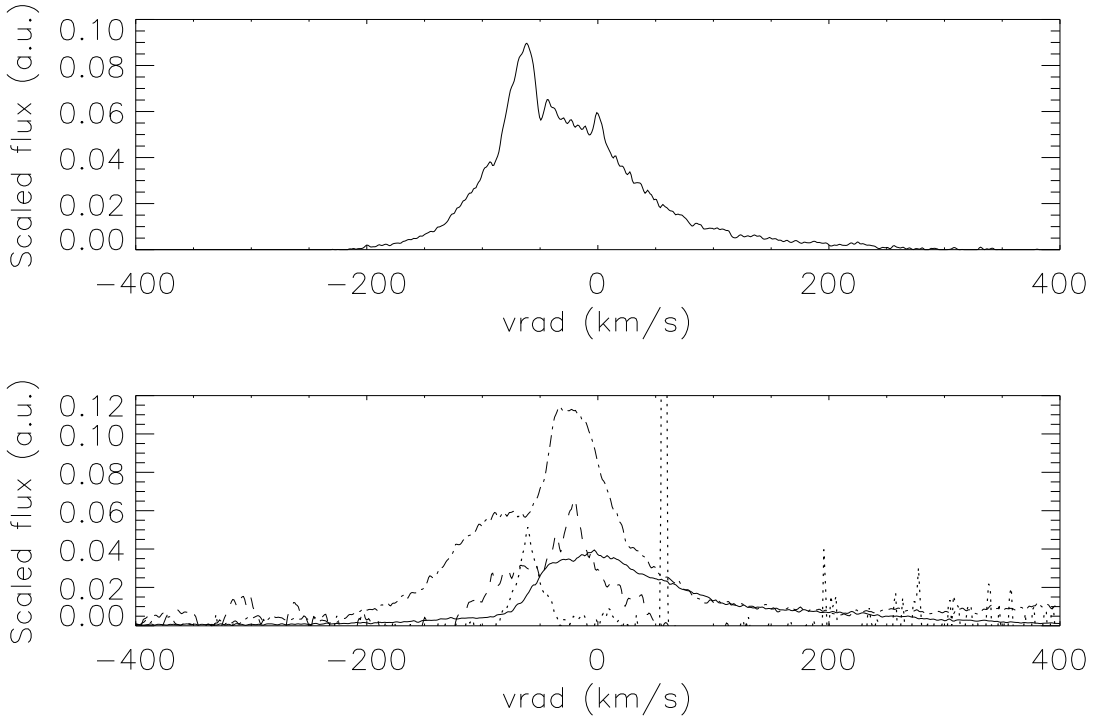

Figure 3.3: V407 Cyg 2011 - reconstruction (bottom) of [O I] 6300Å (top) with the emission profiles from different species, tracing different physical conditions: solid - [O III] 5007Å, ionized Mira companion wind; dots - Mg I 4571Å, chromosphere and neutral wind; dashes - [S II] 6716Å, shocked gas; dot-dash - [N II] 6548Å, extended lower ionization outer wind (Shore et al., 2012).

The reestablishment of the quiescent state, i.e. the pre-outburst physical conditions, may take several years. However, it is still debated whether, after the outburst, novae systems eventually return to their pre-outburst conditions. The explosion may in fact alter several properties of the systems: the metallic abundance on the WD outer layers, via undershooting convection or nucleosynthesis; the companion mass outflow rate; the orbital separation, because of the angular momentum losses; the mass of the WD, depending on the ratio $M_{accreted}/M_{ejecta}$.

T Pyxidis represents one of the few novae observed with high resolution UV instruments years after the outburst, thus being a perfect example to show the properties of the late phase emission.

3.5 Symbiotic-like novae evolution

Symbiotic-like novae evolution are much more complex than classical novae because the physical conditions in which the TNR and subsequent explosion take place are extremely more complicated. RS Oph, which 1985 outburst UV spectral evolution was followed with IUE (Shore et al., 1996), and V407 Cyg, a γ-ray emitter intensively followed during its 2010 outburst (Shore et al., 2012), are important examples for the comprehension of these systems

Once the TNR sets in, the explosion does not lead to a free expansion, in fact an

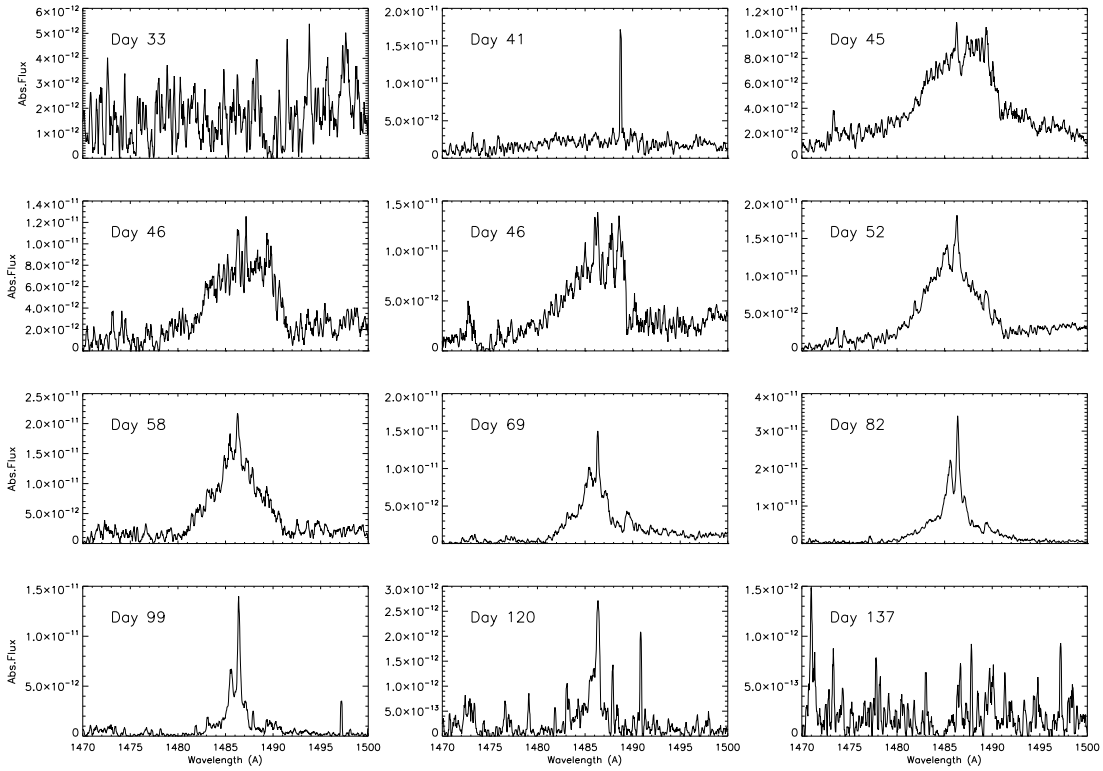

Figure 3.4: Spectral development of N IV] 1486Å in RS Oph 1985 outburst. IUE high dispersion spectra from the MAST archive.

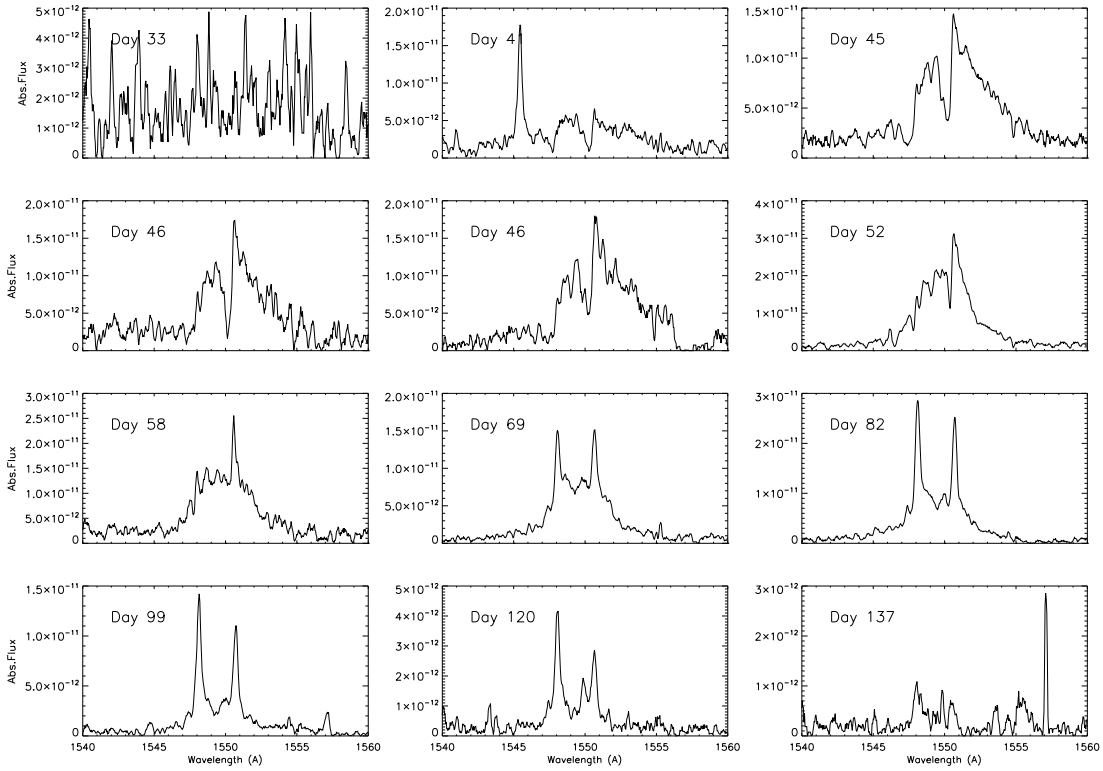

Figure 3.5: Spectral development of C IV 1550Å doublet in RS Oph 1985 outburst. IUE high dispersion spectra from the MAST archive.

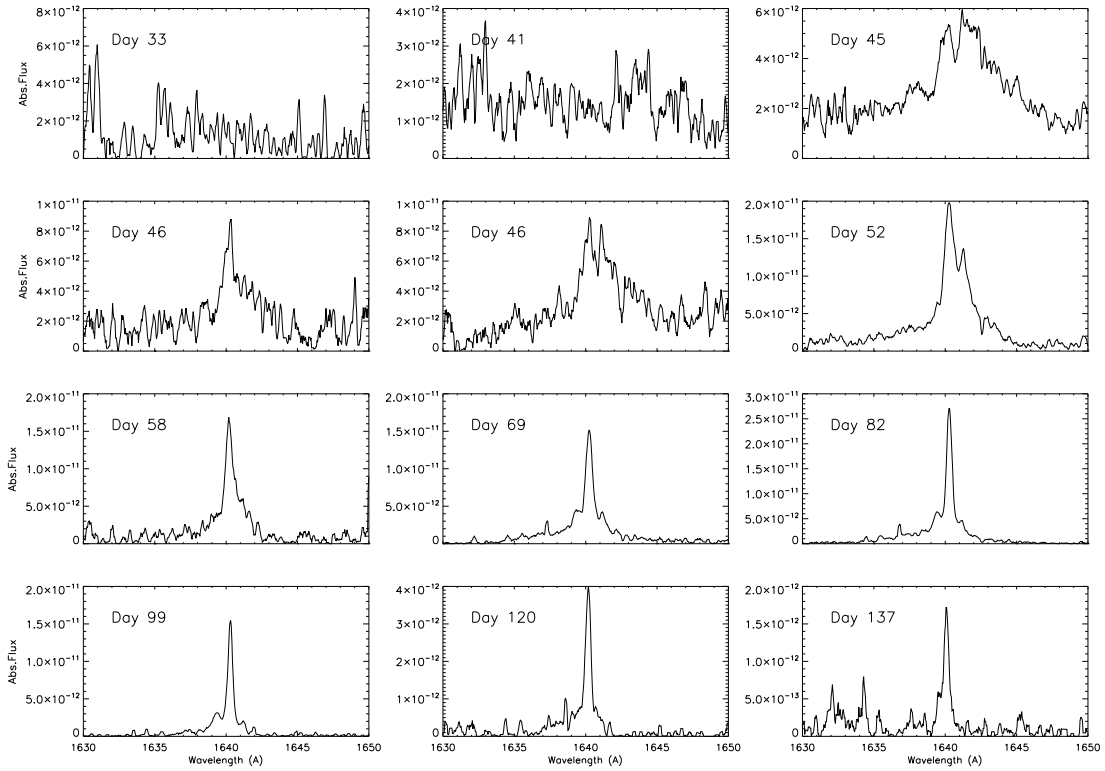

Figure 3.6: Spectral development of He II 1640Å in RS Oph 1985 outburst. IUE high dispersion spectra from the MAST archive.

outward propagating shock forms and travels through the dense matter surrounding the system. The temperature at the base is very high, close to 1 MK.

The line profiles evolution then follows the ionization front moving outward in the RG atmosphere. The shock-wind interaction is an important energy source for the emission. Concerning optical spectra, during this initial phase, Balmer lines show an extended emission profile with the absorption signature of the RG wind absorbing on the line of sight. The emission lines velocity extension is related to the internal shock propagating throughout the wind, which strongly ionizes the gas, driving intense X-ray soft emission.

While expanding, the ejecta accumulate material and the composition is a complicated mixture of the WD expelled envelope and the giant wind.

When the shock breaks out, the ejecta emerge from the extended RG wind and then freely expands. The wind gas then recombines: the profiles now develop narrow emission features, with the velocity extension reflecting the velocity field of the wind.

Figures 3.4, 3.5, 3.6 show the evolution of the lines N IV] 1486Å, C IV 1548, 1550Å doublet and He II 1640Å in RS Oph 1985. After an initial, optically thick stage, the ejecta broad emission appears, with the wind causing the narrow absorption. Later, the ejecta break out, their relative emission eventually fade. The shock has left the wind highly ionized, as demonstrated by the presence of [Fe XIV] lines in RS Oph. After the break out, the wind recombines: narrow emission features appears, with the shocked gas and the highly ionized chromosphere often distinguishable (for instance, from the profile

development of N IV] 1486Å in RS Oph, fig. 3.4: the spectral resolution is sufficiently high to distinguish, from day 52, the blueshifted emission from the shocked gas and the not shifted component of the wind, with the broad emission coming from the fast ejecta). However, the full reconstruction of an emission line could be a difficult task, especially with high resolution spectra (fig. 3.3).

The growth of the narrow emission features from the post-shocked wind is an helpful incident: it is extremely useful in the recognition process of the lines, because their FWHMs are on the order of ∼100 km s^{-1}, thus allowing for less ambiguous identification, which is often a problem when dealing with "usual" emission lines from novae, with FWHM≳2000 km s^{-1}. In Shore et al. (2013b) we have used this property to successfully identify the [F III] 2930Å emission in Nova Mon 2012, comparing with late stage IUE spectra of RS Oph.

3.6 Light curves

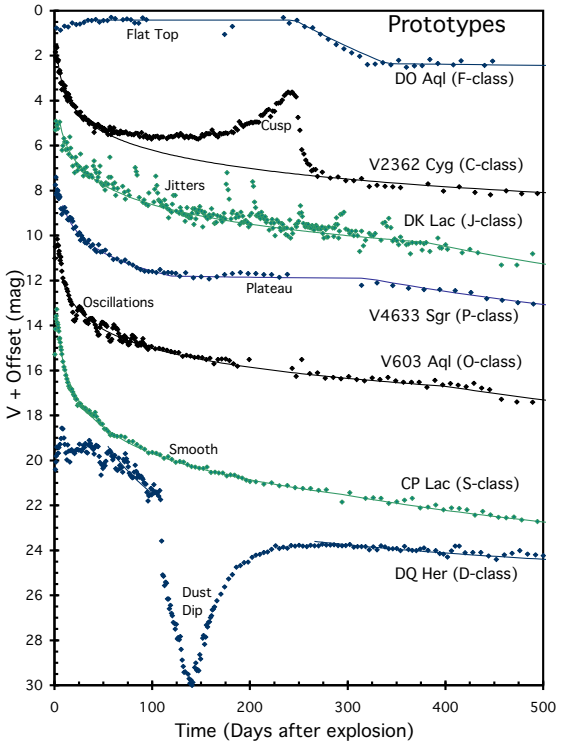

Figure 3.7: Novae light curves morphological classification (Strope et al. 2010).

A detailed nova visual light curve is a powerful tool, if used correctly: it is easy to measure and it carries important information, but its physical interpretation must necessarily face the spectral evolution of the object. Payne-Gaposchkin (1957) introduced the speed-class classification still *a la mode*. The 2 and 3 magnitude decline time (t_2 and t_3 respectively) have a significant physical meaning: small t_2 (fast) usually means low ejected mass. However, for several reasons, a low mass ejecta nova can display a peculiar light curve that makes the t_2 (or t_3) timescale meaningless. We should also be very careful about the photometric filter used: because of the rapidly evolving spectra, both line and continuum emissions change in time, hence each photometric filter will register different maximum magnitudes and rate of decline. This is the reason for usually defining t_2 and t_3 in the V band.

A recent morphological classification has been proposed, highlighting photometric

features that seem shared between more novae. The classification is illustrated in fig. 3.7 (see Strope et al., 2010, for details). These classes still lack precise physical interpretations and proper spectroscopic explanation of certain light-curve feature, but there are exceptions for example the D-class, with the well known dip feature caused by the augmented absorption by dust. The brightness fluctuations present during the declining phase of the light curve, occasionally showing periodicity or increasing temporal separations between subsequent peaks (the O and J class) represent an explained although very common event. T Pyx light curve showed this phenomenon.

For a complete comprehension of the nova problem, it is therefore necessary to extend the wavelength range of the observation and spectroscopically investigate the objects.

3.6.1 The maximum magnitude vs rate of decline relation

Zwicky (1936) was the first to suggest a relation between the maximum magnitude and the *lifetime* (rate of decline) of novae light curves. The contemporary state of the problem is summarized by Warner (2008). The usual relationship is the following

$$M_{max} = A + B\, log(t_2) \tag{3.3}$$

The physical motivations for this relation are based on the explosion mechanism and simply depends on the WD mass. If the WD mass is high, the amount of gas to be accreted to reach TNR conditions is low; the explosion will then blow up less, faster material. The optically thick phase, when the magnitude is at maximum, will therefore be short (low t_2 or t_3).

Della Valle & Livio (1995) used a large sample ($\sim$100) of photometrically observed classical novae in LMC and M31 to derive the absolute maximum magnitudes and t_2 times (fig. 3.8), then determined this best-fit model

$$M_V = -7.92 - 0.81\, arctan \frac{1.32 - log\, t_2}{0.23}. \tag{3.4}$$

The 3σ is $\sim$0.5 mag. They used t_2 (or indifferently v_{2d}, the rate of decline, defined as $v_{2d}=2/t_2$) because, given the faintness of the objects observed, t_3 was often poorly measured, being on average 70% longer than t_2. Moreover, the survey is limited to bright outbursts with low t_2, because faint, hardly detected novae, usually present longer t_2. Another issue arises from the use of the bolometric correction, which is not obviously physically meaningful: it is assumed that the ejecta, at the maximum magnitude of the outburst, are optically thick and flux redistribution works perfectly, ignoring any spatial property of the gas (like filling factor or geometry). The relation was applied for the Virgo cluster's novae and returned a reasonable estimate of the distance. Their work is an important extension to pioneering observational surveys conducted in the past, e.g. the work by Arp (1956) who derived a similar curve for M_{max} vs t_2 (fig. 3.9). The best-fit model by Livio & Della Valle has no clear theoretical support and the authors also recommend about the large scatter around the MMRD relation, being a consequence of

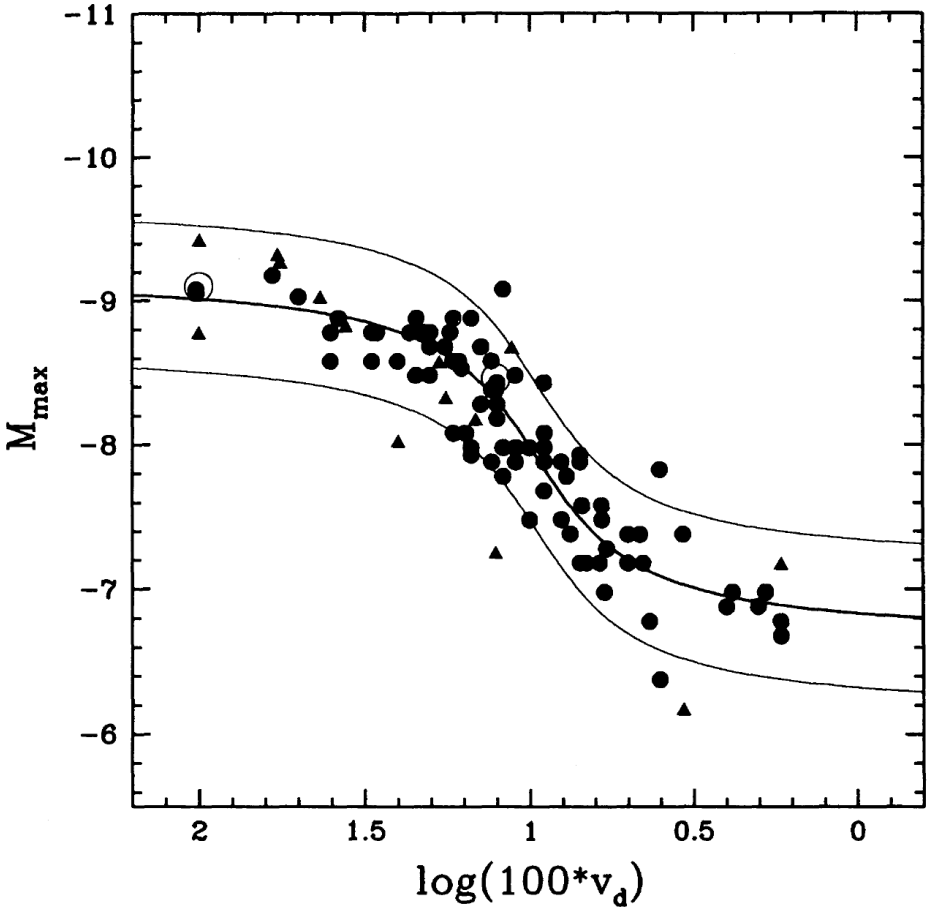

Figure 3.8: Maximum magnitude vs rate of decline relationship by Della Valle & Livio (1995), with novae observed in M31 (*filled circles*) and LMC (*triangles*). The best fit (eq. 3.4) is the solid curve, with $\pm 3\sigma$ curves located above and below it. Each apparent magnitude was transformed to an absolute V-mag using different distance moduli for M31 and LMC.

the multitude of physical parameters involved in novae explosions along with the WD mass.

3.7 CTIO spectral classes

Novae are commonly classified with a spectral taxonomy, introduced by Williams (1992), that characterizes the prominent, non-Balmer features in the optical spectra. This classification is named after an intense observational campaign conducted at the Cerro Tololo Inter-American Observatory (CTIO).

The *Fe II*-class members show, in the early phase, P Cyg profiles from Fe II and other low ionizations transitions, such as Na I, O I, Mg II, Ca II. The early nebular phase is domination by low ionization auroral lines, while some develop strong [Ne III] lines. For *He-N* novae, the early phase strongest non-Balmer lines are from helium, neutral or firstly ionized, or nitrogen, N II/III, with P Cyg absorption weak or absent. The nebular phase is characterized by broad emission lines, some novae develop high excitation

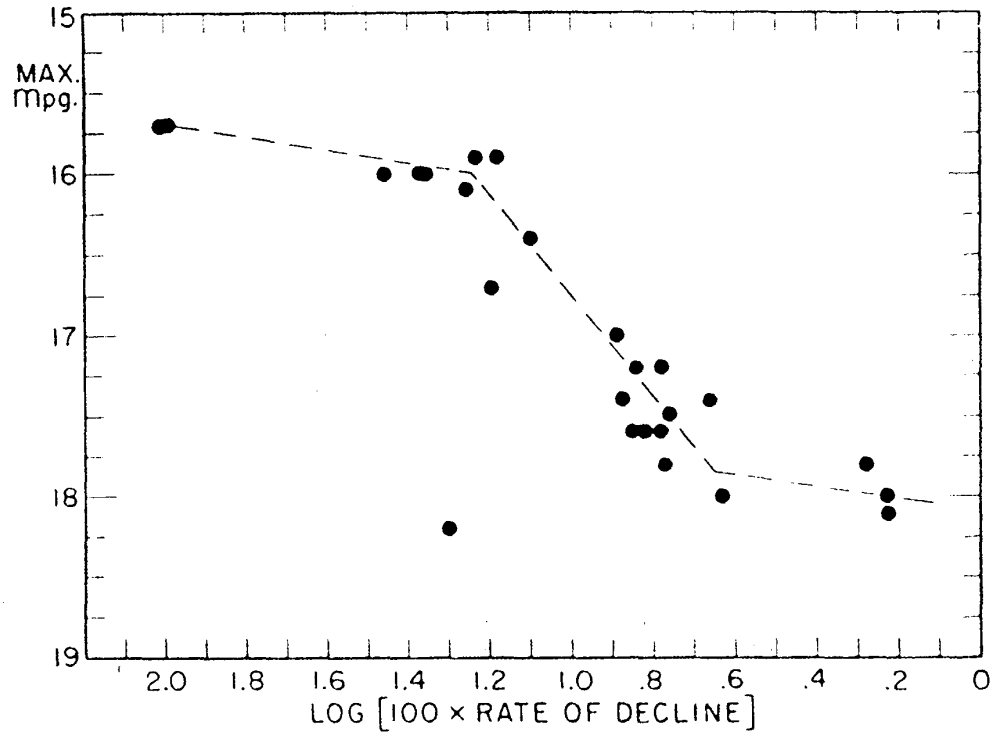

Figure 3.9: Maximum apparent magnitude vs rate of decline relationship by Arp (1956) with novae observed in M31. The dashed broken lines represent a mean behavior, with ± 0.2 magnitude as average deviation from the lines.

coronal lines, and some show Ne III lines too. The *hybrid* class shows mixed features, starting as a Fe II nova and evolving into a He-N.

It is clear that these classes correspond to spectral evolutionary stages of the nova. For example, some outbursts may be caught very late in the spectral development of the ejecta, because of the fast evolution of the nova, therefore spectra may show strong emission lines: following this classification, we should label those as He-N novae, but surely they passed through an early, perhaps short, stage when the ejecta were optically thick, resembling Fe II novae.

3.8 X-ray emission

Novae are proficient X-ray emitters. For a comprehensive review of novae X-ray astronomy see Krautter (2008). The study of their high energy emission has been conducted with several space facilities, the first being *EXOSAT*, with the pioneering observation of GQ Mus 1983 (Ögelman et al., 1984), followed by *ROSAT* during the early 90s', *XMM-Newton*, *Chandra*, and *Swift* nowadays.

Several mechanisms combine to X-ray emission. During the fireball stage, once the shock reaches the top layer of the WD, the effective temperature goes up to $\sim 10^6$ K: the peak of the spectral energy distribution (SED) falls in the wavelength range of EUV and *soft* X-rays, ranging from 0.1 to 1 keV.

Always in the initial phase of the expansion, differential velocities of fragments and filaments in the ejecta is responsible for internal shocks: this mechanism leads to very high energy emission from *hard* X-rays (from 1 keV up to 0.1 MeV) to strong γ-rays (up to 100 GeV).

After the explosion, a large portion of the envelope is still gravitationally bound: this still hydrogen rich gas becomes fuel for a thin superficial layer on the WD where nuclear reactions are still active. The WD temperature is $\gtrsim 10^5$, thus being a soft X-rays source. Although the burning shell is very hot, the ejected expanding envelope may be so dense to completely obscure the super-soft central source. This phase is characterized by a "constant bolometric luminosity" (with $L \sim L_{Edd}$): the flux from the central source is redistributed within the ejecta, acting as a bolometer, while the surface area keeps on growing, thus pushing towards longer wavelength the peak of the SED. The steadily expansion of the ejecta eventually exposes the central source and the mass of the burning shell continuously decreases because of nuclear reactions, winds, or friction: the soft X-ray emission increases, then decreases.

Additional X-ray emission may come from the resumed accretion, for which only one clear example is known, i.e. V2487 Oph (Hernanz & Sala, 2002), where, besides a strong X-rays continuum, the fluorescent line Fe Kα was at $\sim$6 keV was measured, a common indicator of active accretion in magnetic CV. Compton degradation of radioactivity low energy ($\sim$MeV) γ emission may also account for X-ray emission during the initial stages of the outburst, although this mechanism has never been observed.

The study of the high energy emission from the WD and the ejecta is very important to understand the UV and optical development through all the stages of a nova, given the active role X-rays have on the ionization structure of the gas. γ-ray emission is discussed in V959 Mon chapter.

Chapter 4

T Pyxidis

T Pyx first eruption was recorded by H. Leavitt in 1890, reported in Leavitt & Pickering (1913), where they also noted that «*it may be necessary to revise the definition [of nova] to cover the possibility of there being more that one appearance*». Other five outbursts occurred, in 1902, 1920, 1944, 1966 and the ultimate 2011 eruption. The first four eruptions are described briefly in Payne-Gaposchkin (1957).

4.1 Recurrent novae

As already discussed, due to accretion of material on the WD even after an outburst, any classical nova will eventually undergo more explosive events. Recurrent novae undergo multiple outbursts on time scale less than $\sim 10^2$ yr (Schaefer, 2010): this is a mere historical definition, but different studies (Bode, 2010) suggest that novae on recurrence time scale of $\sim 10^3$ have not been observed yet. It is also suggested that RNe host massive WDs, allowing for less gas to be accreted to initiate a TNR. Equally, a high accretion rate is necessary. However, it is thought that a very high accretion rate will lead to an envelope on the WD with a low state of degeneracy and steady-state nuclear burning, thus denying the conditions for future TNRs (Fujimoto, 1982). Given the fundamental role of RNe in understanding CVs, these properties are continuously investigated in known recurrent systems.

The list of RNe is progressively growing, thanks to intense sky survey programs for both hemispheres. There is no need here to enlist all known RNe, but it is worth to summarize the classification scheme proposed by Anupama (2008), an attempt to subdivide RNe sharing specific phenomenological and physical properties. *Short period* RNe are characterized by close orbit systems, featuring heterogeneous behaviors and being physically comparable to CNe. *Long period* RNe, a class with only five objects, is very important because its members all show a Red Giant as donor star and very long orbital period.

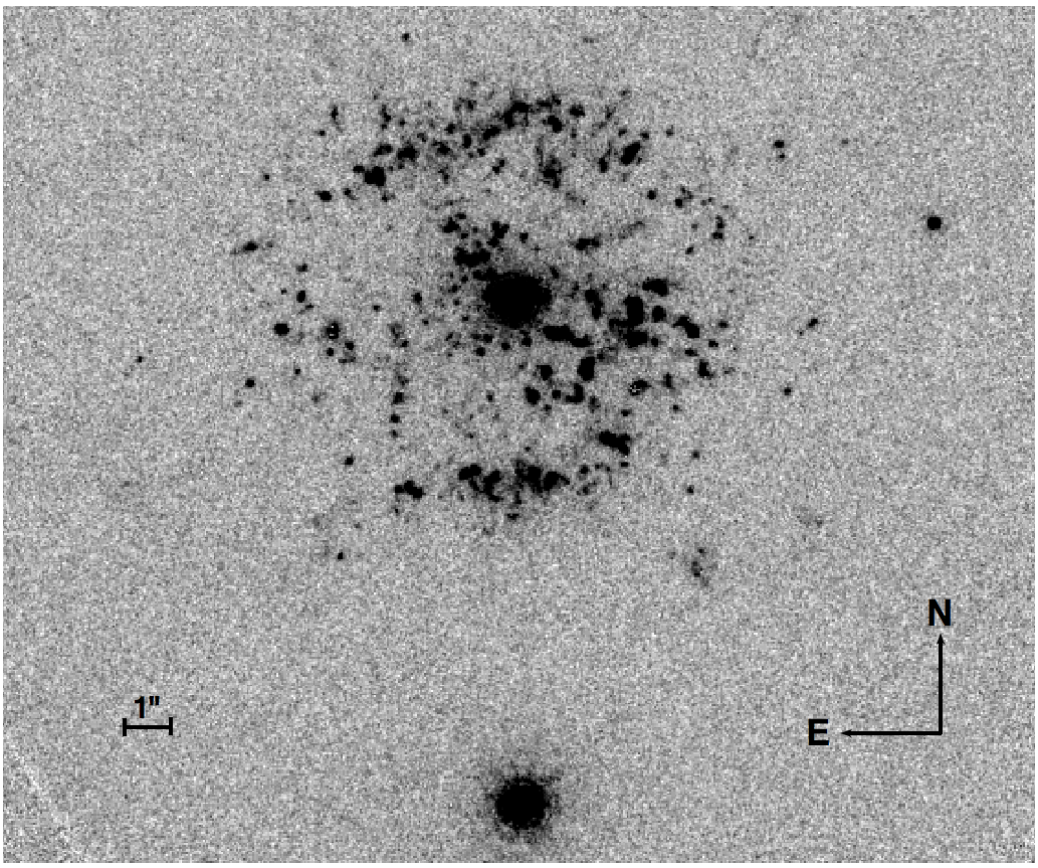

Figure 4.1: T Pyx remnant on 1994 Feb. 26, with HST/WFPC2, [N II] 658nm filter (Shara et al., 1997). T Pyx is the star in the middle, surrounded by the remnant. A bright star is near the bottom and a faint one close to the right margin.

4.2 T Pyx previous history

Since the 1966 eruption, T Pyx has been intensively investigated and its properties have been disputed for decades. Catchpole (1969) reported high resolution spectra (fig. 4.2) spanning over ∼400 days. The nova reached maximum V-magnitude 6.5 followed the typical spectral evolution: the first plates, ∼12 and 16 days after halt, show strong P Cyg profiles from Balmer lines and features from low ionization elements, O II, N II and Fe II; in later spectra, P Cyg profile disappear in favor of wide (velocity up to ∼2000 km s^{-1}) emission profile from Balmer lines, He I/II, N II/III, prominent [O III] lines. It is also reported, for the late stage, a feature associated with [Fe XIV]. Absorption features from Ca II H and K are also reported, with a radial velocity ∼20 km s^{-1}.

The subsequent outburst was awaited impatiently by the community and much has been said about T Pyx unusually prolonged quiescence, which is still a mystery. In the meanwhile, research has been focused in investigating the remnant from previous outbursts and the binary system properties.

The study of T Pyx remnant started with a Duerbeck & Seitter (1979) who reported an unexpected nebular shell, with a diameter ∼10 arcsec, around the central source. A

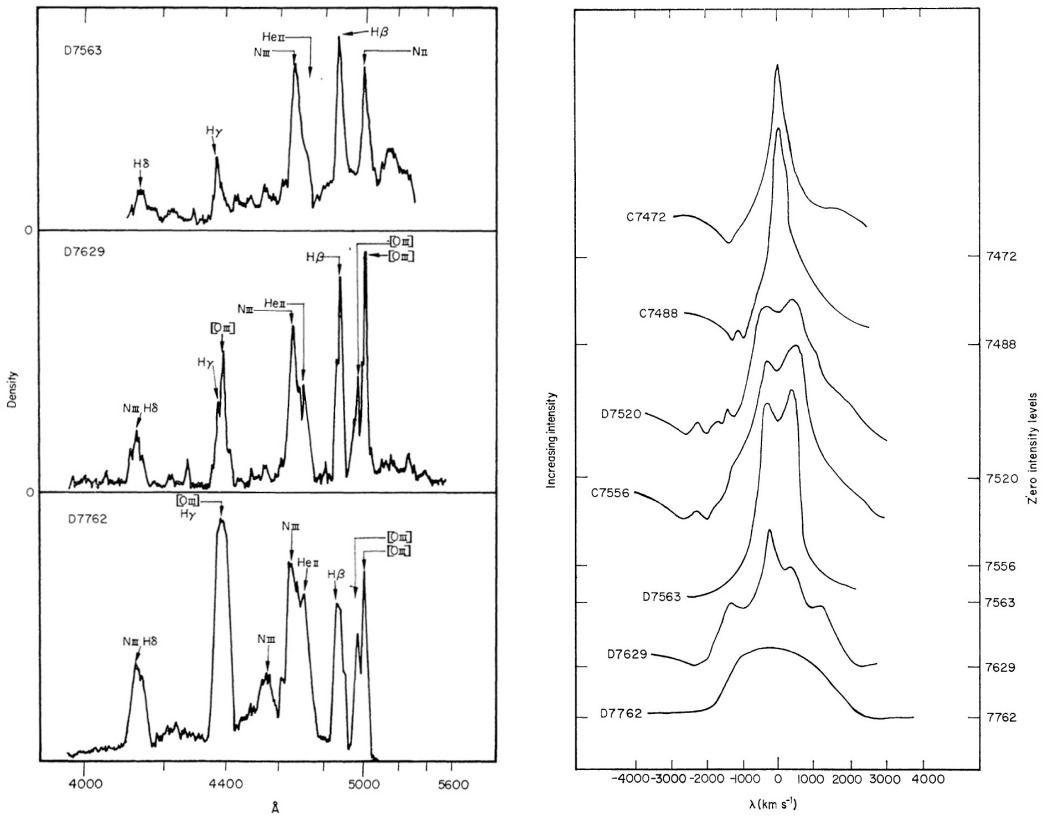

(a) Three spectra showing the transition to nebular stage (from top to bottom).

(b) Hβ time development, from top to bottom (each profile is labeled with the plate number).

Figure 4.2: Line profiles reported by Catchpole (1969).

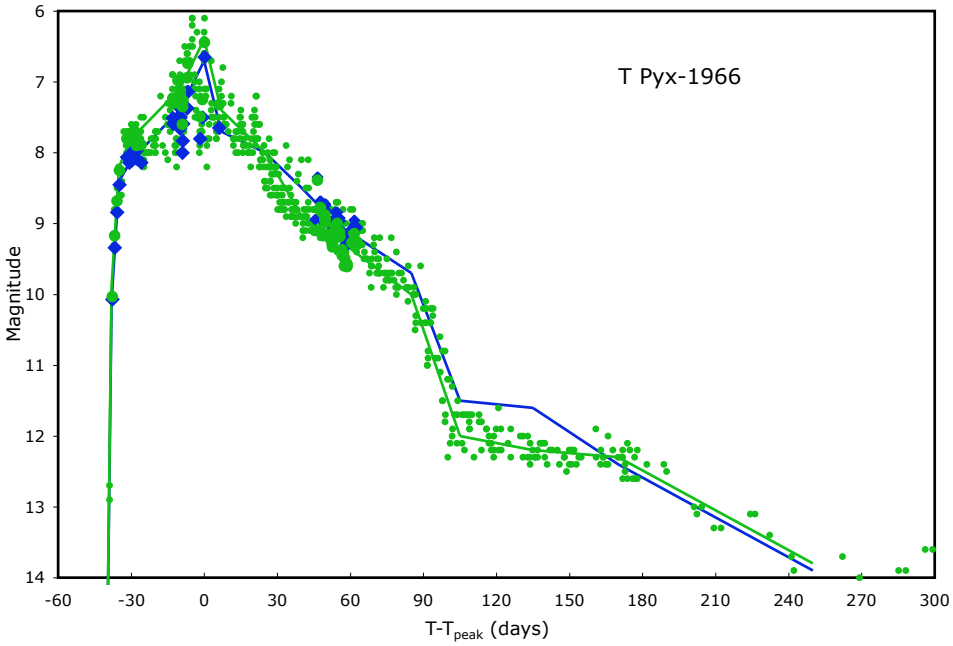

Figure 4.3: T Pyx 1966 outburst light curve reconstructed by Schaefer (2010). Diamonds for B-band, circles for V-band. The broken lines indicate the templates, highly smoothed sections of the light curves, with the gaps filled, used to compare the general light curve development of different outbursts.

detailed study of the remnant was conducted by Williams (1982): he could not clarify whether the shell originated from the 1966 or older eruptions, but reported spectral scans of the north portion of the shell that showed physical conditions similar to planetary nebulae. Shara et al. (1989) reported CCD imaging observations conducted until 1987 that showed how slowly the shell was expanding, velocity close to $\sim$350 km s^{-1} in disagreement with the values reported by Catchpole (1969), and an upper limit to its mass $\lesssim 10^{-4} M_{\odot}$, which is much less than a common planetary nebulae ejected mass, i.e. $\sim 0.1 M_{\odot}$ (it was doubted whether the remnant shell had a planetary nebula origin or not, being spectroscopically very similar to a usual planetary nebula). The distance and precise ejection date of the remnant remained basically unknown, but proposed 1 kpc as a consistent distance with 1966 as generation date of the shell, while the distance estimated with the MMRD was 1.5 kpc.

With HST/WFPC2 (*Hubble Space Telescope / Wide-Field Planetary Camera 2*) high angular resolution imaging (Shara et al., 1997), the complex structure of ejected material surrounding the system was finally seen (fig. 4.1), demonstrating that the shell is not a uniform expanding nebulosity but rather a complicated structure of knots, as already showed by other resolved novae remnants (HR Del, GK Per etc., for an extended review on resolved nova remnants see O'Brien & Bode, 2008)), each one of them showing variability in luminosity. Schaefer et al. (2010) then compared 2007 HST/WFPC2 images with previous data: their analysis suggests an old ejection event for the shell, which mass is estimated to be $\sim 3 \cdot 10^{-4} M_{\odot}$, perhaps originated by an 1866 missed outburst after a long period ($\sim 10^6$ yr) of quiet accretion and homologous expansion law for the knots.

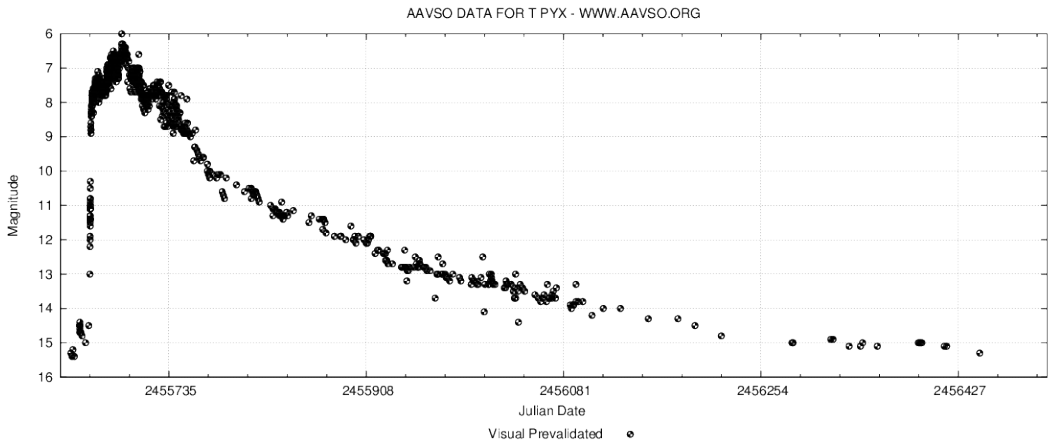

Figure 4.4: T Pyxidis visual light curve of the 2011 outburst (AAVSO) (Julian date).

Sokoloski et al. (2013) recently obtained an important result observing T Pyx light-echos from the 2011 outburst. With a one-year observational campaign conducted with the imaging facilities onboard the HST, they measured the time delays between the light from the central system and the scattering of light from dust present in the surrounding clumps of gas. The distance determined is 4.8 ± 0.5 kpc. This measurement confidently agrees with the results discussed here.

4.3 2011 outburst

The sixth historical outburst was discovered on 2011 April 14.29 MJD 2455665.79 (Waagan et al., 2011) at 13.0 visual magnitude. The AAVSO light curve is showed in fig. 4.4. It reached maximum magnitude on May 13, at V$\sim$ 6.5 mag, with a $\sim$2 months long phase of near-maximum brightness, followed by slow continuous fading.

Optical high resolution spectroscopy observation were conducted with the by the *Nordic Optical Telescope* (2.6 m, in La Palma) fiber-optic echelle spectrograph (NOT/FIES). In high resolution mode (0.023Å px^{-1}) the spectrograph covers the spectral interval from 3635 to 7364Å, while in medium resolution mode (0.035Å px^{-1}) the spectral range goes from 3680 to 7300Å. Two mid-resolution (0.04Å px^{-1}) spectra obtained at the *Very Large Telescope* (VLT) X-Shooter spectrograph, spectral range from 5500 to 10000Å on 2011 June 21 and 26 were downloaded from the ESO archive.

Ultraviolet spectra were obtained with Space Telescope Imaging Spectrograph (STIS) on-board the *Hubble Space Telescope* (HST). The instrument uses three gratings to observe the UV wavelength range: E140M for 1100-1750Å, E230M for 1600-2400Å, E230H for 2400-3000Å respectively with a resolution of 0.012, 0.026, and 0.012 Å px^{-1}.

The UV and optical spectra discussed here have been reported in Shore et al. (2011, 2013b) and De Gennaro Aquino et al. (2013). The journal of observations is reported in tab. 4.1.

NOT/FIES Date	JD 2450000+ [Day]		t_{exp} (sec)
2011 Apr. 15	5667.42 [2]		600
2011 Apr. 23	5675.46 [10]		600
2011 May 6	5688.38 [23]		600
2011 May 8	5690.37 [25]		60
2011 May 15	5697.38 [32]		600
2011 May 21	5703.37 [38]		600
2011 May 30	5712.38 [47]		900
2011 Oct. 10	5845.74 [180]		600
2012 Apr. 8	6026.37 [360]		3600
VLT/X-Shooter Date	JD 2450000+		t_{exp} (sec)
2011 June 21	5733.980 [68]		20
2011 June 26	5738.976 [73]		20
HST/STIS OBSID	JD 2450000+	Grating	t_{exp} (sec)
2011 May 06 [day 23]			
OBG101010	5688.335	E140M	571
OBG101020	5688.345	E230M	571
OBG101030	5688.356	E230H	571
2011 July 28 [day 105]			
OBG199010	5770.786	E140M	285
OBG199020	5770.794	E230M	285
OBG199030	5770.801	E230H	35
2011 Oct. 04 [day 173]			
OBG103010	5838.540	E140M	600
OBG103020	5838.552	E230M	600
OBG103040	5838.567	E230H	155
2012 Mar. 28 [day 349]			
OBX701010	6014.643	E140M	2457
OBX701020	6014.702	E140M	3023
2012 Dec. 21 [day 617]			
OBXS01010	6282.221	E140M	2449
OBXS01020	6282.279	E140M	3015
2013 July 26 [day 834]			
OBXS03010	6499.875	E140M	2449
OBXS03020	6499.917	E140M	3015

Table 4.1: Journal of T Pyx observations.

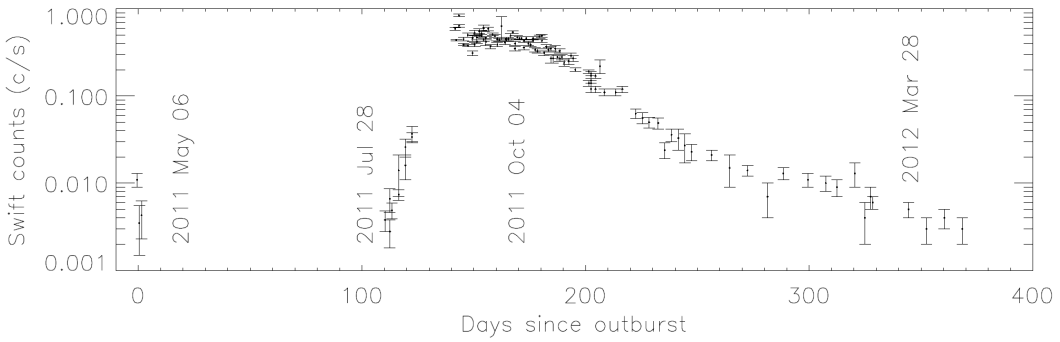

Figure 4.5: T Pyxidis SWIFT/XRT of the 2011 outburst, with HST observations dates marked.

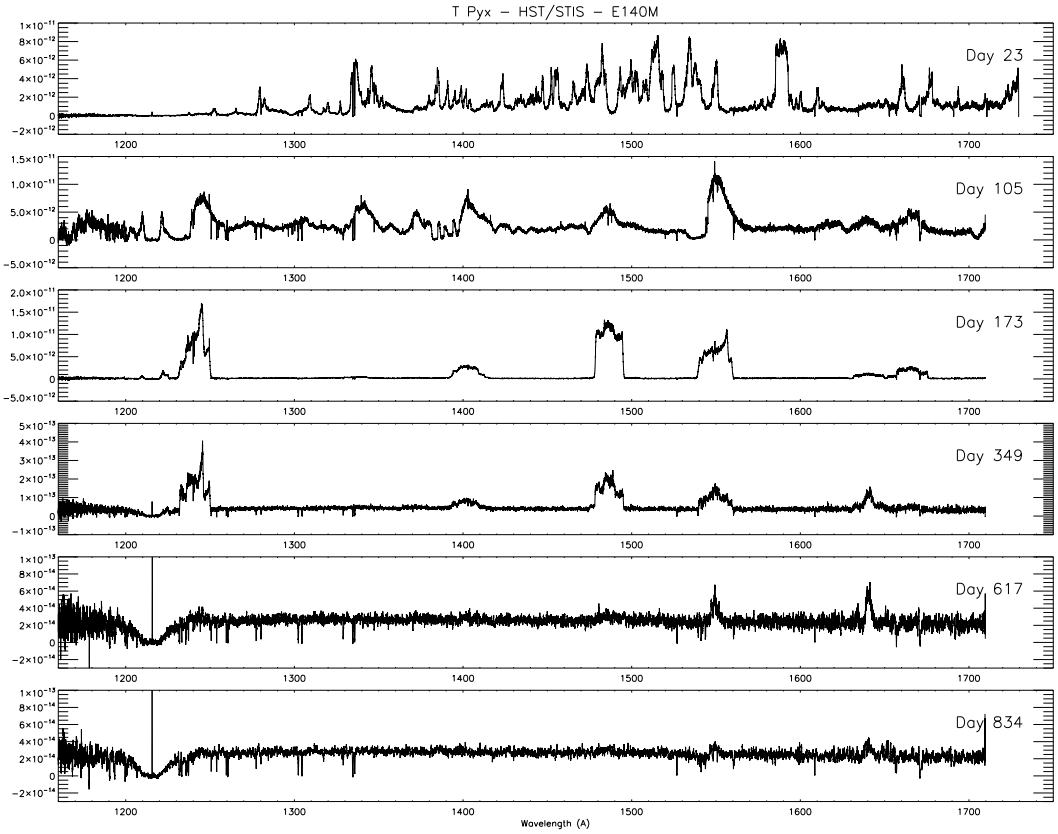

Figure 4.6: T Pyxidis 2011 HST/STIS spectra with E140M grating (1200Å- 1700Å). From top to bottom: day 23, May 6th 2011, observed during the iron curtain, main features are *pseudo*-emissions between optically thick bands by low ionization species; day 105, July 28th 2011, observed during the transition phase, several P Cyg lines, from resonance and intercombination transitions; day 173, Oct. 4th 2011, nebular phase, optically thin emission lines; day 349, Mar. 28th 2012, nebular phase, but emission lines evolved; day 617, Dec. 21st 2012, late phase, weak residual line emissions, ejecta absorption features from N V 1240Å and C IV 1550Å; day 834, July 26th 2013, late phase, ejecta absorption features evolved.

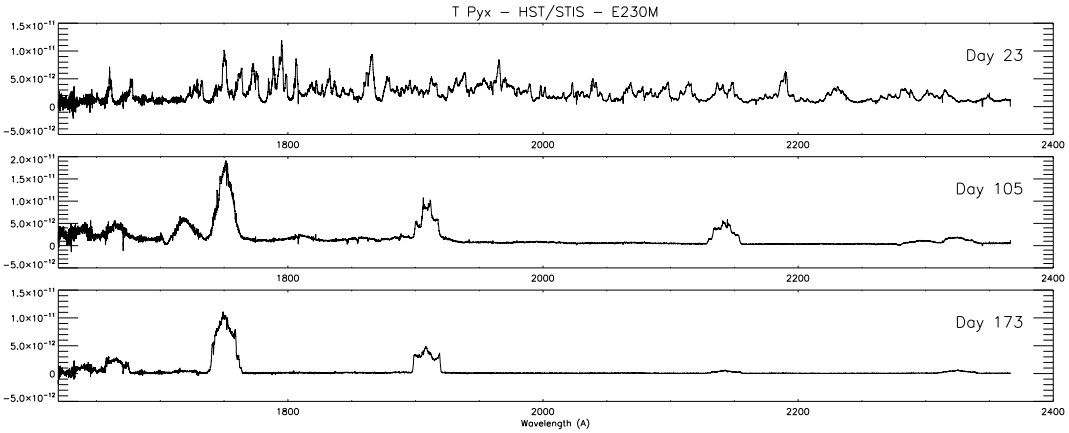

Figure 4.7: T Pyxidis 2011 HST/STIS spectra with E230M grating (1700Å- 2400Å). Same sequence as in fig. 4.6, but only for the first three epochs covered.

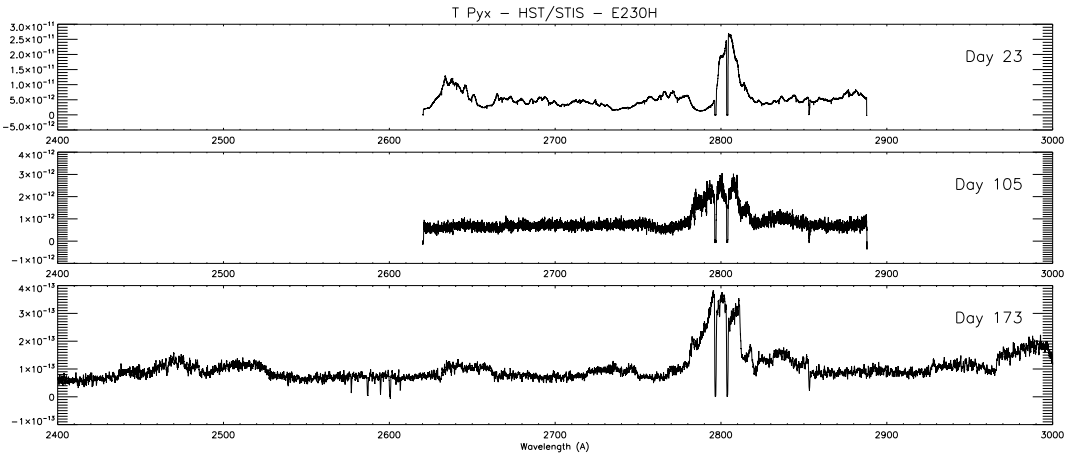

Figure 4.8: T Pyxidis 2011 HST/STIS spectra with E230H grating (2400Å- 3000Å). Same sequence as in fig. 4.6, but only for the first three epochs covered. Prominent feature is always the Mg II 2800Å doublet.

4.3.1 Fireball and Fe-curtain phase

The first optical and UV observations were conducted during the optically thick phase. Shore et al. (2011) analyzed the first 50 days of the optical spectral development (from the end of June 2011, T Pyx was too close to the Sun to be observed[1]). In De Gennaro Aquino et al. (2013) we then reported the analysis of day 23 HST/STIS observation.

The first optical high-resolution spectrum was obtained with NOT/FIES on April 15, only $\sim$2 days after the outburst, during the fireball phase. It was characterized by many P Cyg lines from H I and He I/II, with the absorption extended up to -2500 km s^{-1}, with a smooth terminal edge. Subsequent NOT spectra were instead characterized by many other lines from low ionization metals, i.e. Fe II, Ca II H and K and Na I, all showing complex and evolving P Cyg absorptions. The line profiles, which initially resembled a simple smooth P Cyg, broke into distinct absorptions, which number, saturation, central velocity and width varied with time, moving progressively towards higher negative velocities. The Hα development is displayed in fig. 4.9: the initial smooth, unsaturated P Cyg absorption, subsequently developed different broad, optically thick absorption structures; it is worth to notice that the negative velocity edge always showed a smooth decrease from the continuum to the saturated absorption. The He I 5786Å and Na I doublet development is showed in fig. 4.10: with the narrow interstellar features from sodium always visible, the first spectrum on day 2 showed only P Cyg absorption from He I, subsequently also sodium recombined, showing initially two broad absorptions features which then broke into several narrower features. Several DIBs were observed and using the correlation relationship between several DIBs equivalent widths and the

[1]The Sun and the seasons are well known to astronomers, but novae explode whenever they want. For novae very close to the ecliptic, there's always a time window during the year where they cannot be observed with telescopes (Fermi/LAT is an important exception). And until few decades ago, novae located in the southern hemisphere were poorly followed (the Cerro Tololo atlas by Williams et al. (1994) and the SMARTS Atlas by Walter et al. (2012) are remarkable achievements). In this picture, space telescopes have privileged positions, but very limited accessible time.

extinction (Friedman et al., 2011), it was obtained, independently of distance, and extinction of E(B-V)=0.49±0.17.

The first HST/STIS observation on day 23 shows how strong the Fe II curtain was (first panel in figures 4.6, 4.7, 4.8). The spectrum is densely populated by pseudo-emissions produced by spectral windows of low opacity between optically thick absorption bands from Fe II and other low ionization species (S I, C I etc), resulting from the combination of line distribution and velocity gradient of the ejecta. Only few features are identifiable as emission profiles, i.e. the Mg II 2800Å doublet, with a P Cyg profile extending to -2000 km s^{-1}, and very weak line emission from O I 1302Å, C II 1334Å doublet, and N II 2145Å.

An important measurement in this phase is the unreddened "bolometric" luminosity: we actually consider only UV and optical wavelengths. The unreddened flux measured in the range from 1200 to 7300Å is $3.2 \pm 0.2 \times 10^{-8}$ erg s^{-1} cm^{-2}, which represents a lower limit because of non complete wavelength coverage. Using 5 kpc as distance, we obtain a corrected luminosity of $\gtrsim 2.5 \times 10^5\, L_\odot$. This value is very large, much higher than the Eddington luminosity. Using lower values for extinction and distances, E(B-V)=0.3 and 3 kpc, as proposed by Selvelli et al. (2008), we obtain $3.3 \times 10^4\, L_\odot$, which is still a very high luminosity; a similar value is provided by the MMRD relation (Della Valle & Livio, 1995) with $t_2 = 32$ days.

These considerations suggests a very massive WD, $M_{WD} \sim 1.3 \pm 0.2\, M_\odot$ close to the Chandrasekhar limit, a result in agreement with the theoretical statement of RNe hosting massive WDs. These results contradict the orbital parameters measured by Uthas et al. (2010): their main result is the spectroscopic determination of the orbital period, i.e. P_{orb}=1.83 hrs, but they also estimated the inclination of the system, $i \approx 10$ deg (which is similar to the value discussed below), and the masses of the stars, with the mass ratio being $q = 0.20 \pm 0.03$ and the WD mass being $M_1 = 0.7 \pm 0.2\, M_\odot$, a value substantially lower than our estimate.

The first UV and optical spectra are extremely useful for understanding the physical processes of the early expansion, and to unambiguously explain the evolution of the moving narrow absorption features, a long-standing problem in novae optical spectroscopy (McLaughlin 1954, Payne-Gaposchkin 1957, Hutchings 1970, Cassatella et al. 2004b). The ejecta, after the initial complete ionization phase (the fireball), eventually expands and cools and recombination starts: the UV iron curtain and the P Cyg lines from Balmer and lowly ionized species in the optical wavelength range perfectly show this stage. The recombination front moves outward in the expanding ejecta, progressively tracing higher velocities portion of the ejecta: the absorption moves blueward. The ionization of parcels or filaments of gas, structures that are frozen in at the time of the outburst in the ballistic ejection hypothesis, then follows the global changes: substructures on the line of sight will be visible as narrow features in the P Cyg structure.

T Pyx, since the first X-ray detection by Swift (Kuulkers et al., 2011), was continuously monitored (fig. 4.5). It became X-ray invisible few days after the outburst, a condition that lasted for more than 3 months.

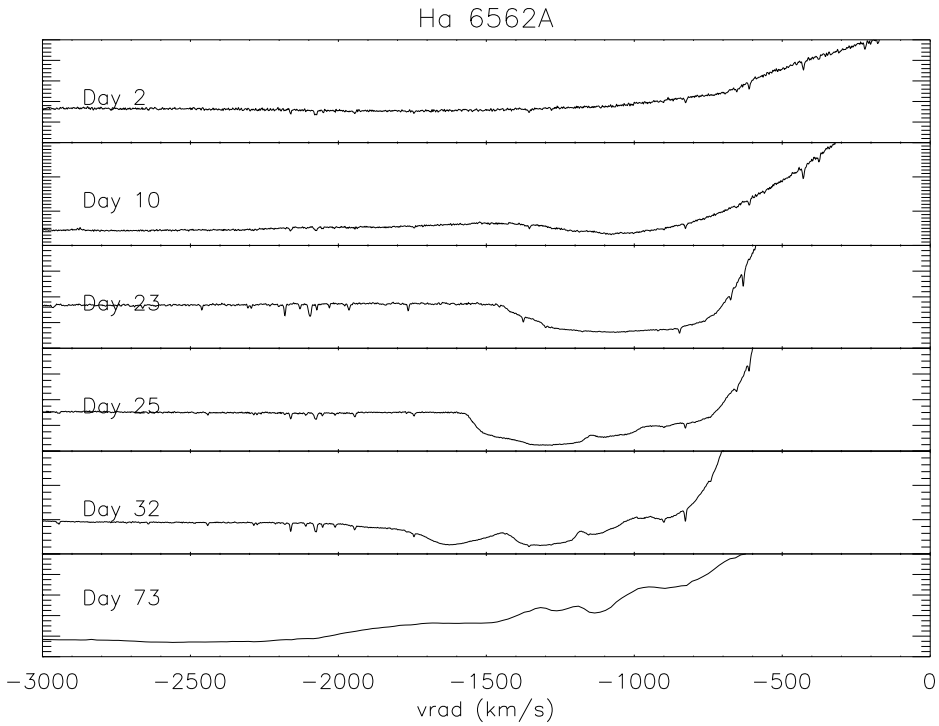

Figure 4.9: The development of the P Cyg profile, only the absorption region, of Hα from the fireball to the transition phase.

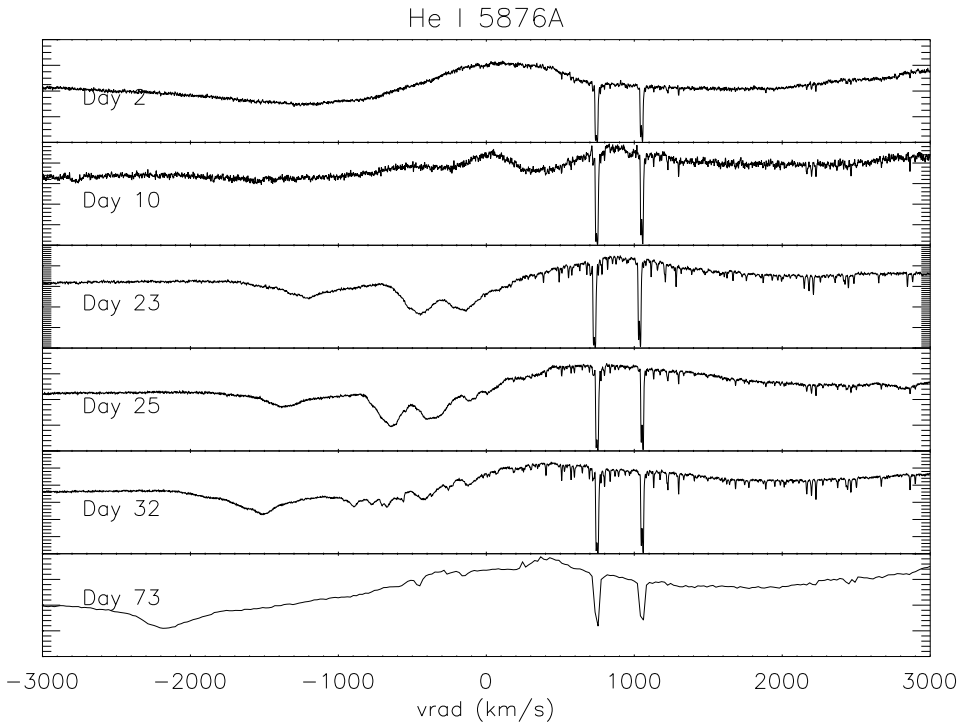

Figure 4.10: The development of the P Cyg profile of He I 5876Å from the fireball to the transition phase. The stationary narrow lines on the red side are the interstellar neutral sodium D1 and D2 doublet.

4.3.2 Transition to nebular phase

The ejecta remained optically thick for a very long time: the second HST/STIS passage, on Day 105 after the outburst (second panel in figures 4.6, 4.7, 4.8), reveals strong P Cyg line from resonance lines, the doublets from N V 1240Å Si IV 1400Å, C IV 1550Å and Mg II 2800Å, and intercombination lines, N IV] 1486Å, O III] 1667Å, C III] 1909Å, N II] 2145Å, and C II] 2324Å, which mark the transition phase to the nebular phase. Optical spectra obtained with X-Shooter on 2011 June 21 and 26 (Day 68 and 73), in the wavelength range 5500-10200Å, are extremely useful to cover the evolution of several transitions, like Hα, He I 5875Å etc, and to explain the development of the line profiles from CNO ions.

As already mentioned, the UV spectrum is characterized by prominent P Cyg profiles by strong resonance lines. N V and C IV present the most extended absorption, up to -3500 km s^{-1} with almost complete saturation from -2000 to -1000 km s^{-1}. The maximum negative velocity in these lines is higher than the one observed for the optical recombination lines during the initial phase: we can explain it as a combined effect of the very high oscillation strength of the transitions and especially the almost complete passage of the recombination front (which, emphasizing again, is not a dynamic front). The velocity profile on the blue side is not sharp but presents a gradual shading, something that cannot be observed with a wind-like outflow. The Si IV 1400Å presents a structured P Cyg profile with two main detached broad absorption components ranging from -2300 to -1900 km s^{-1} and -1800 to -1300 km s^{-1}, even though the appearance of the profile is rather complicated given the separation of the two transitions of the doublet (1393.76Å and 1402.77Å, which are separated by $\sim$ 2000 km s^{-1}). This is the same structure observed for Ca II lines in the early phase spectra, and it shows that for different species, tracing different ionizations both in space and time, the structure was fixed since the initial stages of event.

Several narrow absorption features from lowly ionized species, i.e. N I, O I, Si II, Mg II and Al III, are observed at the same negative velocity of -1330 km s^{-1}: more details below.

Along with resonance permitted lines, other transitions, from ground and excited states, showed P Cyg profile with similar high velocities, the prominent line being N IV] 1486Å. This is a rather rare observation: at this stage, i.e. the "lifting" of the Fe II curtain, only ONe novae (V1974 Cyg, V382 Vel, LMC 1990#1) and the recurrent U Sco 1979 displayed this feature. Before going into the details of the observed transitions, it's important to notice again the X-ray data from Day 105: there was no Swift detection. Along with ground state intercombination transitions, the simultaneous observation of detached P Cyg profiles from highly excited states of CNO, i.e. C III 2296, N IV 1718, and O V 1371Å, has *never* been observed. The non-saturated absorption for C III 2296 and N IV 1718Å extends from -2200 to -1800 km s^{-1}, with the O V 1371Å clearly present but showing a rather different profile: the ionization energy of O^{+4} is 77 eV, which is much higher than 24 eV and 47 eV required respectively for C^{+2} and N^{+3}. It is extremely useful here to report the partial Grotrian diagram of the iso-electronic

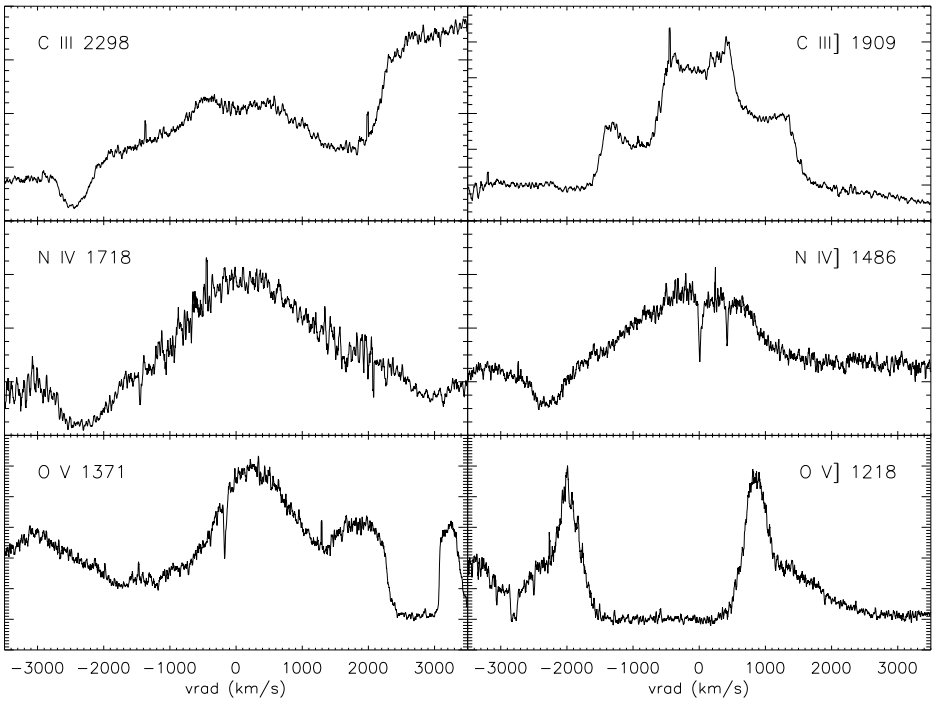

Figure 4.11: C^{+2}, N^{+3} and O^{+4} iso-electronic lines observed in on day 105, during the transition phase (relative sample Grotrian diagram in fig. 4.12). Details in text. Flux rescaled for all profiles.

transitions (fig. 4.12). Far-UV photons were radiatively populating the upper levels: this indicates the presence of a strong, optically thick source shortward of 1000Å. The detached P Cyg covers a limited velocity interval, with respect to C IV and N IV for instance, thus showing that the absorption was produced on the line of sight to the WD, and FUV was optically thick only in that region. The X-Shooter optical spectrum, although observed a month earlier, reveals the same profile for He I 5785Å and N II] 5676Å. The transition C III] 1909Å shows no P Cyg absorption, with the profile being almost identical to the Hα: this can be explained by the combined effect of optical depth decreasing at higher wavelength and the low transition probability.

The observed UV transitions provide a remarkably good description of the ionization structure and irradiation condition of the ejecta: a schematic diagram of the velocity range covered by the absorption features from P Cyg or narrow components is displayed in fig. 4.37 (the diagram include features observed in later time, discussed below). The X-ray invisibility of the nova in this stage (it was not detected by Swift until 110 days after the outburst) indicates the high optical depth of the ejecta, and the CNO iso-electronic P Cyg profiles from excited states transitions, perfectly agrees with this interpretation.

High velocity narrow features

Through the identification and measurement of UV interstellar lines it was possible to identify narrow absorption features, with FWHM$\sim$100 km s^{-1}, on most strong resonance transitions of neutral and singly ionized heavy elements. These lines, displayed

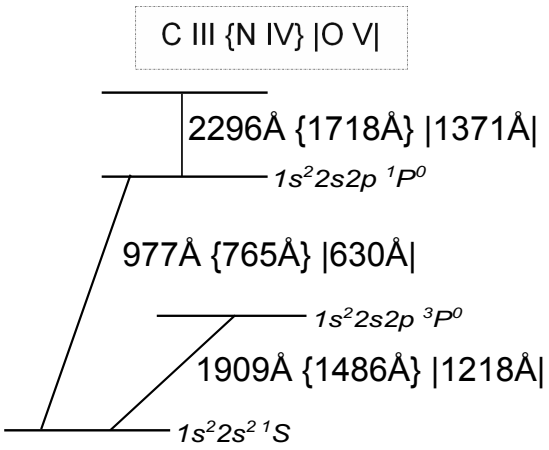

Figure 4.12: Schematic sample Grotrian diagram of the isoelectronic transitions of C^{+2}, N^{+3}, and O^{+4} that display detached P Cyg profiles during the transition stage. The resonance lines are also indicated and the FUV exciting transitions.

at -1300 km s^{-1}, are easily identifiable and distinguishable from ISM features if we compare the spectrum from Day 105 with, for instance, Day 23 or Day 173 spectra (figures 4.13, 4.14, 4.15). Transitions from fine structure states with excitation energy below 0.1 eV were present for which no interstellar counterpart was visible. The equivalent widths of these features were measured (table 4.2) and the derived column densities are listed in table 4.3 (the technique used here is discussed in the next section about the interstellar medium). In the approximation of a single cloud producing the narrow absorption at -1330 km s^{-1}, the curve of growth model, built on the ground state transitions measurements, gives a b value (the velocity width of the Gaussian profile of the line) of 22 km s^{-1}, with a $\chi^2/(dof) \sim 0.7$ (fig. 4.16). This calculation shows confidently that the narrow absorptions originated in a similar environment, i.e. a little parcel of gas on the line of sight. It should be noted the unusual ratio of Si and Mg column densities, N(Si II)/N(Mg II)$\sim$10$\pm$3. Comparing this result to the interstellar value, N(Si II)$_{ISM}$/N(Mg II)$_{ISM}\sim$1 (section below) and the reference solar value, N(Si)$_\odot$/N(Mg)$_\odot$=0.9 (Asplund et al., 2009), we may have found another evidence of mixing+nucleosynthesis during the TNR, with the chemical composition of the ejecta substantially changed with the respect to the solar-like accreted material: from 1D models by José & Hernanz (1998), we find that the CO4 simulation, with a 1.15 $M_\odot$ CO WD and a 25% abundances pre-TNR mixing between the WD core and the solar-like accreted envelope, finally leads to a mass fraction of magnesium of 1.2×10^{-4} and a silicon yield of 9.8×10^{-4}, hence a Si-to-Mg mass fraction ratio of $\sim$8 (in all CO WD simulations conducted, the final Si mass fraction is at least 2 times higher than Mg).

4.3.3 Nebular stage

The nebular phase development was followed with HST/STIS and NOT and discussed in Shore et al. (2013a) and De Gennaro Aquino et al. (2013). The analysis has been conducted on the observations taken almost simultaneously at both facilities on days $\sim$180

Species	Wavelength (Å)	f-value	Eq.Width (mÅ)	Vel.range (km s^{-1})
Si II	1193.29	0.575	210 ± 40	-1390 ; -1260
Si II	1194.50*	0.737		-1380 ; -1260
Si II	1197.39*	0.150	165 ± 30	-1430 ; -1260
N I	1199.55	0.132		-1420 ; -1240
N I	1200.22	0.0869	105 ± 20	-1380 ; -1270
N I	1200.71	0.0432	111 ± 20	-1390 ; -1260
Si II	1260.42	1.22	320 ± 20	-1470 ; -1250
Si II	1264.73*	1.09	bl. S II 1259Å (ISM)	-1470 ; -1280
O I	1302.17	0.0520	128 ± 15	-1380 ; -1270
Si II	1304.37	0.0928	92 ± 15	-1360 ; -1260
O I	1304.86*	0.0518	103 ± 20	-1360 ; -1280
O I	1306.03**	0.0519	90 ± 20	-1380 ; -1270
Si II	1309.27*	0.0800	86 ± 15	-1520 ; -1260
Si II	1526.71	0.133	185 ± 25	-1410 ; -1290
Si II	1533.45*	0.133	bl. Si II 1527Å (ISM)	–
Al III	1854.72	0.557	682 ± 40	-1540 ; -1170
Al III	1862.79	0.227	bl. Al III 1854Å (ISM)	-1480 ; -1170
Mg II	2796.35	0.608	231 ± 40	-1360 ; -1280
Mg II	2803.53	0.303	158 ± 50	-1370 ; -1280

Table 4.2: Equivalent widths for the negative velocity narrow features observed on day 105 with velocity ranges.

Species	-1σ	Log N (cm^{-2})	+1σ
Al III	15.35	15.65	15.98
Mg II	12.76	12.90	13.02
N I	14.15	14.27	14.38
O I	14.16	14.19	14.26
O I* (E=0.019 eV)	14.03	14.12	14.20
O I** (E=0.028 eV)	13.95	14.06	14.15
Si II	13.86	13.99	14.12
Si II* (E=0.035 eV)	13.79	13.90	14.00

Table 4.3: Derived column densities for the features reported in tab. 4.2.

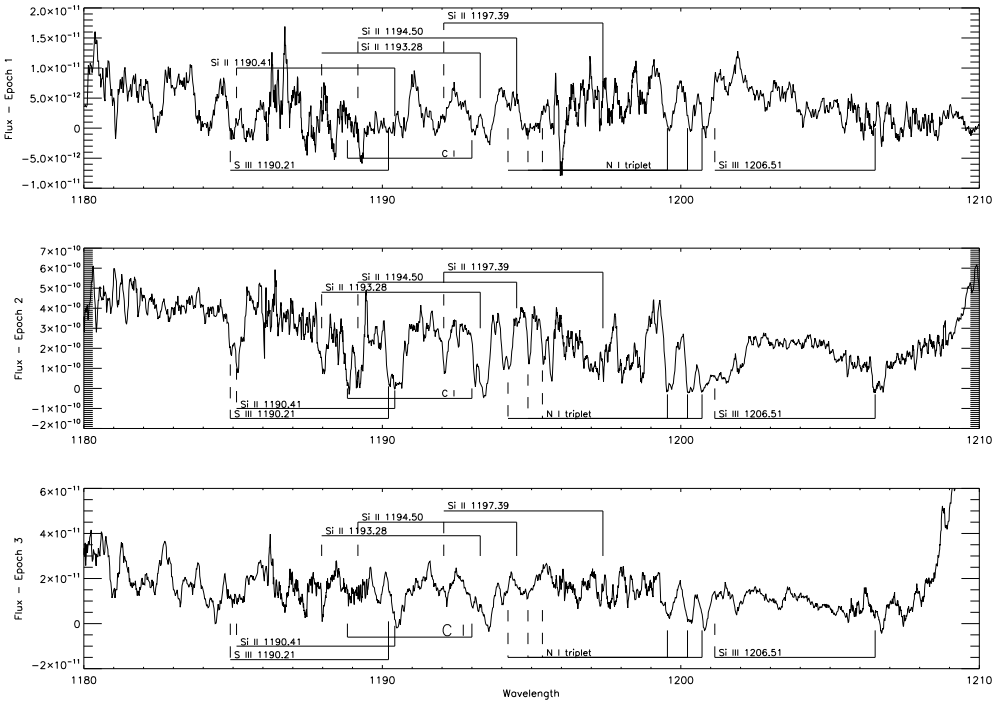

Figure 4.13: The development of the wavelength range 1180-1210Å during the first three epochs (top to bottom: days 23, 105, and 173). The high velocity (-1330 km s^{-1}) narrow absorption component is indicated with a link to the rest wavelength (in most cases the interstellar contribution). Note that narrow displaced absorption was also detected for transitions that did not display interstellar components, those from fine structure excited states.

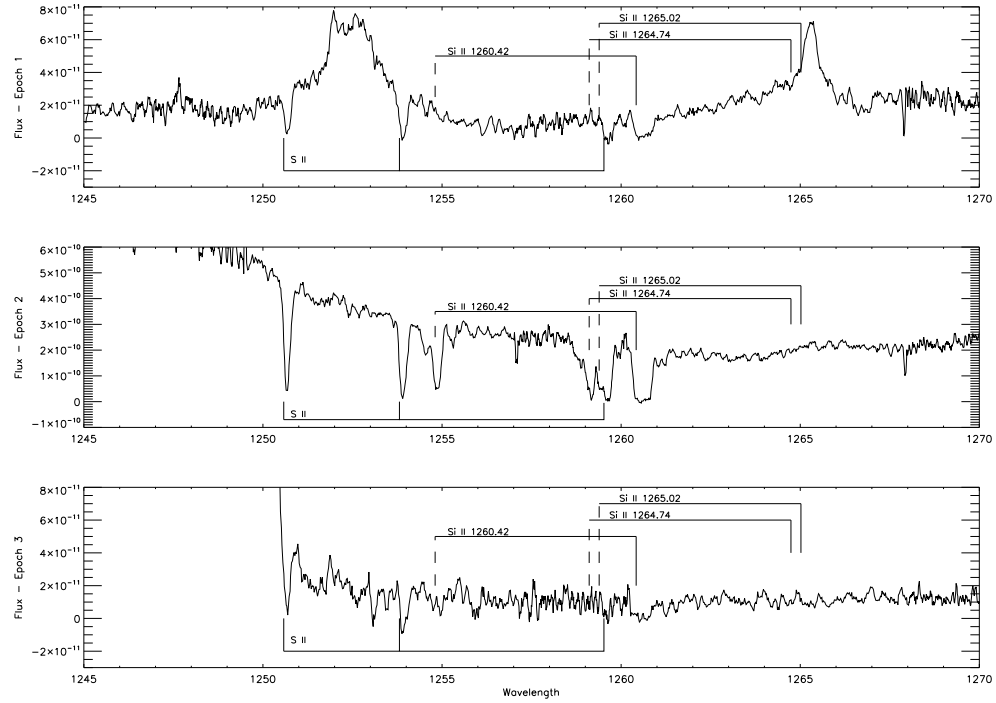

Figure 4.14: Same as in fig. 4.13 but in the wavelength range 1245-1270Å.

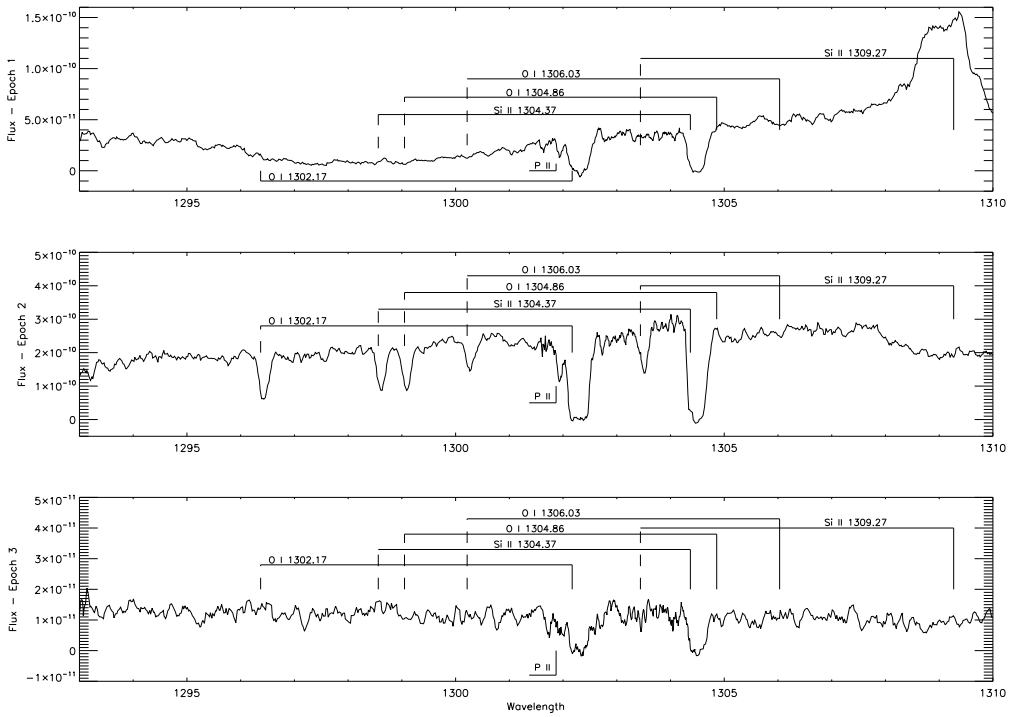

Figure 4.15: Same as in fig. 4.13 but in the wavelength range 1293-1310Å.

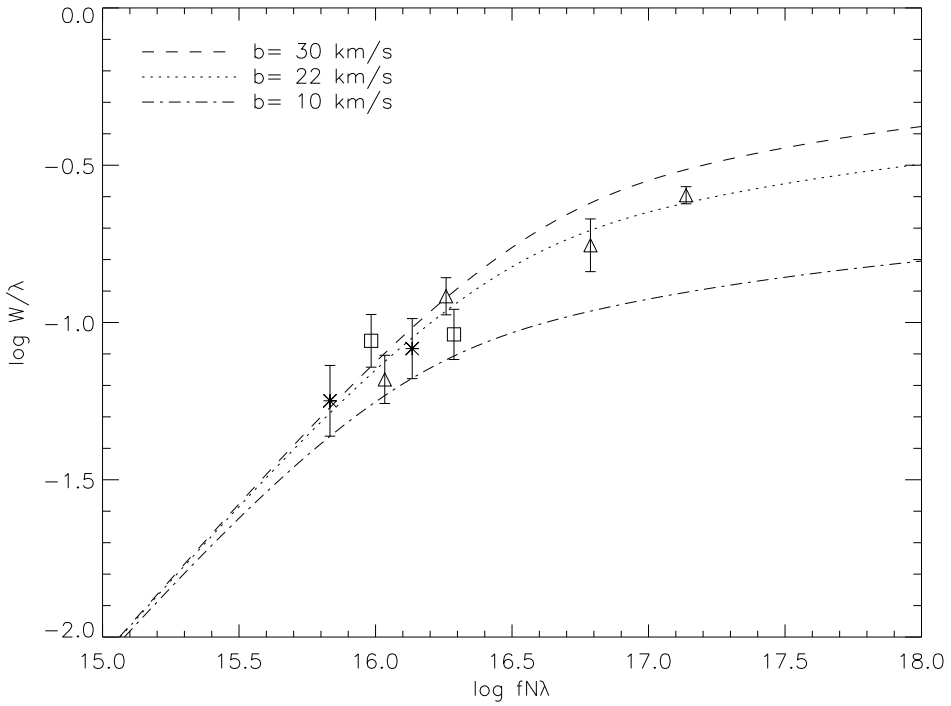

Figure 4.16: Curve of growth for the narrow high velocity absorption lines from the metallic ions, column densities derived listed in table 4.3. Si II triangles, N I squares, and Mg II stars.

and ∼350 after the outburst: at this stage, the small temporal difference, i.e. few days, between NOT and STIS spectra does not account for any physically meaningful change in the spectrum, so that we treated the UV and optical spectra as simultaneous for each epoch (hereafter we refer to them as day 180 and day 350 epochs). Few important differences are indeed observed between the two epochs. Unfortunately, March 2012 HST/STIS observation was conducted only with the short wavelength E140M grating.

The optical G430L STIS spectrum was used to calibrate the epoch 1 NOT observation by convolving the spectrum following median filtering to the STIS resolution (about 3) and using a third order fit to the strongest lines from 3300-5700Å. A low resolution SMARTS spectrum from 2012 April 2 was used to absolutely calibrate the NOT spectrum from April 8.

The fluxes were dereddened using E(B-V)=0.50±0.5. This value was obtained measuring the interstellar H column density from the absorption profile of the Lyman α emission (Hβ profile as model) and then using the E(B-V)/N_H calibration (Guever & Oezel, 2009). This value is in agreement with the E(B-V) estimate obtained with the DIBs equivalent widths relationship.

For both epochs it is important to notice the development of the X-ray emission from the central WD (fig. 4.5). Day ∼180 spectra were taken when the soft X-ray emission was close to the peak, while day ∼350 observations were conducted when very weak X-ray emission was left, at the end of the SSS phase.

X-ray peak stage - day 180

Day 180 UV spectrum (third panel in figures 4.6, 4.7, 4.8) presented a weak continuum, no blueshifted absorption components and a multitude of emission lines. Lyα was heavily damped and contaminated on the red side by the O V] 1218Å emission line. The N V and C IV doublets profiles presented strong emission and no P Cyg absorption, with marked emission on the red side of the lines (these transitions are discussed with details below). Si IV 1400Å resonance doublet was blended with the S IV] lines. N IV] 1486Å line presented a double-top emission profile, almost identical to the iso-electronic resonance intercombination transition of C III] 1909Å, which in turn were very similar to Hβ (fig. 4.22). The O V] 1218Å iso-electronic line was, as already mentioned, heavily blended by the Lyα (panel (a) in fig. 4.17). O V 1371Å was also weak but present. Weak emission from N II] 2145Å and C II] 2324Å was still visible while O III] 1667Å was as strong as the Si IV/S IV] blend.

He II 1640Å was visible, with an almost identical profile to He II 4686Å(fig. 4.23).

The optical spectrum from NOT showed several line from the Balmer series, Hα, β and γ, and helium, He I lines 5875, 6678 and 7065Å, the already mentioned He II 4686Å but blended with the N III multiplet at 4640Å. Important lines for nebular spectroscopic diagnostics were also visible, [O III] 4363, 4959, and 5007Å, and the [N II] 5755, 6548 and 6583Å, the latter being heavily blended with Hα. We identified the emission lines at wavelengths 5309 and 6086Å as [Ca V] lines, but it is not certain (the 5309Å profile is anomalous, and 6086Å could suffer contamination from [Fe VII] 6087Å).

X-ray source off - day 350

For UV spectrum on day 350 (4th panel in figure 4.6), the UV emission lines found in day 180 E140M spectrum were all there, exception for O III] 1667Å and O V 1371Å being disappeared. However, all the profiles slightly changed (fig. 4.17 and 4.18). In the optical spectrum, only the He I lines disappeared. Also for the optical transitions, the lines profiles changed with respect to day 180 (figures from 4.17 to 4.22).

The resonance doublets C IV and N V are discussed in a proper section. The other transitions showed a double top profiles on day 180 spectrum, with the exception of the complex profiles from [Ca V] transitions, but on day 350 spectrum, the central emission core was prominent with respect to the broad shoulders, which in sames cases were very faint, e.g. [N II] 5755Å.

Electron density and filling factor of the ejecta

Between both epochs, although He II 4686Å was blended with N III 4640Å multiplet, the lines profile matches almost perfectly (fig. 4.23). On day 180 spectrum, the lines showed a double top profile, with the central core extended to $|v_{rad}| \leq 500$ km s^{-1} and broad emission up to $|v_{rad}| \sim 2000$ km s^{-1}; on day 350, the central core showed prominent emission with respect to a weak residual pedestal emission. Once applied the extinction correction, with E(B-V)=0.5, for day 180 spectrum the dereddened fluxes are $j_{1640} = 5.0 \pm 0.1 \times 10^{-10}$ and $j_{4686} = 3.0 \pm 0.2 \times 10^{-11}$ erg s^{-1} cm^{-2}, resulting in the ratio $j_{1640}/j_{4686}(day\,180) \approx 16.6 \pm 0.2$; for day 350, $j_{1640} = 2.3 \pm 0.1 \times 10^{-11}$ and $j_{4686} = 1.9 \pm 0.2 \times 10^{-12}$ erg s^{-1} cm^{-2}, hence the ratio is $j_{1640}/j_{4686}(day\,350) \approx 12.1 \pm 0.2$. This results is consistent with the hypothesis of constant mass ejecta.

The [O III] 4363, 4959, 5007Å lines were present in both epochs without any severe blending, only a partial blend for [O III] 4365Å and Hγ 4640Å. To remove it, we scaled the Hβ profile to the Hγ and remove it to obtain a clear [O III] 4363Å profile. [N II] 6583Å was very weak in day 180 spectrum but clearly present on the red wing of the Hα (panel (c) in fig. 4.19), so we used the Hβ profile to disentangle the [N II] line at 6583Å from the Hα (the [N II] 6548Å was never clearly detected). We then estimated the electron density and temperature radial profile using the [O III] and [N II] optical lines diagnostic (see appendix for details), taking the ratios of the lines fluxes $(j_{4959} + j_{5007})/j_{4363}$ and $(j_{6548} + j_{6583})/j_{5755}$, in order to obtain a consistency check on both diagnostics tools. It must be noted that extinction is an important parameter here, given the large wavelength differences between the used transitions. For the temperature range $1 \leq T_e/10^4\,(K) \leq 4$, the [O III] ratio gives $0.9 \leq n_e/10^7\,(cm^{-3}) \leq 5.4$, while the [N II] gives $1.4 \leq n_e/10^6\,(cm^{-3}) \leq 4.9$, hence the two diagnostics are not consistent with each other: the reason is the high uncertainty on the [N II] lines profiles.

On day 350 spectrum, the [N II] 6583Å was much stronger, and the blending with Hα was easier (fig. 4.25), so using the same technique we have a consistent single set of parameters: $T_e = 3.9 \times 10^4$ K and $n_e = 5.4 \times 10^5$ cm^{-3}. The radial velocity profiles for the electron density reconstructed with both diagnostics (4.24) are in very good agreement for $|v_{rad}| < 1000$ km s^{-1}, for higher velocity the noise on the line profiles is

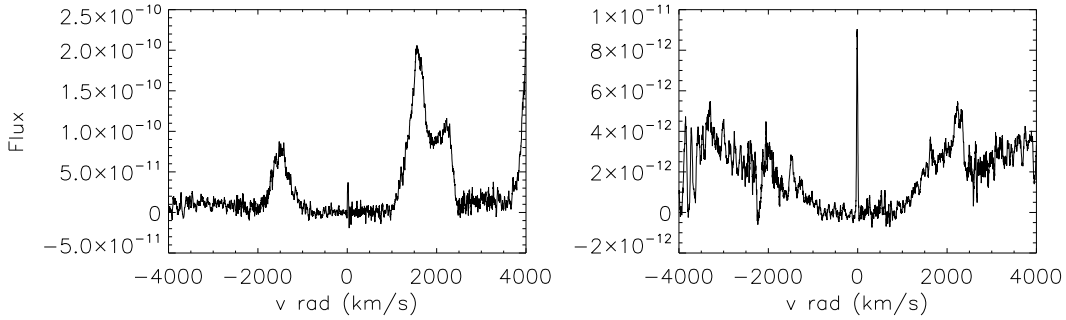

(a) Lyα 1216Å (with O V] 1218Å contamination at +2000 km s^{-1})

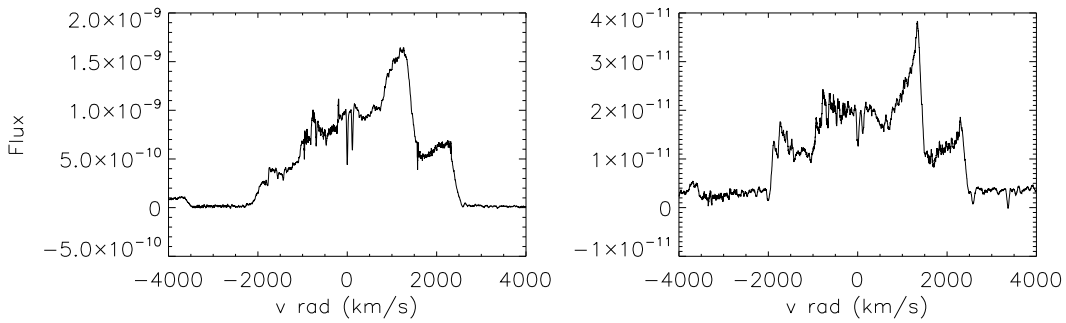

(b) N V 1240Å doublet

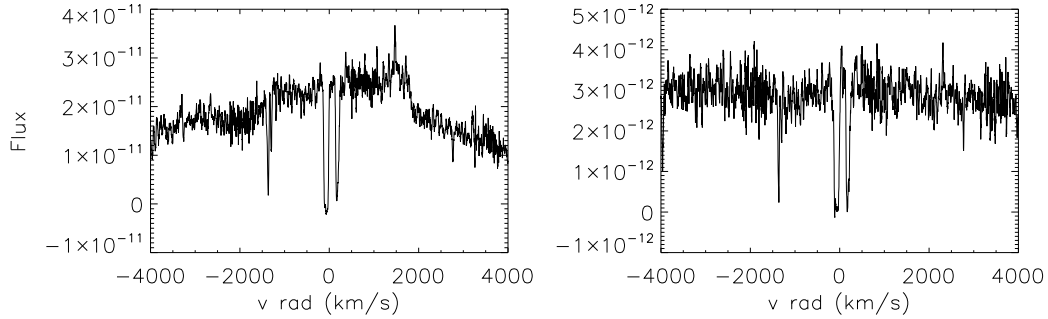

(c) C II 1335Å doublet

Figure 4.17: Ultraviolet emission lines observed with HST/STIS during the nebular stage. Left Oct. 2011, day 180; right, March 2012, day 350.

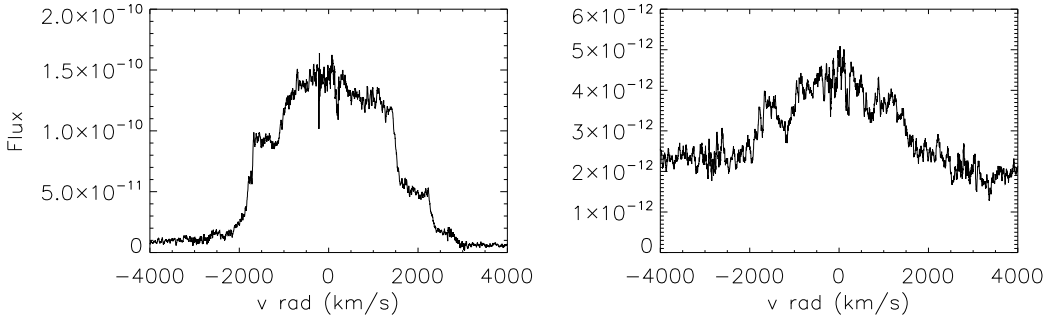

(a) Si IV 1402Å doublet

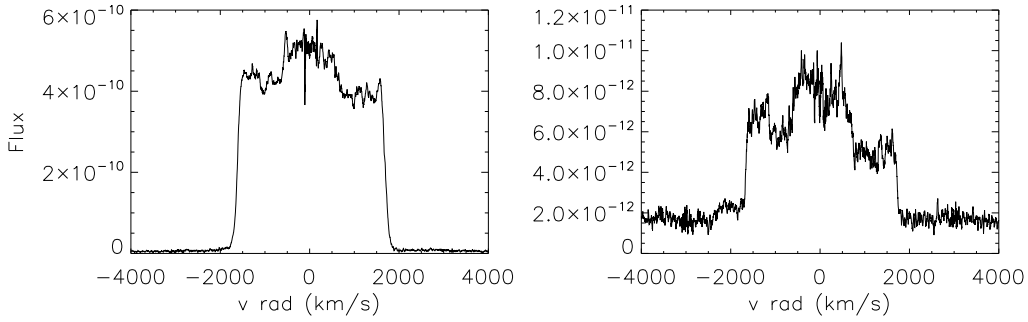

(b) N IV] 1486Å

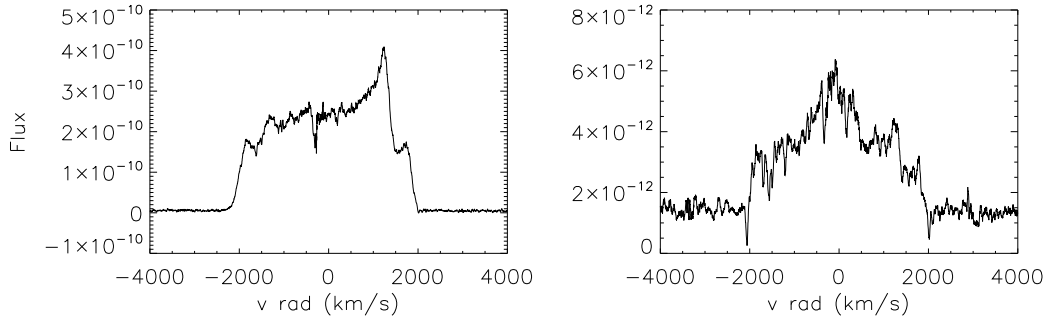

(c) C IV 1550Å doublet

Figure 4.18: Continued from fig. 4.17.

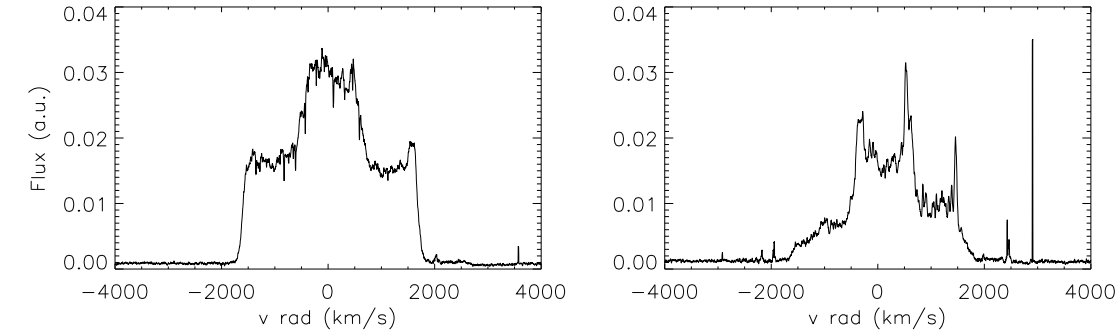

(a) Hα 6562Å

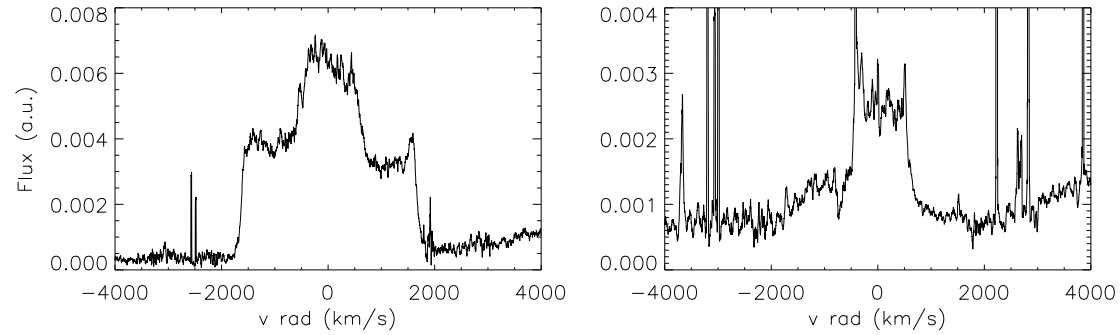

(b) Hβ 4861Å

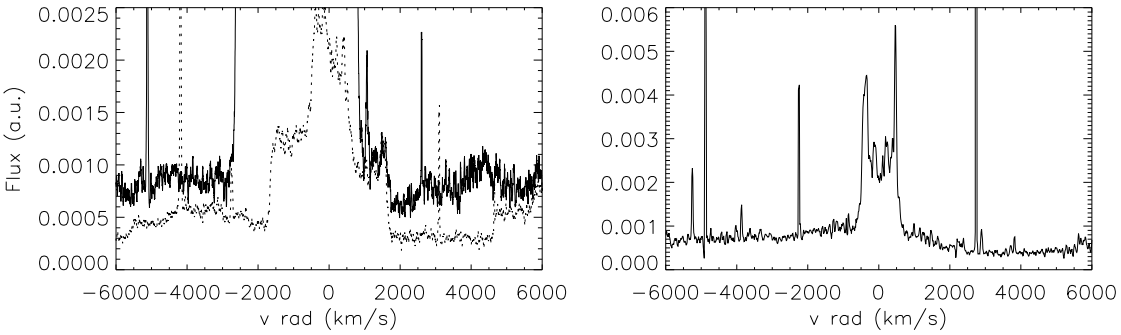

(c) [N II] 6583Å (for day 180, the [N II] 5755Å (dots) profile is superimposed for clarity)

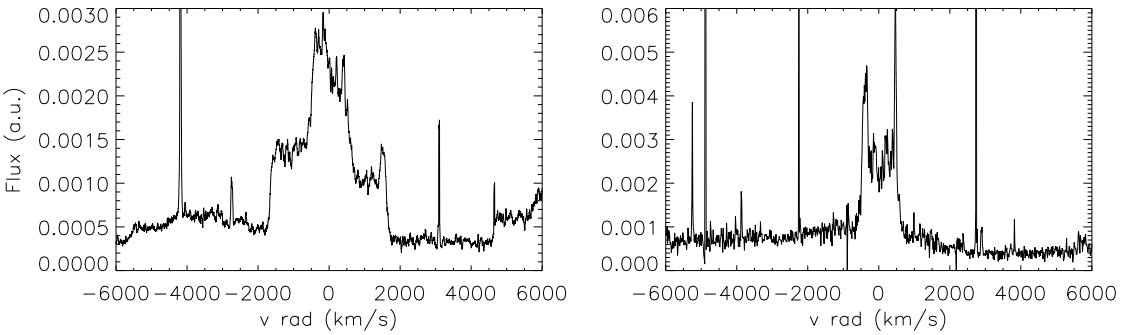

(d) [N II] 5755Å

Figure 4.19: Optical emission lines observed with NOT/FIES during the nebular stage. Left Oct. 2011, day 180; right, March 2012, day 350.

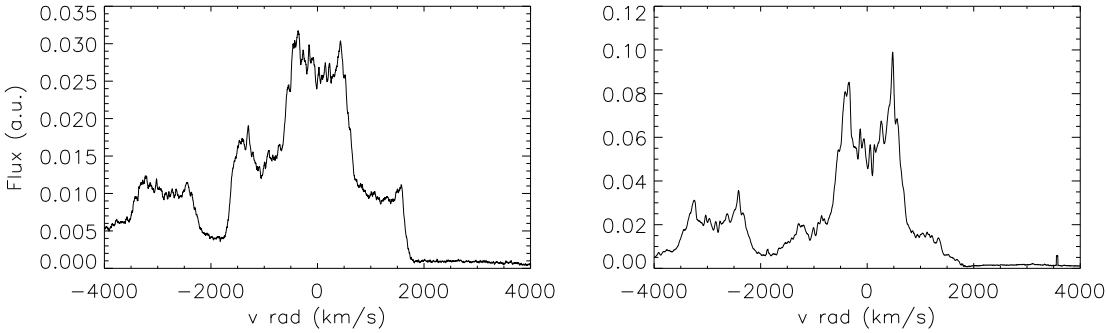

(a) [O III] 5007Å

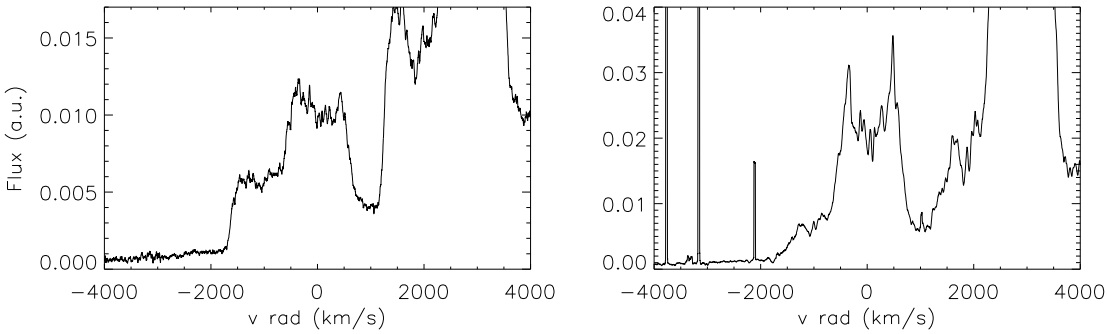

(b) [O III] 4959Å

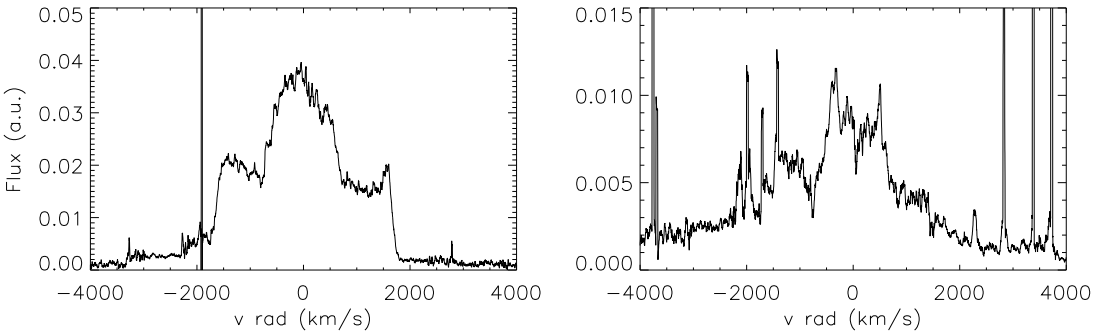

(c) [O III] 4363 Å

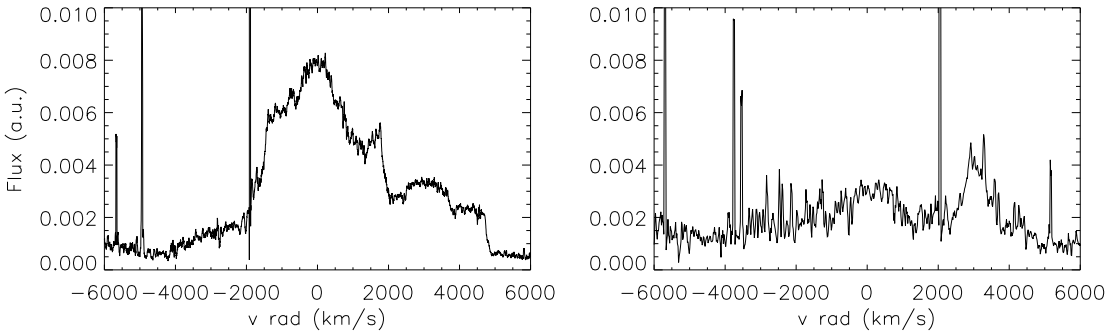

(d) N III 4638Å

Figure 4.20: Continued from fig. 4.19

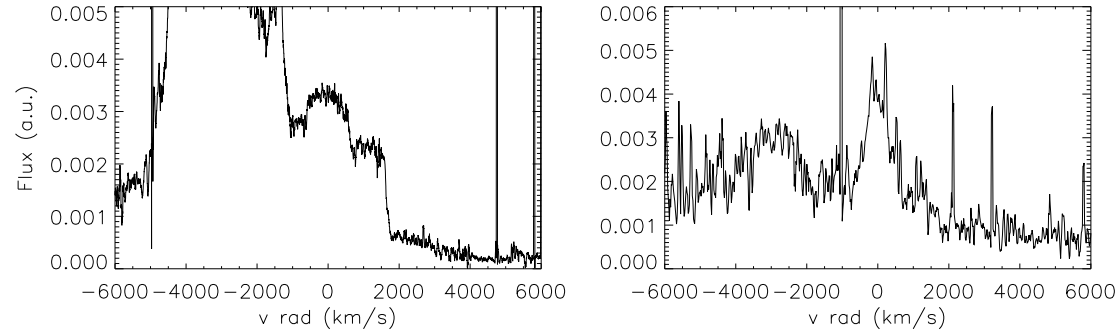

(a) He II 4686Å

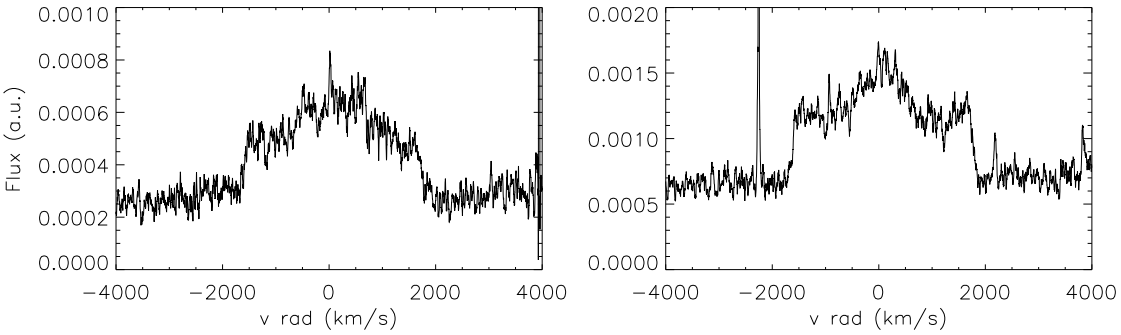

(b) [Ca V] 6086Å

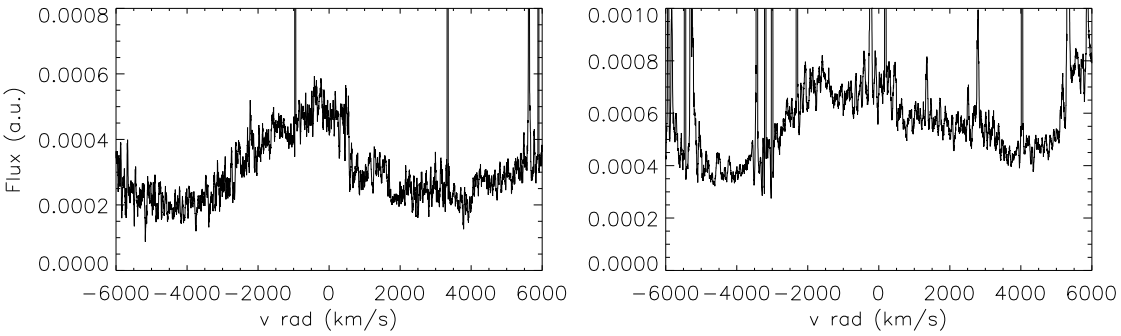

(c) [Ca V] 5309Å

Figure 4.21: Continued from fig. 4.19. [Ca V] identifications is not certain.

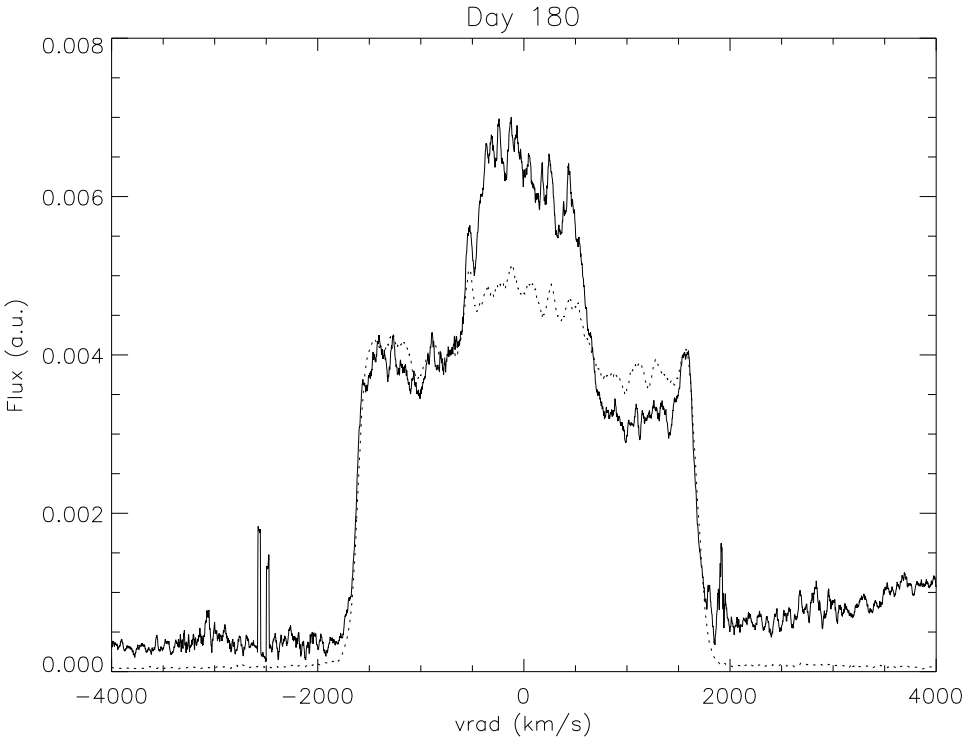

(a) Hβ (solid) N IV] 1486Å (dots)

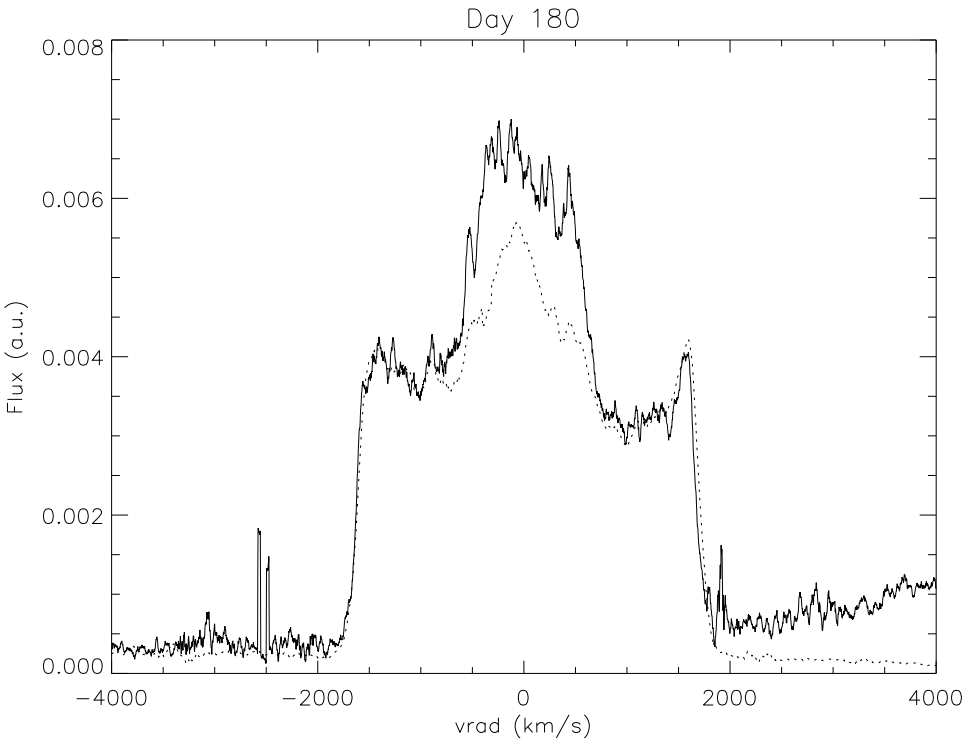

(b) Hβ (solid) C III 1909Å (dots)

Figure 4.22: Comparisons between emission lines observed on day 180. Flux are rescaled.

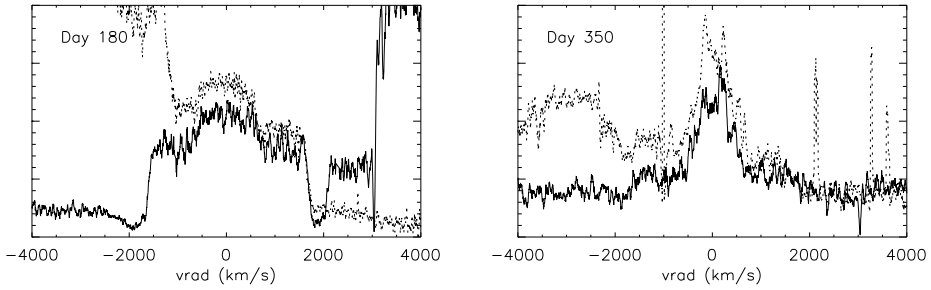

Figure 4.23: Comparison between He II 1640Å (solid line) and He II 4686Å (dots) for the nebular phase spectra, Oct. 2011 (day 180) and March 2012 (day 350). The fluxes have been rescaled. The He II 4686Å suffers the blending with N III 4640Å on the red wing. (Shore et al., 2013a)

problematic.

Thanks to the absolute calibration of day 180 spectrum with the G430L STIS observation, we can measure confidently the $H\beta$ integrated flux, and apply the usual extinction correction. Using the Hβ flux diagnostics (assuming an emitting sphere of hydrogen with a radius R and uniform electron density and temperature, details in the appendix) we can determine a reasonable value on the filling factor f of the emitting volume. To measure the luminosity of the Hβ line, in Shore et al. (2013a) we adopted 3.5 kpc as distance to T Pyx: using the recent measurement by Sokoloski et al. (2013) of d=4.8 kpc, we find a luminosity $L(H\beta) = 2.2 \times 10^{35}$ erg s^{-1}. For an optically thin medium (*Case B* recombination) with $T_e = 10^4$, we determine $n_e^2 V \approx f \cdot 2.4 \times 10^{47}$ cm^{-3}, with V being the volume of the emitting sphere. For day 180, the radius of the sphere is $v_{max} \cdot \Delta t \approx 6 \times 10^{15}$ cm, and assuming $n_e = 3 \times 10^7$ cm^{-3}, it gives an estimate of $f \approx 0.06$, a value which is only double with respect to the published in Shore et al. (2013a). The important result is the very low value of f, suggesting a very fragmented environment.

4.3.4 Bipolar ejecta

Since the first spectroscopic observations of the nebular emission lines, it was commonly recognized the non-sphericity of the expanding ejecta. Payne-Gaposchkin (1957) shows the different emission profiles obtained from various configurations of shells and rings in the ejecta. Hutchings (1972) modeled the ejecta from HR Del using polar cones and rings, with synthetic line profiles that appeared similar to the observed ones.

Before novae, many other objects were observed with remarkable "axisymmetric polar flows": for example, the Homunculus Nebula surrounding the Luminous Blue Variable (LBV) η Carinae, or the planetary nebula (PN) Hubble 5 (4.26). However, we must be very careful about the detailed physical mechanisms leading the formation of this structures: for example, for PNe and nebulosities around massive stars , winds are responsible for creating such structures, taking thousand or million years, while for novae we know that the remnant originated during a very short event.

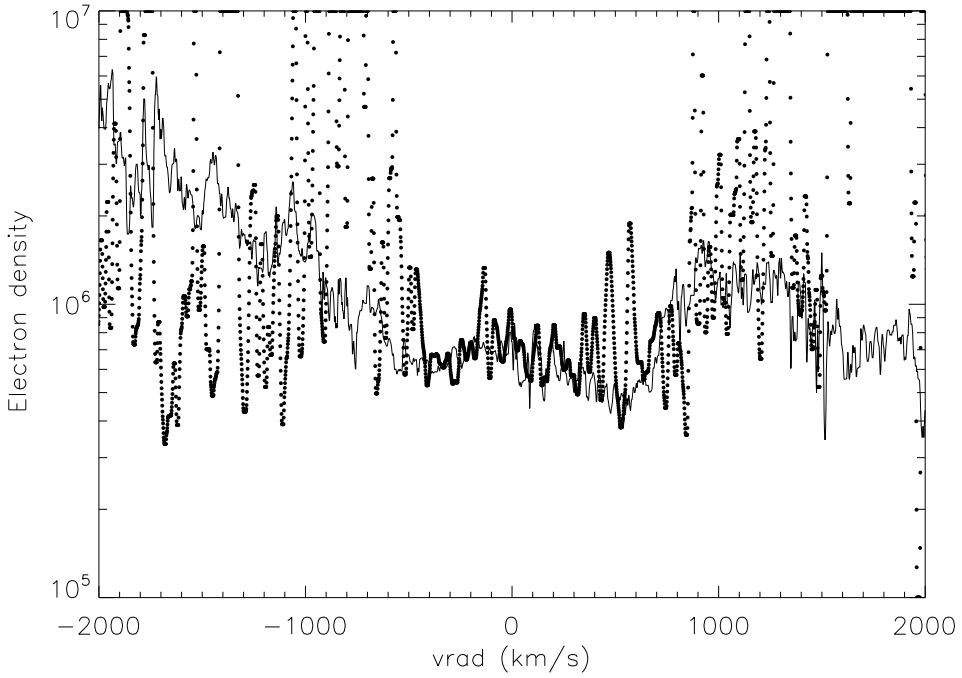

Figure 4.24: Comparison of [N II] (dotted) and [O III] (solid) electron densities from day 350 NOT spectrum. The wings beyond $|v_{rad}|$ = 1000 km s^{-1} are comparatively weaker in [N II] than [O III], hence the much higher noise. (Shore et al., 2013a)

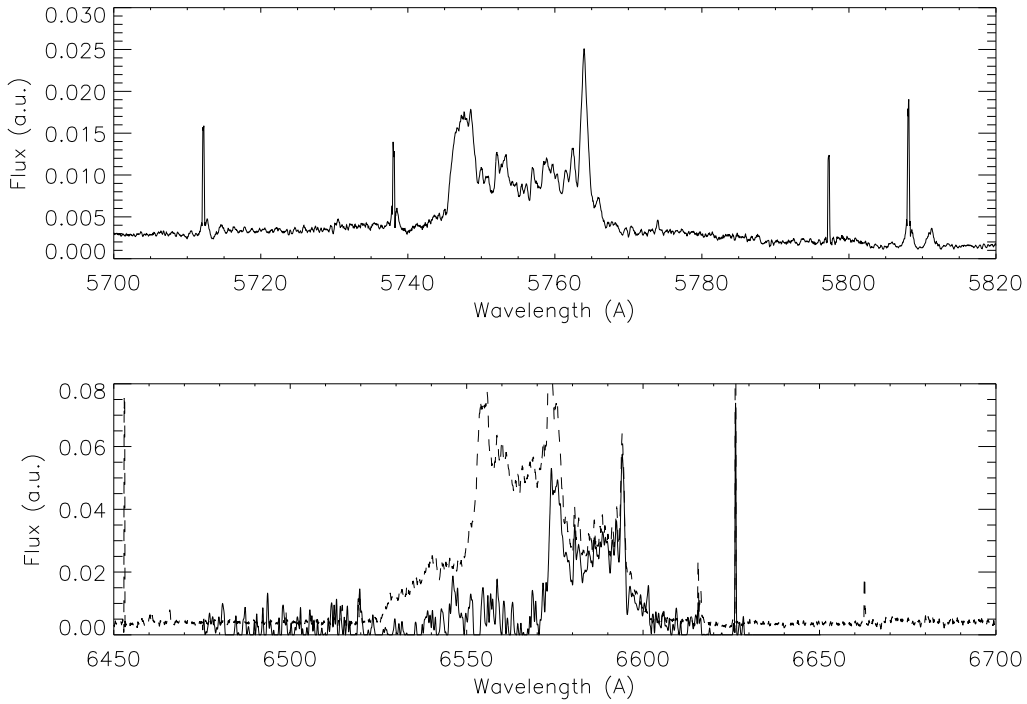

Figure 4.25: Top panel shows [N II] 5755Å on day 350. At the same epoch, the bottom panel shows the reconstructed [N II] 6583Å profile before (dashed) and after (solid) the decomposition of Hα, using Hβ as modeling profile. (Shore et al., 2013a)

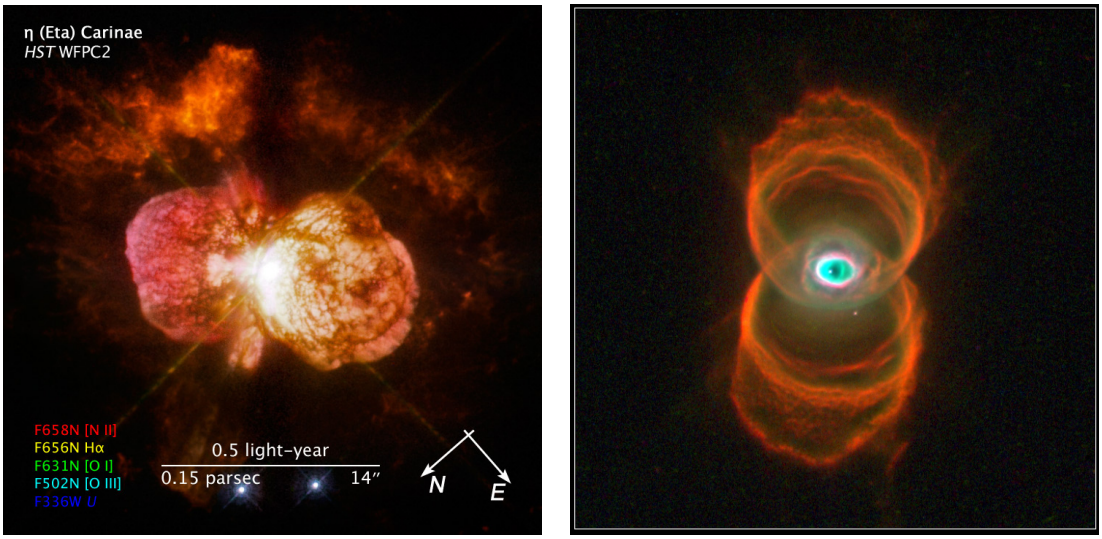

(a) The Homunculus Nebula surronding the LBV star η Car (HST/WFPC2 multifilter composite).

(b) Planetary nebula MyCn 18, best known as the Hourglass Nebula (HST/WFPC2 multifilter composite).

Figure 4.26: Bipolar nebulae.

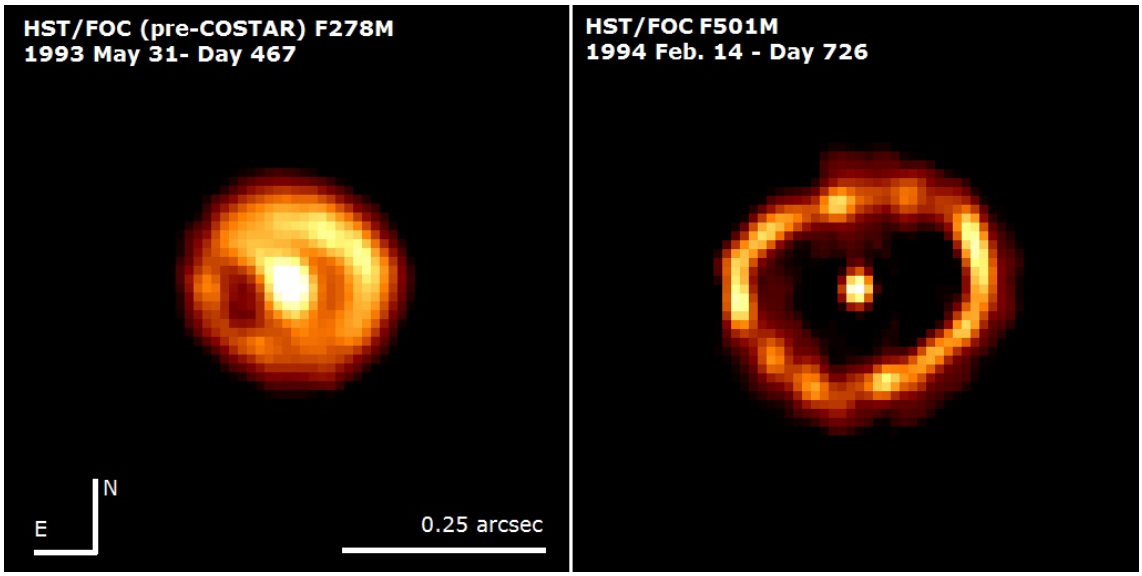

Figure 4.27: Images from HST/FOC of the resolved ejecta of V1974 Cyg 1992. The left image, captured 467 days after the outburst, was obtained before the COSTAR upgrade; the F278M is center on $\lambda = 2800$ with a FWHM=300Å the emission comes primarily from Mg II 2800Å. The right image was captured 726 days after the outburst; the filter F501M is centered on $\lambda = 5010$ with a narrow bandwidth, FWHM=74Å, hence the emission is almost entirely [O III] 4959 and 5007Å (Paresce et al., 1995).

The hypothesis of bipolar flow was confirmed once old novae remnants were resolved (O'Brien & Bode, 2008). Almost any observations, mainly conducted in optical, IR and radio, of novae remnants show non-spherical ejecta, whether they are composed by ellipsoidal shell, polar blobs (elegantly and correctly described as "hour-glass" flow) and/or expanding equatorial rings has been debated for decades. A universal feature is the fragmentation of the ejecta: the expanding gas, if sufficiently resolved, shows up in dozens or hundreds of small substructures (see fig. 4.1), each presenting its own ionization state and density, but generally freely expanding with an average geometry imposed during the first stage of the ejection. V1974 Cyg, an ONe nova discussed in chapter 6, showed remarkably well defined bipolar lobes evolving from a compact to a rarefied shell (fig. 4.27).

The imaging capabilities of HST tremendously improved the knowledge on the fine structures in known remnant. T Pyxidis remnant imaged with HST/WFPC2 appeared heavily fragmented but expanding in radial symmetry. This severely contrasts the early IR interferometric observations by Chesneau et al. (2011) who modeled the expanding ejecta with a bipolar flow, inclined 15^o to the line of sight, an inclination value suggested also by Uthas et al. (2010).

We developed a Monte Carlo procedure to model the line profiles during the nebular stage. The polar ejection are modeled as partially filled cones. Geometrical free parameters determine the opening angle of the bipolar flow ($\theta_1 \geq 0^o$ for the inner angle, $\theta_2 \leq 90^o$ for the outer angle, with respect to the equatorial plane), the inner radius ($\Delta R/R_{max}$), where R_{max} is defined by the maximum velocity of the ejecta v_{max}, the inclination i to the line of sight (see fig. 4.28). The spherical symmetry can be altered with the oblateness parameter a. The ejecta are simulated as N points: for each point, its coordinates are generated randomly and the radial velocity is assigned as a linear function of the radial position r_i, i.e. $v_i = v_{max} r_i / R_{max}$ (but any radial velocity field can be imposed). To simulate the emission from the bipolar cones, emissivity is assigned only to the points inside the region delimited by the chosen angles and the inner radius. The emissivity depends on a power law of the electron density, which in a ballistic ejection of constant mass $n_e \propto r^{-3}$. For a recombination line, then the emissivity goes like the square of the electron density, hence the points emissivities go like $j_i = (r_i/R_{max})^{-6}$. A similar procedure has been already applied for other previous works (Shore at al., 1993, 2003), but at the time the ejecta were modeled with a spherical shell embedding one or more equatorial rings, while in our analysis it was a simple bipolar flow.

It is important to clarify that this model was not meant as a fitting procedure for the line profiles but only as a consistent check on geometrical degrees of freedoms that are relevant for the appearance of the lines. In figures 4.29, 4.30, and 4.31, several geometries are displayed, each figure showing four simulations differing for only one parameter.

The velocity v_{max} for the model was determined from the maximum velocity of the P Cyg profiles of Balmer lines in the optically thick stage, showing absorption up to $\sim$4000 km s^{-1}. The FWZI and FWHM of the modeled profiles depends almost uniquely the inner radius parameter, $\Delta R/R$. From a comparison with Balmer and helium lines, we

constrained $0.4 \leq \Delta R/R \leq 0.5$, independently of the inclination or the exponent in the intensity power law. However, the structure of the profile peak, or multiple peaks, has a mixed dependence on the opening angle of a polar ejection, the inner polar angle, and the inclination. Comparing, for the same epoch, the Balmer, [N II], and [O III] lines, they all showed similar profiles: it appears that there is no particular difference between lines formed by radiative excitation (e.g. the forbidden lines) and those from recombination (Balmer, He II).

Important indications about the geometry come from the comparisons between the two epochs: as already noted, the high velocity "shoulders" decreased in intensity, with the core to wing ratio increasing (fig. 4.32). The He II 1640, 4686Å lines showed much more reduced emission on the shoulders of the line in day 350 than the forbidden lines. This can be reproduced by assuming either a smaller inner fractional radius and/or changing the radial dependence of the intensity power law to mimic different ionizations without a change in the overall geometry of the ejecta. The He^+ region we find is more extensive in the ejecta, signaled by the narrower line profile, but the cone parameters are rather similar. The UV resonance intercombination lines all displayed the same profiles so we consider the match obtained here to be generic of that line forming portion of the ejecta. A peculiar anomaly comes from the N V 1240Å and C IV 1550Å doublets, for which was impossible to obtain a reasonable model.

From the modeling of the lines we found several constraints: inclinations as low as 20^o require an oblate symmetry; the profiles cannot be reproduced with narrow opening angles, $\theta_1 > 20^o$, $60^o < \theta_2 \geq 90^o$, because in this range the polar ejecta become resolved velocity. From this modeling we cannot retrieve any information about the filling factor, because the fragmented structure of the ejecta is a natural consequence of numerical noise in the simulation. Moreover, any velocity law analogous to that from radiatively driven outflows from massive stars is ruled out by the model profiles for all inclinations.

With the geometrical modeling constraints and the estimates on electron density and filling factor, we can now estimate the mass of the ejecta. If $M_{ej} = m_H f n_e(t) V(t)$, m_H the hydrogen mass and $V(t)$ the volume, using the information from day 350 analysis, we find an ejected mass $M_{ej} \approx 4 \pm 1 \times 10^{-6} M_\odot$, a value much smaller than $3 \times 10^{-5} M_\odot$ derived by Schaefer et al. (2010), but in agreement with the other RNe.

4.3.5 Late spectrum

The late time (>1 year) HST/STIS observational program dedicated to understand the quiescent state properties of T Pyx, started on December 2012, has been very important to understand the physical development of the ejecta during the late phase with unprecedented high spectral resolution. At this stage, the ejecta were transparent and no X-ray emissions come from the WD.

On day 617, the spectrum (5th panel in fig. 4.6), observed only with the short wavelength E140M grating, was characterized by a smooth continuum and several line features: the broad damped interstellar Ly α and the other ISM absorption lines, residual emissions from C IV 1550Å and He II 1640Å, and several absorption features on the blue

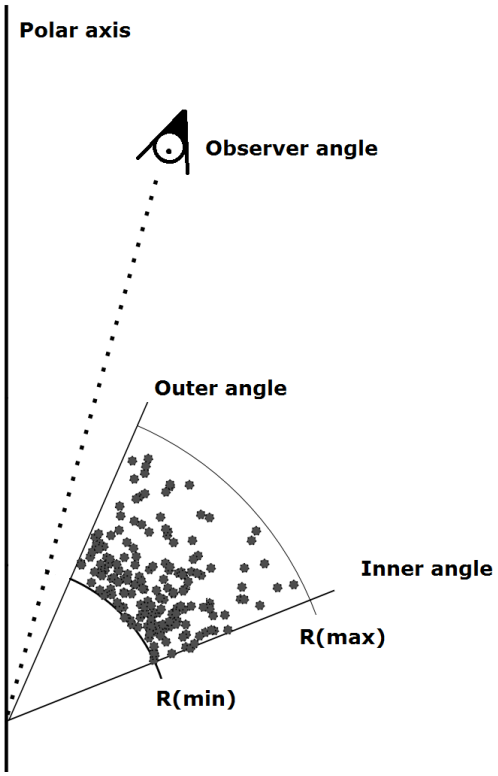

Figure 4.28: Monte Carlo model schematic diagram. This is a 2D section, the full 3D structure is built with a 2π rotation around the polar axis. The dots, which positions is completely random within the volume, have a radial velocity.

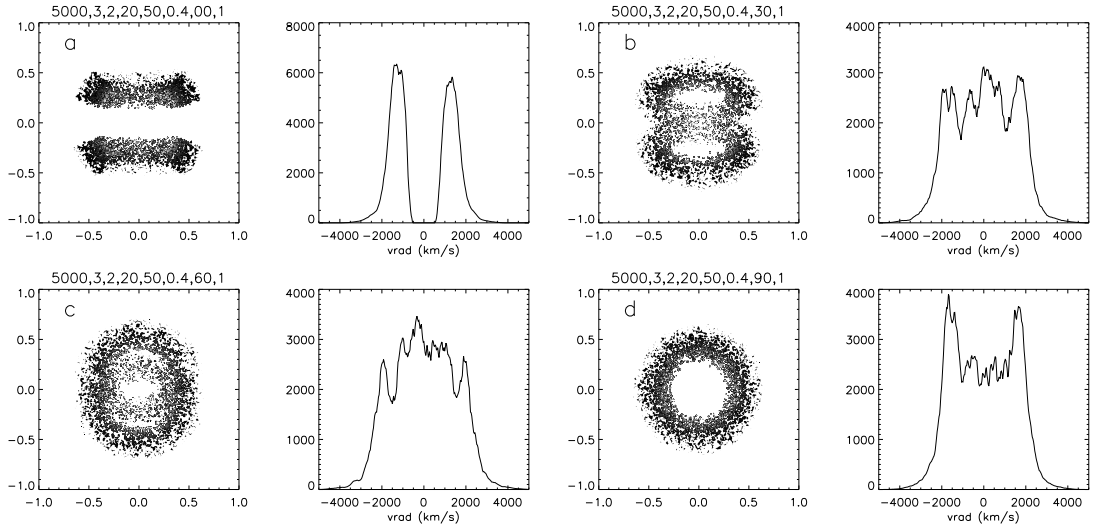

Figure 4.29: Models generated with fixed v_{max} = 5000 km s^{-1}, θ_1=20^o, θ_2=50^o, $\Delta R/R$=0.4, varying the inclination of the system, with values from *a* to *d* being 0, 30, 60 and 90 degrees.

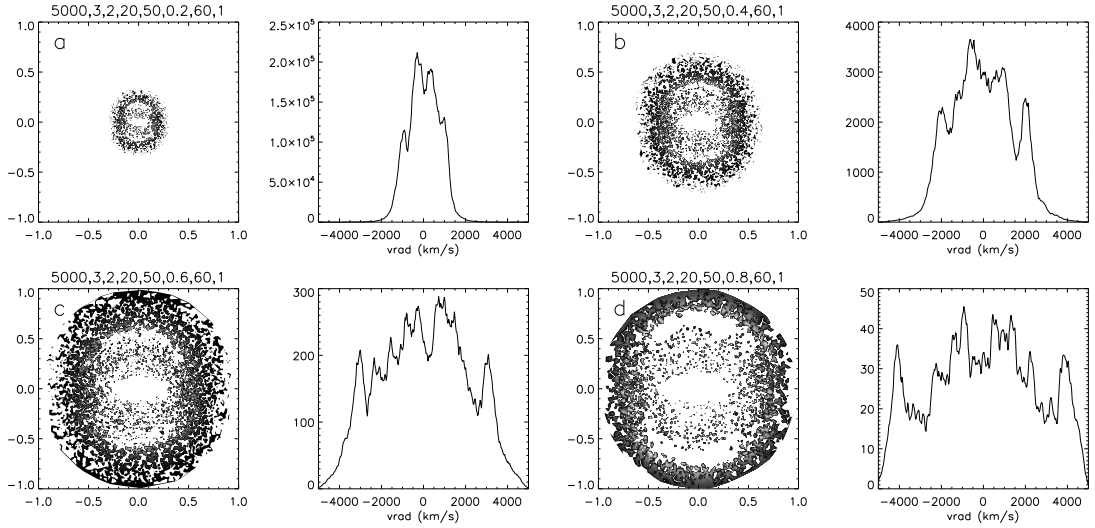

Figure 4.30: Models generated with fixed v_{max} = 5000 km s^{-1}, θ_1=20^o, θ_2=50^o, i=60^o, varying the parameter $\Delta R/R$, with values from *a* to *d* being 0.2, 0.4, 0.6 and 0.8.

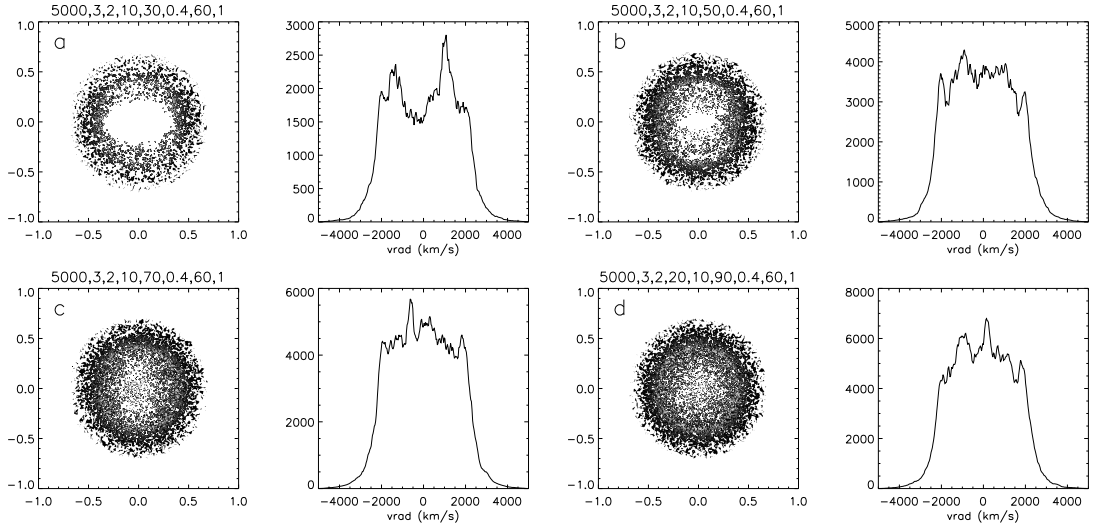

Figure 4.31: Models generated with fixed v_{max} = 5000 km s^{-1}, θ_1=10^o, $\Delta R/R$=0.4, i=60^o, varying the parameter θ_2, with values from *a* to *d* being 30, 50, 70, and 90 degrees.

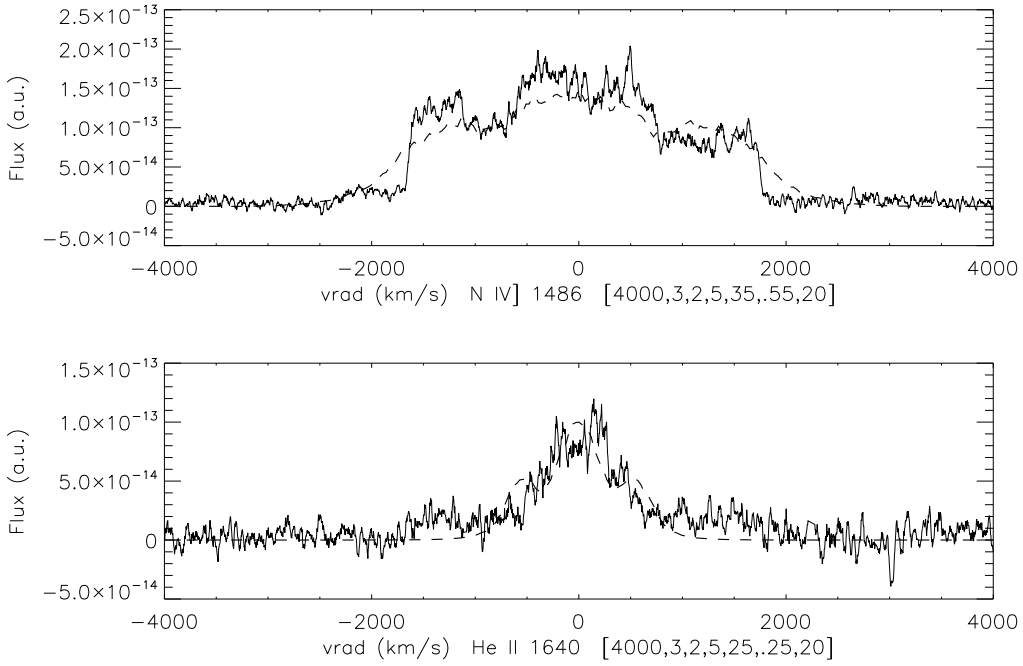

Figure 4.32: The line profiles (solid) of N IV] 1486Å (top) and He II 1640Å (bottom) from March 2012 (day 350) spectra compared with the models (dashes). The N IV] model parameters are v_{max} = 4000 km s^{-1}, θ_1=5^o, θ_2=35^o, $\Delta R/R$=0.55, i=20^o, while for the He II line the parameters are v_{max} = 4000 km s^{-1}, θ_1=5^o, θ_2=25^o, $\Delta R/R$=0.25, i=20^o. (Shore et al., 2013a)

side of N V 1240Å and C IV 1550Å doublets. On day 834 (6th panel in fig. 4.6), the spectrum appeared almost identical, with residual line emissions from the afore-mentioned species being reduced.

The continuum flux at 1400Å on day 834 is 3×10^{-14} erg s^{-1} cm^{-2} Å^{-1}, which is in agreement with the observation on 1996 May 6 with IUE (SWP #57055, low resolution), where the continuum level was 2.5×10^{-14} erg s^{-1} cm^{-2} Å^{-1}: this suggests that the system has returned to quiescence state.

For day 617 spectrum, from the velocity profiles of the N V and C IV doublets, we see two distinct broad absorption features, at -1700 and -1300 km s^{-1}, for each component of both the doublets transitions (fig. 4.36). The width of the features is about 200 km s^{-1}. For a ballistic velocity law, this corresponds to a thickness of $\Delta R/R(t) \sim 0.15$. These simple absorption structure is extremely different from those observed in the early stage of the outburst, where many more narrow components were observed. However, in the early stage, the ejecta absorb against an extended source, while in the late phase the line of sight toward the WD is a pencil beam, thus tracing only two separated clouds/filaments: these structures were present from the initial phase of the expansion, since their velocities agree with the Balmer lines absorptions features during the optically thick phase.

On day 834, we still observed blue-shifted absorptions but the structure slightly changed. A third absorption component appeared at -1500 km s^{-1} for the N V lines; the broad feature at -1700 km s^{-1} had separated into two weaker and narrower components

a -1735 and -1650 km s−1. The C IV absorptions are still present but much weaker. The development of this features shows how the ionization structure of the ejecta is still evolving, with the inner portions still weakly recombining and the outer portions ionizing. It is fundamental to notice that the velocity of the features remained constant through all the epochs, an evidence supported by the striking correspondence of the July 2011 blueshifted features from low ionization metals with the C IV / N V -1300 km s^{-1} absorption.

4.3.6 The ionization structure through C, N and O lines

The resonance doublets of N V 1240Å and C IV 1550Å on day 180 and 350 showed peculiar emission profiles (the development of the lines through all the observed epochs is showed in figures 4.33 and 4.34). In both epochs, the profiles showed a marked emission at approximately +1500 km s^{-1}, this peak being higher when the ionization stage was higher (X-ray peak). The blueshifted portion of the profile was always weaker than the redward side: this suggests that the ejecta were still marginally optically thick. However, while the emission originates from the expanding volume, the absorption was caused by material on the line of sight towards the WD. A velocity check on the absorbing portion of the profiles reveals that the emission on the red side of the line and the absorption on the blue side of the line are displaced by the same velocity, i.e. approximately 1500 km s^{-1}. A possible explanation for these peaks, and relative absorption, may be specific density enhancements at certain radii.

Another clue about the ionization state of the ejecta on day 180 comes from the comparison between the O V 1371Å and He II 1640Å (fig. 4.35): from the differences between the profiles, with O V being flat with respect to He II 1640Å we see that the fast, rarefied material had a higher ionization state with respect to the inner regions of the ejecta, where recombination was active. This is typical of the *freeze-out* conditions, with slow moving, inner, denser region recombining and outer regions recombination being hindered by the expansion rate.

The appearance on day 617 and 834 of narrow blueshifted absorption features against the continuum may seem odd, especially when compared to the earlier spectra absorption component. However, the optical depth during the early phases was very high and pseudo-photosphere was still large, so that P Cyg absorption originated against an extended source. On day 617 and later, long after the X-ray turn off and with completely transparent ejecta, the line of sight towards the central WD was a pencil beam, tracing only the gas on the line of sight. So we observed the negative velocity absorption features: these fragments/filaments were consistently present since the initial stages of the outburst, with their velocities being consistent with the narrow features observed during the optically thick phase of the ejecta.

The changes on day 834 supports these conclusions. The weakening of the C IV absorption and the appearance of a third absorption component for N V, with velocities being constant for the other features, indicates an increase in the ionization of the outer regions while recombination still active in the inner regions.

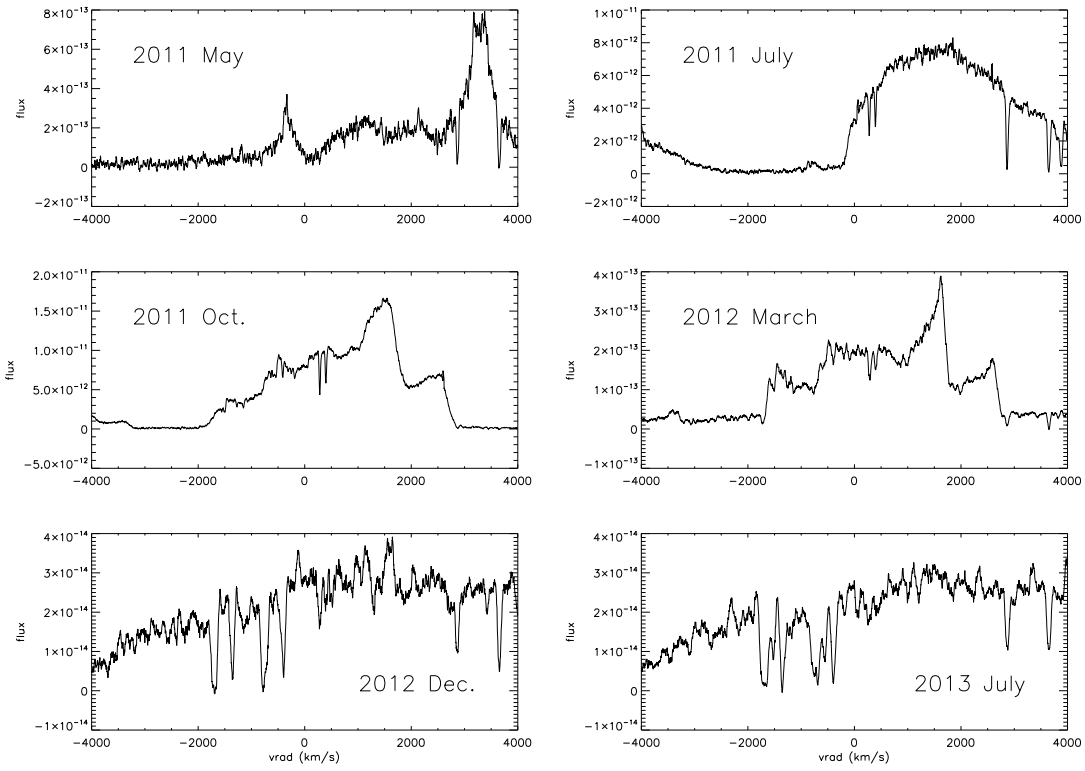

Figure 4.33: The N V 1240Å doublet through all the epochs.

A comprehensive look through all the epochs, with special attention for day 105 spectrum, reveals the ionization structure of the ejecta. The narrow (FWZI∼100 km s^{-1}) absorptions displayed by O I, Si II etc at -1300 km s^{-1} were ∼3 times narrower that the Na^o features during the early stages, but the velocities are remarkably similar, within 30%. Always on day 105, we observed the same velocity range covered by the fragmented P Cyg profile by Si IV 1400Å, which displayed two broad features, FWZI∼ 500 km s^{-1}, roughly centered on -1300 and -2100 km s^{-1}. Finally, with the late spectra, we observe the absorption feature at -1400 km s^{-1}, covering the a slightly larger velocity range with respect to the narrow features on day 105, and the feature at -1700 km s^{-1}. The higher velocity absorptions were seen only on the highest ionized species, weighted by the abundance of the tracing species. For clarity, in fig. 4.37, the velocity structure of the different species observed through all the epochs is showed.

Recalling the C IV and N V profiles, the coincidence of the recombination emission and absorption on the two sides of the lines, hence on the receding and incoming region of the ejecta, cannot be mere chance. The absorption structures observed cover a large volume, thus it's improbable that they are simple knots. Their development follows precisely the ionization evolution of the ejecta. A crucial role in this picture (very important for any future high resolution follow up) is the orientation of the ejecta: if T Pyx was oriented differently, we would have observed completely different spectra.

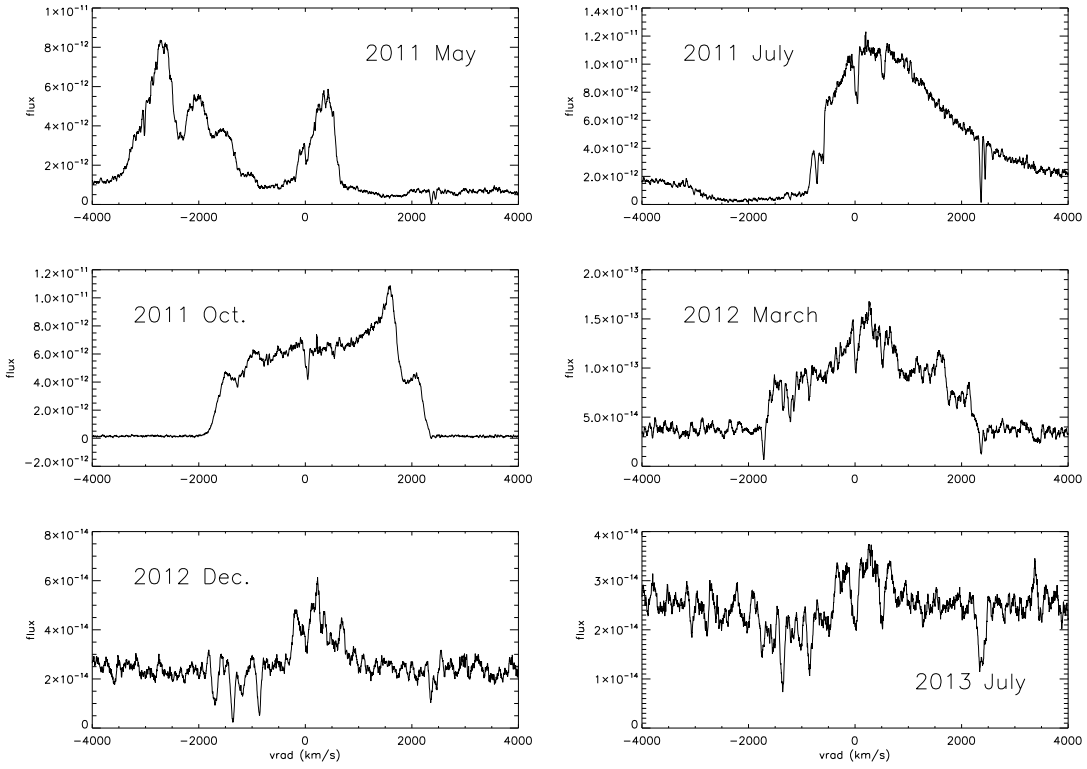

Figure 4.34: The C IV 1550Å doublet through all the epochs.

4.4 Interstellar medium towards T Pyx

The study of the interstellar medium on the line of sight towards T Pyx has been possible thanks to the high luminosity of the source. However, novae may not seem ideal for this investigation: the source is non-stationary, with both continuum and line emission fluxes varying through the different epochs. In fact, many lines were visible only when strong emission fluxes were present on those specific wavelengths. However, the same spectroscopic variability helped in identifying the narrow absorption features at high negative velocity already discussed. Along with the UV and optical data, we used the 21cm neutral hydrogen emission spectrum from the GASS survey (Kalberla et al., 2010) to compare the velocity profile of the absorption interstellar lines.

The observed lines are displayed in figures 4.38, 4.39,and 4.40. Several species displayed not saturated, optically thin profiles: Al II, C I, Cl I, Cr II, Fe II, Mg I/II, Mn II, N I, Ni II, Si II, and Zn II. These transitions all show similar profiles, with a mean radial velocity in agreement with the 21cm emission core. Spectral resolution was sufficiently high to resolve, for few cases, e.g. Cl I 1347.24Å and the Mg II 1240Å doublet, two distinct velocity components at v_{LSR} +11 and +22 km s^{-1}. Only on Day 23, the molecular transition ^{12}CO A-X(3,0) at 1447.335Å was observed, with a velocity profile in agreement with the other optically thin ISM lines.

Several optically thick saturated lines from low ionization transitions were present: C II, Mg I/II, O I, S II, Si II. The profiles were completely opaque in the core and wings extended from -30 to +100 km s^{-1}, a similar velocity interval to the 21cm spectrum.

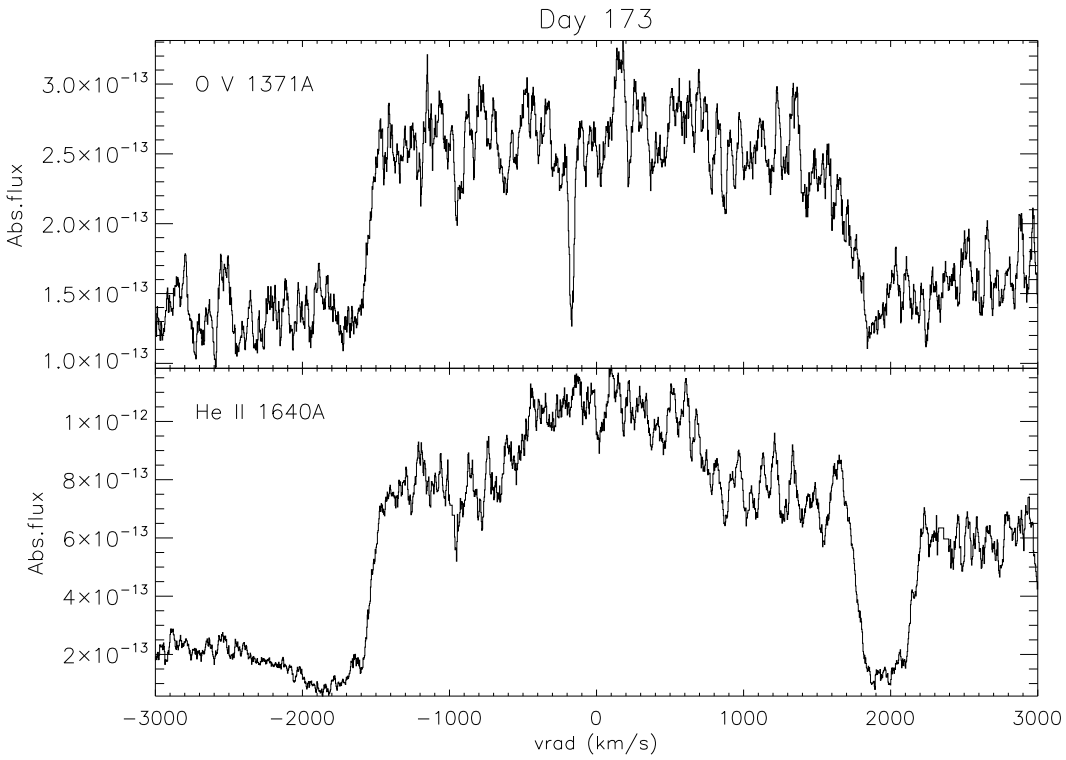

Figure 4.35: O V 1371Å and He II 1640Å on day 173. The difference in the profiles is due to higher ionization conditions of the outer regions of the ejecta, i.e. high velocities, combined with augmented recombination rate in the inner, denser regions. The narrow absorption line in the O V profile is the interstellar Ni II 1370Å line.

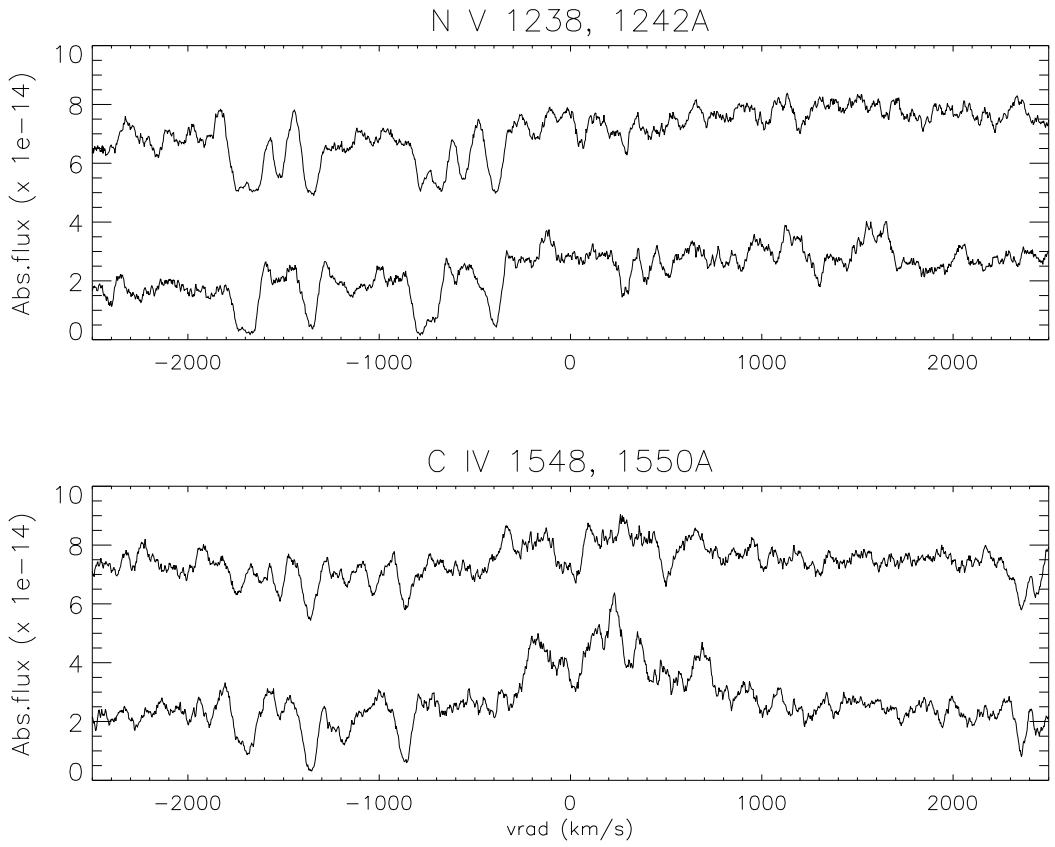

Figure 4.36: Comparison of N V 1238, 1242Å and C IV 1548, 1550Å lines (the rest wavelength is fixed on the red component of the doublets). In each panel, day 834 is on top, shifted by 5×10^{-14} erg s^{-1} cm^{-2} $Å^{-1}$ for clarity. For the N V lines, it must be noted in the later spectrum the fragmentation of the -1700 km s^{-1} component into two blended features and the strengthening of the -1500 km s^{-1} features; for the C IV, the -1700 km s^{-1} weakened and the -1500 km s^{-1} features strengthened too.

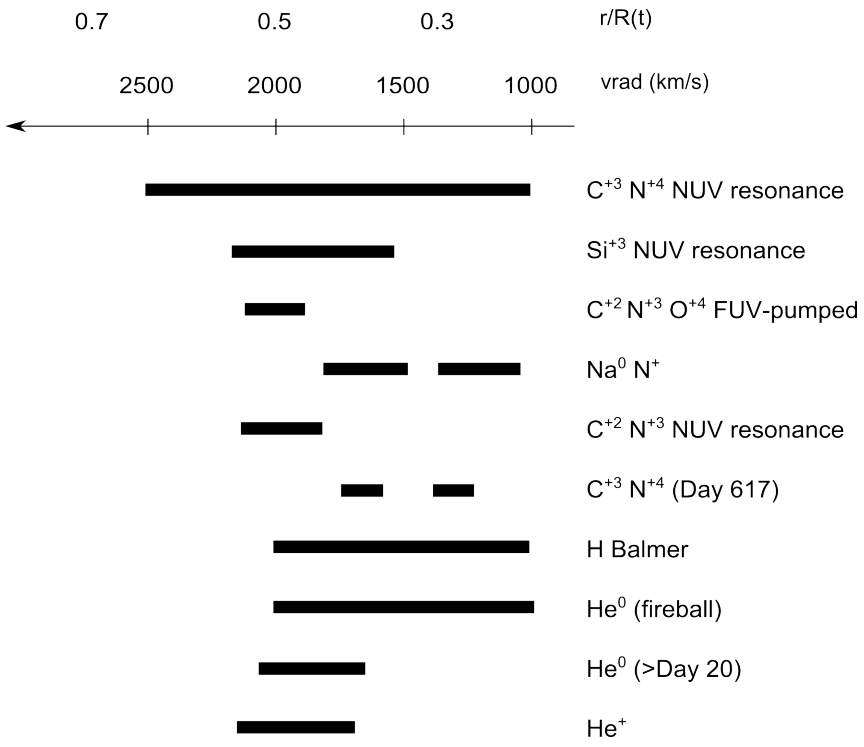

Figure 4.37: Schematic diagram showing the velocity and relative radial position of the absorption features from P Cyg profiles or narrow blueshifted components observed during the fireball, transition and the late development phases. NUV: near ultraviolet; FUV: far ultraviolet.

Highly ionized species were also present, Al III, C IV, Si III/IV, displaying broad, non completely saturated profiles extending from -10 to +80 km s^{-1}.

For each line observed, where no severe blend was present, the equivalent width was measured and reported in tables 4.4, 4.5.

4.4.1 Curve of growth

A curve of growth model was built to estimate the column densities of low ionization species (more about this technique in the appendix). This approximation assumes that the absorption spectrum observed is caused by one single cloud on the line of sight characterized by a Maxwellian velocity distribution for the atoms: this contrasts with the observational evidence of at least two velocity components (two clouds) on the line of sight. This technique also reduces the information about the velocity profile of each line into one single parameter, b, the width of the Gaussian. Jenkins (1986) suggested that a single Gaussian component model for the curve of growth does not dramatically change the results obtained with respect to other techniques, e.g. detailed fitting of each profile or multi-component curves of growth, with the difference being less or comparable to the observational error for poorly resolved lines.

The uncertainties on the equivalent widths and derived column densities were calculated following the method explained in Sembach & Savage (1992).

The curve of growth with the best-fit model ($b = 18.8 \pm 0.2$ km s^{-1}, with a $\chi^2/dof = 1.28$) is displayed in figure 4.42. For the transitions from highly ionized species, which

Species	Obs	$\lambda^a()$	f^b	EW (mÅ)	Note
Si II	3	1190.42	0.277	350 ± 30	(s)
Si II	3	1193.29	0.575	410 ± 50	(s)
N I	3	1199.55	0.132	380 ± 50	(s)
N I	3	1200.22	0.0869	330 ± 50	(s)
N I	3	1220.71	0.0432	300 ± 50	(s)
Si III	3	1206.51	1.67	500 ± 60	(s)
Mg II	2	1239.93	6.21e-4	68 ± 8	–
Mg II	2	1240.40	3.51e-4	55 ± 7	–
S II	1	1250.58	6.02e-3	205 ± 18	–
S II	1	1253.81	0.0121	235 ± 25	(s)
S II	1	1259.52	0.0182	320 ± 30	(s)
Si II	2	1260.42	1.22	–	(s); bl. C I 1260.74Å
C I	2	1276.48	3.69e-3	49 ± 8	–
C I	2	1277.25	–	–	bl. C I 1277.53Å
C I	2	1280.135	0.0261	105 ± 13	–
P II	2	1301.87	0.038	$\gtrsim 70 \pm 10$	–
O I	2	1302.17	0.052	440 ± 20	(s)
Si II	2	1304.37	0.0928	363 ± 16	(s)
Ni II (c)	2	1317.22	0.0571	56 ± 13	–
C I	3	1328.834	0.058	190 ± 20	–
C I	3	1329.1	–	–	unresolved triplet
C I	3	1329.6	–	–	unresolved doublet
C II	1	1334.53	0.129	508 ± 15	(s)
C II	1	1335.71	0.115	318 ± 19	(s)
Cl I	2	1347.24	0.114	53 ± 5	–
Ni II (c)	2	1370.13	0.0588	70 ± 9	–
Si IV	2	1402.77	0.255	38 ± 12	–
^{12}CO(d)	1	1447.335	0.0361	43 ± 7	–
Ni II (c)	1	1454.84	0.026	22 ± 5	
Si II	1	1526.72	0.133	468 ± 45	(s)
C IV	2	1548.20	0.190	159 ± 20	–
C IV	2	1550.77	0.0952	67 ± 10	–
C I	2	1560.31	0.0716	208 ± 15	–
C I	2	1560.7	–	–	unresolved doublet
Fe II	1	1608.45	0.0591	320 ± 20	–

Table 4.4: Ultraviolet ISM lines: a) Laboratory vacuum wavelengths. b) All f-values from Morton (2003), unless otherwise indicated. c) f-values from Jenkins et al. (2006). d) f-value from Welty & Fowler (1992). (s) saturated profile.

Species	Obs	$\lambda^a()$	f^b	EW (mÅ)	Note
C I	2	1656.267	0.0598	97 ± 15	–
C I	2	1656.928	0.143	–	(s); bl. C I 1657.01Å
C I	2	1657.379	0.0357	59 ± 15	–
C I	2	1657.907	0.0476	70 ± 15	–
Al II	2	1670.79	1.83	443 ± 28	(s)
Ni II (c)	2	1741.55	0.0427	70 ± 12	–
Ni II (c)	2	1751.91	0.028	57 ± 10	–
Si II	1	1808.01	2.49e-3	240 ± 30	–
Al III	1	1854.72	0.557	194 ± 17	–
Al III	1	1862.79	0.277	111 ± 9	–
Zn II	1	2026.14	0.515	180 ± 15	–
Mg I	1	2026.48	0.113	$\gtrsim 115 \pm 10$	–
Cr II	1	2056.25	0.105	103 ± 8	–
Cr II	1	2062.23	0.078	72 ± 6	–
Zn II	1	2062.66	0.2529	154 ± 15	–
Cr II	1	2066.16	0.0515	52 ± 5	–
Fe II	1	2249.88	1.82e-3	65 ± 15	–
Fe II	1	2260.78	2.44e-3	122 ± 13	–
Fe II	1	2344.21	0.114	607 ± 24	(s)
Fe II	3	2374.46	0.0359	497 ± 37	–
Fe II	3	2382.76	0.320	717 ± 48	(s)
Mn II	3	2576.88	0.3610	418 ± 35	–
Fe II	3	2586.65	0.0717	597 ± 50	(s)
Mn II	3	2594.51	0.28	406 ± 26	–
Fe II	3	2600.17	0.239	763 ± 53	(s)
Mn II	3	2606.47	0.198	228 ± 32	–
Mg II	1	2796.35	0.608	976 ± 23	(s)
Mg II	1	2803.53	0.303	895 ± 22	(s)
Mg I	1	2852.96	1.800	550 ± 25	(s)

Table 4.5: Continued from tab. 4.4.

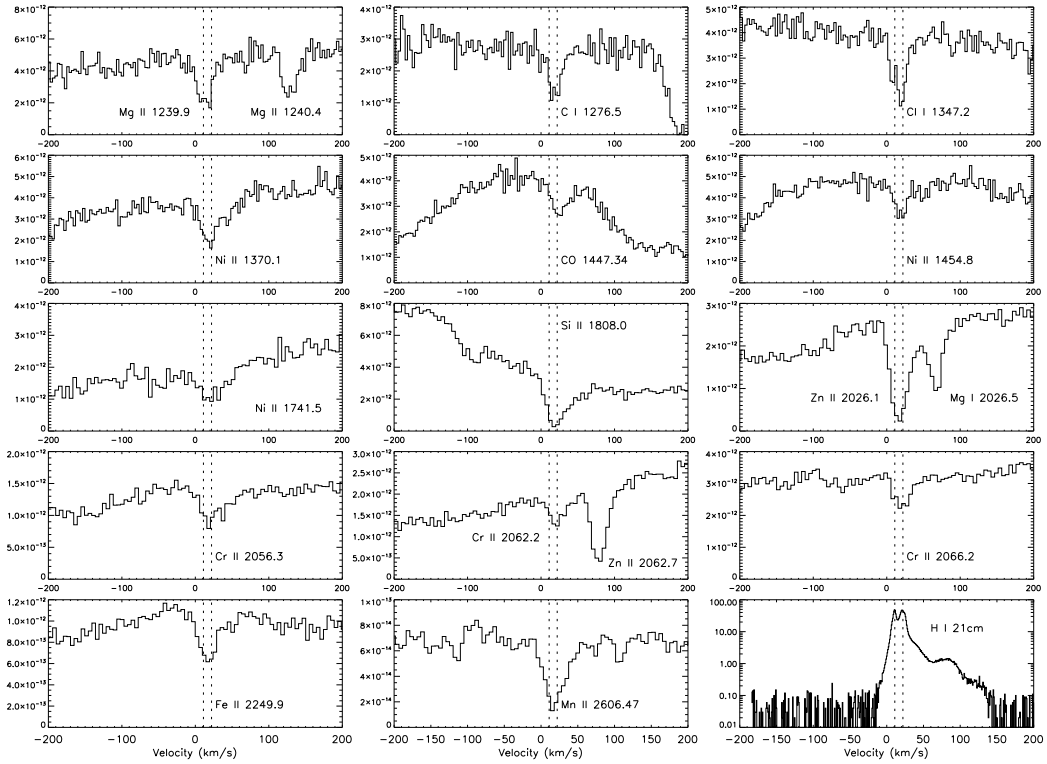

Figure 4.38: UV interstellar lines observed with HST/STIS and 21cm neutral hydrogen spectrum data from the GASS survey in the heliocentric velocity frame. On y-axis: flux ($erg\,s^{-1}\,cm^{-2\,-1}$), and for the 21cm profile log T_b, brightness temperature, (K). Dotted lines mark +11 and +22 km s^{-1} radial velocity. Optically thin lines.

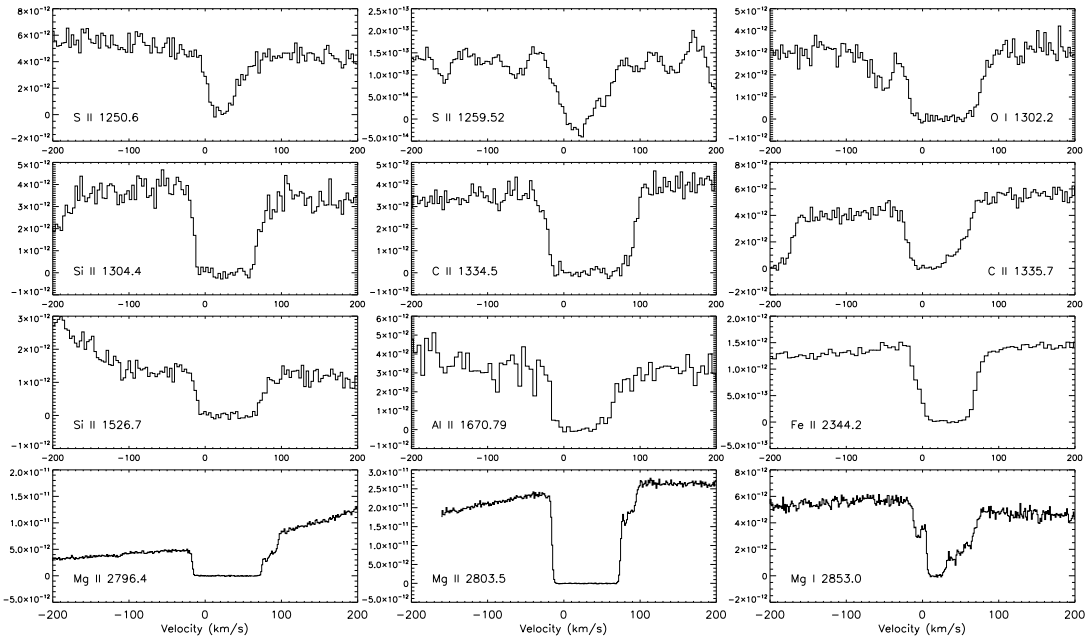

Figure 4.39: As in Fig. 4.38: saturated interstellar lines.

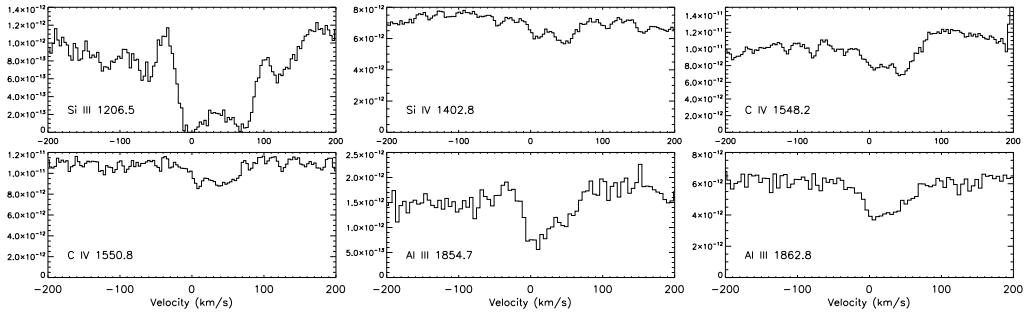

Figure 4.40: As in Fig. 4.38: high ionization species lines.

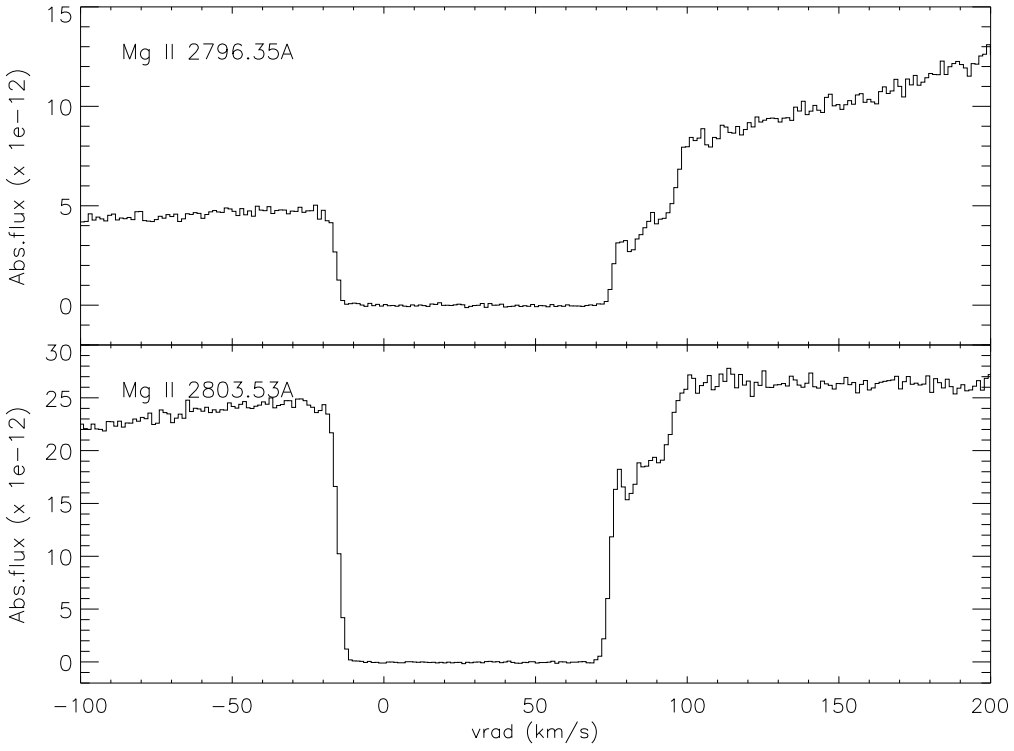

Figure 4.41: Interstellar Mg II 2796 and 2803Å profiles from day 23 HST/STIS spectrum. Note the almost complete saturation of the profile (the residual flux is only background scattered light) and the presence of two unresolved not saturated components at +80 and +90 km s^{-1}.

Species	-1σ	Log N (cm^{-2})	+1σ
H I[a]	21.40	21.48	21.54
Al II		>12.99	
Al III	13.03	13.09	13.14
C I	14.43	14.50	14.57
C II		>14.40	
C IV	13.47	13.56	13.64
Cl I	13.47	13.52	13.57
Cr II	13.42	13.47	13.51
Fe II	15.03	15.21	15.39
Mg I		>13.44	
Mg II	15.86	15.97	16.07
Mn II	13.55	13.64	13.73
N I	15.61	16.10	16.68
Ni II	13.75	13.85	13.94
O I		>14.75	
P II		>14.09	
S II	15.75	15.94	16.17
Si II	15.61	15.98	16.40
Si III		>13.37	
Si IV	12.76	12.93	13.05
Zn II	13.18	13.24	13.29
^{12}CO	13.73	13.81	13.87

Table 4.6: Column densities derived with the curve of growth model displayed in fig. 4.42. a) hydrogen column density as derived in Shore et al. (2013a) b) Column densities estimated with eq.(4.1).

lines may originate in a different environment with respect to the low ionization species, we used the equation (Jenkins 1986)

$$N\,[\mathrm{cm}^{-2}] = \frac{m_e c^2}{\pi e^2 f \lambda^2} W_\lambda = 1.13 \times 10^{17} \frac{W_\lambda\,[\mathrm{m\AA}]}{f \lambda^2\,[\mathrm{\AA}]} \tag{4.1}$$

which is suitable for unsaturated profiles. For the optically thick transitions not included in the curve of growth model (Al II, C II, Mg I, O I, P II, Si III) the same equation was used to give a lower limit on the column density.

The result from the curve of growth suggests that the lowly ionized species absorptions originate in the same environment. However, the presence of highly ionized species, i.e. Al III, C IV, and Si IV, suggests a mixed composition of the ISM on the line of sight. Given the distance to T Pyx, it is reasonable that, on the line of sight, we observe neutral and lowly ionized gas typical of the galactic disk, and warm, highly ionized gas associated with the galactic halo.

The high resolution NOT optical spectra also showed CH molecular lines, CH 4300Å and CH^+ 4232Å, and many DIBs (reported in Shore et al., 2012).

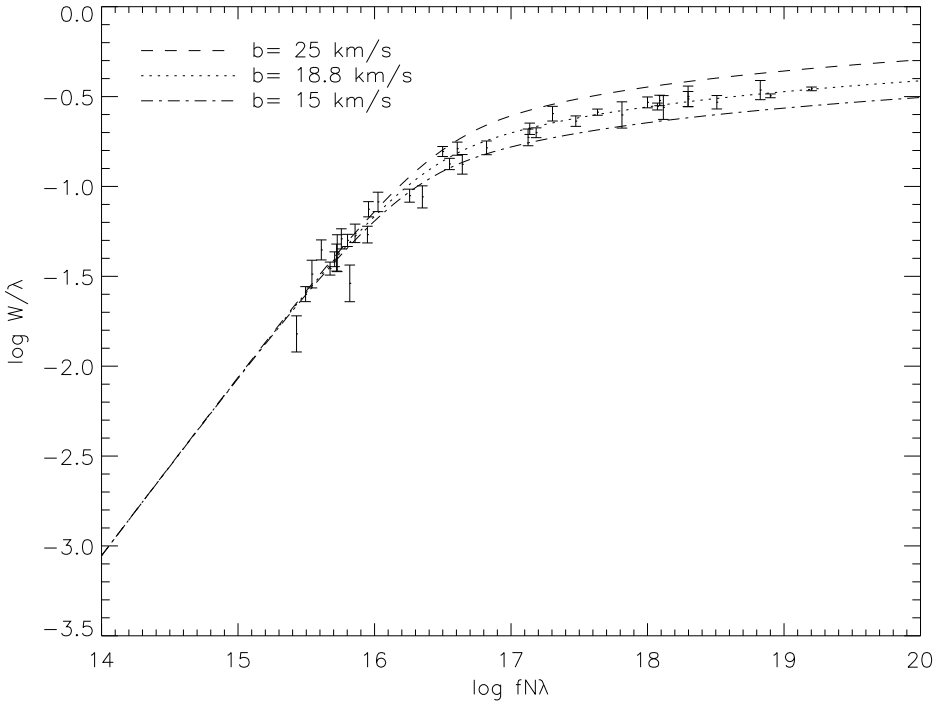

Figure 4.42: Curve of growth for low ionization species. For each species, the lines are shifted horizontally by an amount equal to the column density derived and vertically by the wavelength value in order to display all the lines on the same theoretical curve of growth.

4.4.2 Physical properties

A reasonable estimate of the distance to T Pyx is very important for understanding the nova event. Several attempts have been conducted in the past, all suggesting a distance between 3 and 4 kpc (Selvelli et al., 2008; Schaefer et al., 2010). Recently, Sokoloski et al. (2013), who observed the light echos of the outburst emission reflected by past ejected material, reported a distance of 4.8 $\pm$ 0.5 kpc. Our estimate is based upon the rotation curve of the third Galactic quadrant (Brand & Blitz 1993). Thanks to a very high signal-to-noise ratio for Day 23 E230H spectrum, we can see from the velocity profiles of the deeply saturated absorption lines of Mg II 2796Å and 2803Å (fig. 4.41) that the line is completely saturated from -10 to +70 mk s^{-1}, with two blended unsaturated components clearly present at +80 and +90 km s^{-1}. From the rotation curve, this velocity corresponds to a distance of the absorbing cloud of $\sim 5 \pm 1$ kpc. This result, which is not a direct measurement of T Pyx distance but only an indication, is in very good agreement with Sokoloski et al. measurement.

The presence of the molecular lines in both UV and optical spectra, ^{12}CO 1447Å, CH 4300Å and CH^+ 4232Å, is tightly linked to the presence of DIBs (*diffuse interstellar bands*). The identification of the atomic or molecular species responsible for the DIBs is an open question, but it is widely accepted that large molecules are involved (Herbig, 1995). This observation, possible only because of the high signal-to-noise and spectral resolution achieved by NOT/FIES, clearly shows how the ISM is a rather complex mixture of

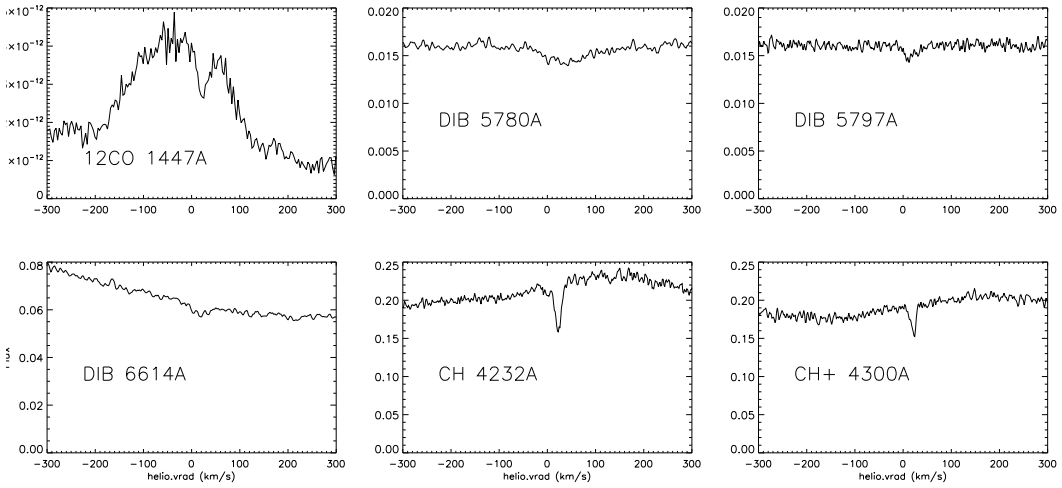

Figure 4.43: Molecular and DIBs interstellar lines on the line of sight towards T Pyx. The profiles, with the exception of the broad 5780Å DIB, cover the same velocity range.

different gas phases.

4.5 T Pyx and all its friends

As a classical CO nova, with high recurrence being probably the outcome of several physical parameters acting together, T Pyxidis spectroscopic evolution is not different from other novae. Although it never had a dust formation event, the general spectral development did not show any new unobserved properties. Only the late phase, thanks to high resolution spectroscopy, revealed for the first time the recombined, still optically thick, ejecta gas on the line of sight years after the outburst. We have found that the WD is massive, close to the Chandrasekhar limit, a property which is usually assigned to RNe, with the additional requirement of high accretion rate. It is important then to discuss other systems, physically similar or not, in light of our latest results.

4.5.1 Close orbit RNe

We do not know many binary systems like T Pyx with such a short orbital period. Only two other RNe, CI Aql and IM Nor, with T_{orb}<1 day, present similarities and differences that deserve full attention. Other systems, like U Sco, have a slightly larger orbital period, T_orb∼1 day, but high recurrence rate, for U Sco is ∼10 years. Symbiotic-like recurrent novae, like RS Oph, are instead characterized by very large orbital period, T_{orb}∼years. And also in this case, RS Oph goes on outburst every ∼20 years. This suggests something about the intrinsic causes leading to high outburst recurrence: the WD mass is very high and, independently (almost) of the orbital separation or environment, massive WDs will erupt more frequently.

The first evolutionary phase in T Pyx outburst presented a very long phase of high optical depth, lasted almost two months: it is easily recognizable, within the light curve,

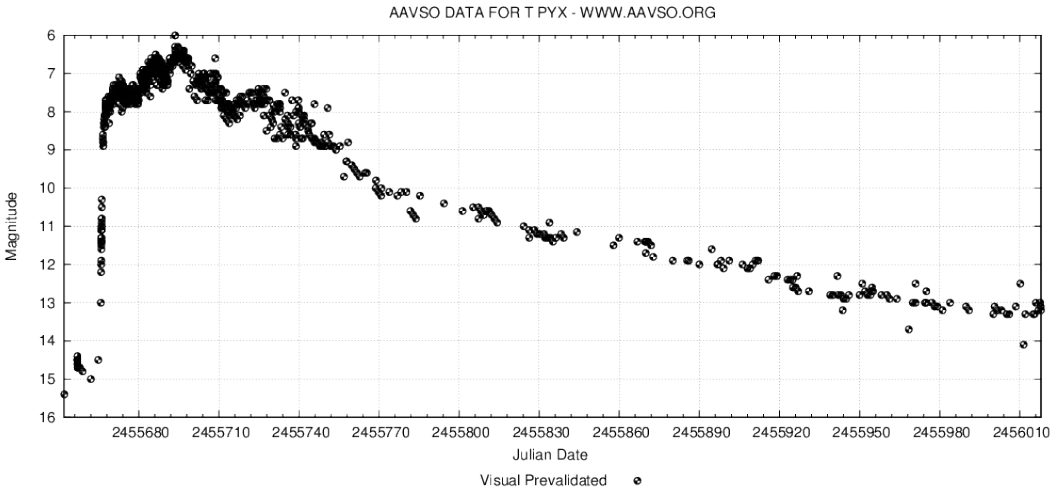

(a) T Pyx 2011 visual light curve.

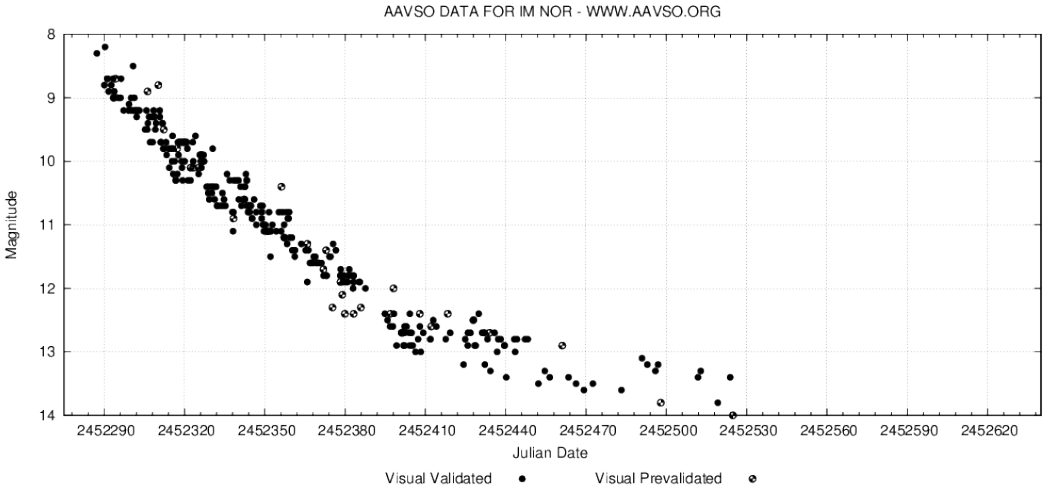

(b) IM Nor 2002 visual light curve.

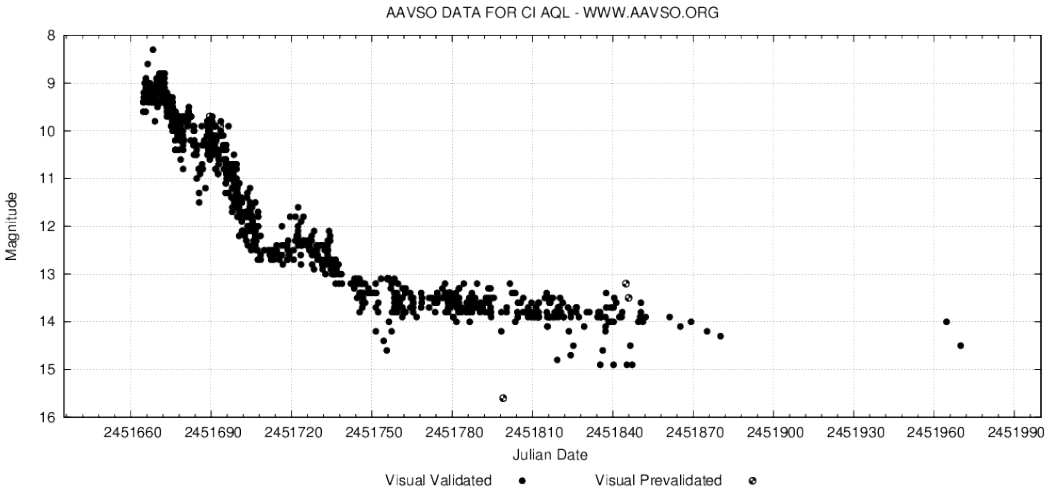

(c) CI Aql 2000 visual light curve.

Figure 4.44: Visual light curves (AAVSO) of T Pyxidis, IM Nor and CI Aql.

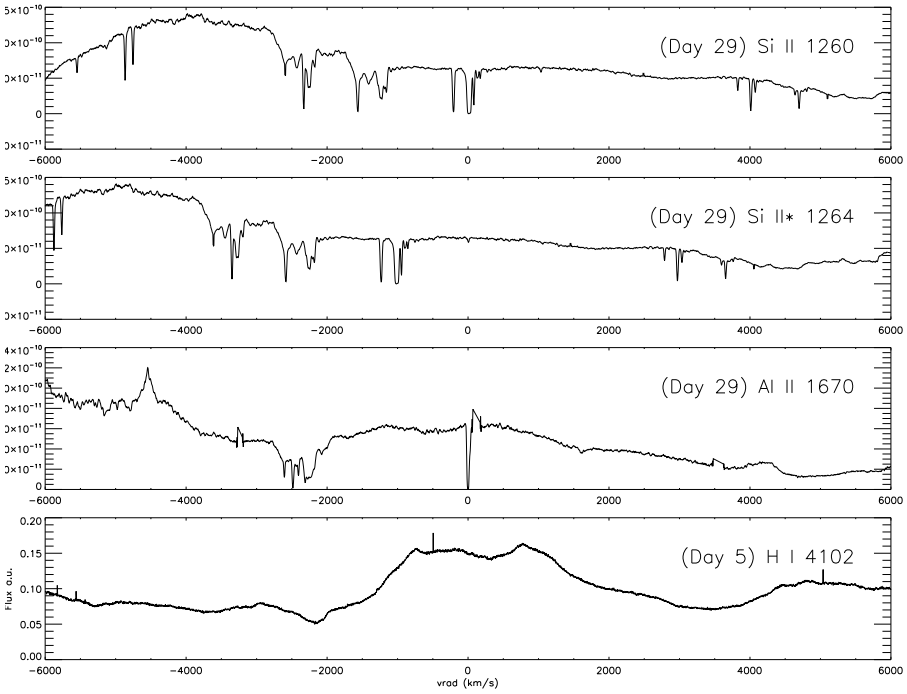

Figure 4.45: V382 Vel 1999 - HST/STIS spectrum on 21st June 1999 (day 29 after visual maximum) showing the high velocity absorption features, from -2600 to -2100 km s^{-1}, for Si II 1260Å and the excited state transition Si II 1264Å. The third panel shows the Hγ P Cyg profile from ESO/FEROS spectrum on 28th May 1999 (day 5), with the absorption covering the same velocity range of the UV Si II lines.

as a prolonged time interval where the visual magnitude was close to maximum. In details, this long phase is characterized by a series of small amplitude rebrightenings with a few days interval. CI Aql, which like T Pyx features a very compact orbital system (P_{orb}∼0.6 h), displayed a similar light curve in its latest 2000 outburst. IM Nor 2002 presented instead smoother light curve (fig. 4.44). All novae, however, presented long t_2 time scales, approximately ∼30 days. These properties don't fit together perfectly: if the systems host a massive WD, the masses of the ejecta should be small, as well as t_2. We have measured for T Pyx $M_{ej} \sim 4 \times 10^{-6} M_{\odot}$, similar values are found for CI Aql ($\sim 3 \times 10^{-6} M_{\odot}$, Iijima, 2012) and IM Nor ($\sim 8 \times 10^{-6} M_{\odot}$, Hachisu et al. 2003). With these values, we see that the relationship proposed by Della Valle et al. (2002) that correlates M_{ej} and t_2, doesn't work, because for $t_2 \sim 30$ days, the mass of the ejecta should be $\sim 10^{-4} M_{\odot}$.

The physical scenario leading to the outburst and its outcome, i.e. the role of the WD and the energetics of the explosion, the mass of the ejecta etc, are still reasonably well understood, several details about the post-outburst development of the system require for further investigation.

4.5.2 Optically thick phase

Several other novae were observed, before T Pyx, with high resolution spectroscopy during the fireball and optically thick phase: Williams et al. (2008) optical analyses with ESO/FEROS, Cassatella et al. (2004b) with UV spectra of V1974 Cyg. They recognized and properly identified the narrow absorption features coming from the absorption side of P Cyg line profiles. However, they proposed a different explanation: the moving features are optically thick parcels of gas originated, before the outburst, from the secondary star which mass is lost during the accretion quiescent period goes towards the WD and outside the system.

The evolution of V382 Vel 1999, an ONe nova that is part of the next chapters discussion, was studied in the UV range by Shore et al. (2003) and optical spectra were discussed by Della Valle et al. (2002) and Williams et al. (2008). However, although the optical DACs were properly identified and reported in Williams et all paper, while not mentioned in Della Valle et al. work, the ultraviolet narrow features, clearly present in HST/STIS spectrum from 21st June 1999 (day +29) were never recognized (fig. 4.45). This observation ties in classical CO novae outbursts with ONe ones: this is not surprising anyway because the physical processes taking place are identical, with the "big" differences in WD mass and composition being relevant only for the TNR physics. As a future work, I plan to recover the old data from nova V382 Vel and reanalyze them in the light of the latest discoveries.

4.5.3 Recurrent novae vs Supernovae Type Ia

Supernovae (SN) are the most violent phenomena ever observed in our galaxy. They are characterized by a an enormous increase in magnitude (historically, they were observed with naked eye for days or weeks), with a total energy release of the order of 10^{51}erg. A specific scenario, known as Type Ia, is currently depicted as the carbon-deflagration and detonation of a CO WD close to the Chandrasekhar limit. The fundamental role of SNe Ia in the history of the galaxy and their use as cosmological standard candles is not discussed here: see Hillebrand & Niemeyer (2000) for a detailed review.

Whether novae represent a preliminary stage towards SN Ia is still an open question. Given the high accretion rate and high WD mass, recurrent novae are considered suitable candidate for further SN Ia events, but the rate of formation of RNe (with the requirement that the WDs grow up to the M_{Ch} limit) is too low to account for the rate of SN Ia.

T Pyx final faith has been extremely debated in the last decades, with pre-2011-outburst studies generally in agreement with the *non* SN Ia final scenario (Selvelli et al., 2010). Another longstanding issue was the prolonged quiescence state T Pyx entered after 1966 outburst, with Selvelli et al. (2008) suggesting a 2025 date for the next eruption (no uncertainty provided), in contrast with Schaefer el al. (2005) suggesting a 2052 ± 3, later corrected with 2225 (Schaefer et al., 2010). After the 2011 outburst, the eventual SN Ia outcome of T Pyx is still debated: Patterson et al. (2013) report the results from a 15 years observational campaign that show an increase in orbital period mainly caused by

mass loss, a strong argument against SN final faith.

Recently, Sahman et al. (2013) suggested, from detailed analysis of CI Aql post-outburst spectra from quiescence state, determined the properties of the system, composed by a 1.00±0.14 $M_\odot$ CO WD and A-type companion 2.32±0.19 $M_\odot$, and proposed that it is evolving towards higher mass accretion rate: the companion is still burning hydrogen in the core but it has just begun to evolve away from the main sequence, filling its Roche lobe. At this stage, mass transfer evolves on thermal-timescales, so that the accreting envelope on WD could grow, eventually up to the Chandrasekhar limit, with their models predicting a SN Ia explosion within ∼10 Myr.

The greatest unknowns for this problem are the WD mass (for which we have suggested a very high value, close to Chandrasekhar limit) and the mass transfer rate, and much is left to understand on how the explosive event changes the CV evolution: for instance, efficient convective mixing during the explosion is well observed, but we still don't know its effects on the long-term WD evolution.

Chapter 5

V959 Monocerotis 2012

Nova Monocerotis 2012 is an ONe nova with a peculiar observational history: it is the first classical nova to be discovered as a γ-ray sources. Its optical/UV properties were studied when the ejecta were already in the nebular stage, but a detailed comparison with past ONe novae has lead to confirm and discover fundamental features of this class.

5.1 High energy γ-ray emission

The *Fermi Gamma-ray Space Telescope* is a space observatory, a grand collaboration between NASA and many European government agencies, to observe the γ-ray sky. INFN Pisa section intensively contributed to the realization of the on board Large Area Telescope (LAT), a pair conversion telescope covering the energy band from 20 MeV to 300 GeV, which surveys the entire sky in approximately three hours, looking for high-energy (> 100 MeV) emission sources. This instrument has revealed new outstanding properties of the initial, unexpected energetic stages of novae outbursts. In fig. 5.2 the three γ-ray light curves for the first novae observed with Fermi-LAT. See Cheung (2013) for a short but complete summary of the discoveries.

On 2010 March 13th, Fermi-LAT detected a bright source, which position was coincident with the symbiotic-like nova V407 Cyg, discovered in outburst in March 10th. Although observed for the first time, this strong γ emission was not extremely surprising for this class of objects: Tatischeff & Hernanz (2007) suggested, for RS Oph, that energetic photons could be generated by pion productions and high energy proton collisions or inverse Compton and bremsstrahlung emission by relativistic electrons, with particles being accelerated in the shock between the nova ejecta and the Red Giant companion atmosphere embedding the white dwarf.

In June 2012, two transients were discovered, with γ emission lasting roughly two weeks. The first transient, started on June 9th, was associated with Nova Sco 2012, a classical nova visually discovered on May 22nd (to date, no detailed spectroscopic analysis has been published about this nova). The second transient, on 15th June and detected for few days, was not associated with any known object in that field of view, in the Monoceros constellation, and ground observations were impossible due to the

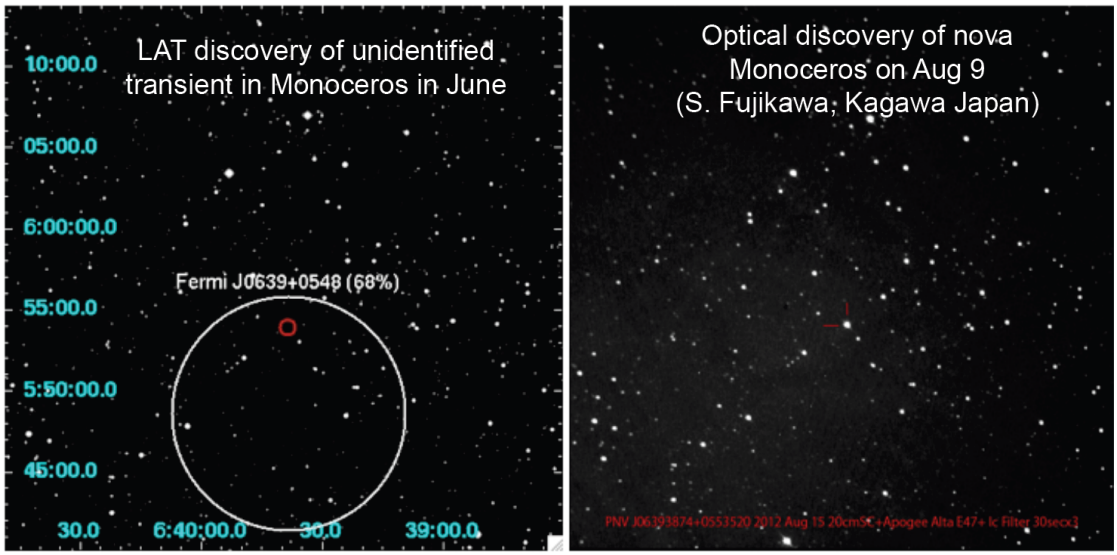

Figure 5.1: Left - plot of the position of the reported possible nova, PNV J06393874+0553520 (red circle); right - optical discovery of Nova Mon 2013 (Cheung, 2013).

Sun position. On August 9th, at 9.4 V-magnitude, possible nova candidate was suggested by S. Fujikawa (CBET #3202). I then personally participated to the observations, data reduction and preliminary analysis of the low resolution spectra obtained at the Haute Provence Observatory on August 14th: it was then possible to associate the γ-ray transient to an ONe nova (fig. 5.1, Cheung et al., 2012; ATel # 4310).

Recently, August 2013, another nova has been observed as a γ-ray source: Nova Del 2013 (CBET #3628), which from preliminary spectroscopic analysis (Shore et al., 2013c) resembles a CO nova, thus definitely demonstrating the very high energy emission from any novae subclass.

The high-energy γ-rays emission from CNe is indeed an unexpected and surprising phenomenon. Since the discovery of strong γ-ray emission from V407 Cyg, the phenomenon was not obscure, but for CNe, which lack dense environments where the shock could propagate and accelerate particles, the same physical processes producing >100 MeV photons must be equally efficient in a much rarefied medium. In Shore et al. (2013b), we proposed internal shocks as leading mechanism. During the optically thick stage, individual filaments and knots may present differential velocities close to the expansion rate of the envelope, $\sim 10^3$ km s^{-1}. The fragmented structure of the ejecta is a universal properties for novae, hinting at common processes taking place during the ejection and to omnipresent high-energy γ-rays. The ONe class is probably a much efficient γ emitter because the energy released in the outburst is greater than CO novae, thus being observable over larger Galactic volume, thanks also to small absorption from the interstellar gas in this energy range.

This description is absolutely preliminary and it needs theoretical and computational effort. Another observational mystery regards the soft-γ rays, related to nova radioactivity, with energy from 511 keV (electron-positron annihilation) to few MeV (unstable

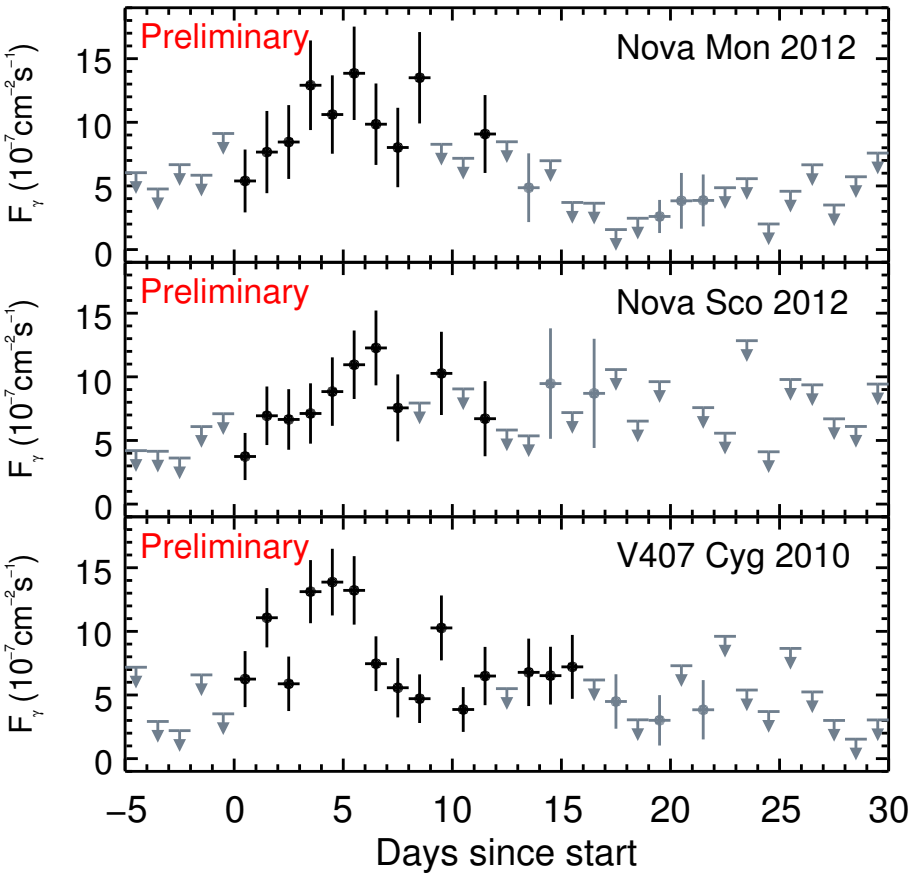

Figure 5.2: Fermi/LAT 1-day binned (energy above 100 MeV) preliminary light curves of the three detected gamma-ray novae (Cheung, 2013). The start dates indicated are from top to bottom, 2012 June 9, 2012 June 15, and 2010 March 10. Black points with error bars indicated detections with 3σ significances, gray points with error bars indicate data with 2-3σ significances are shown in gray, gray upper limits for detections below 2σ. For all novae, HE γ-rays were confidently detected for an extended period, $\sim$10 days. As of the writing of the thesis, Nova Del 2013 Fermi/LAT detection has been continued since Aug. 18 2013 (Hays et al., 2013).

NOT/FIES	Date	JD 2450000+	Day	t_{exp} (sec)
	2012 Aug 16	56155.243	55	300
	2012 Sep. 6	56176.212	76	2000
	2012 Oct. 6	56206.049	106	3000
	2012 Nov. 21	56252.060	152	2765
CHIRON				
	2012 Nov 22	56253.257	153	1800
HST/STIS	Obs.id: grating			
2012 Nov. 20	OC4701010: E140M	56251.896	151	900
	OC4701020: E230M	56251.912	...	310
	OC4701020: E230M	56251.919	...	410

Table 5.1: Journal of V959 Mon 2012 observations.

isotopes decays), which so far have been never observed. The fundamental merit of Fermi-LAT is its high cadence entire sky observational activity and exceptional sensitivity.

5.2 Nebular stage

From the preliminary low resolution spectroscopic observations at the Haute Provence Observatory on August 14th and the first high resolution data on 16th from NOT/FIES, the appearance of the spectra incredibly resembled the late epoch ones from V382 Vel 1999 (Della Valle et al., 2002), one the brightest nova ever observed, member of the ONe subclass. The spectroscopic evolution of V382 Vel is showed in fig. 5.3, and a comparison between the 1999 July 14 FEROS spectrum and N Mon 2012 Aug. 16th instantly reveals that the emission lines species observed are the same for both novae. This analogy allowed to identify N Mon 2012 as the γ-ray source observed with Fermi-LAT and classify it as a member of the ONe subclass, observed in early nebular phase.

An intense observational campaign has been conducted to study the late evolution of the nova, with a precious UV observation with HST/STIS in November 2012. Several ground observatories were dedicated to the study of the nova: the Nordic Optical Telescope, CTIO 1.5m SMARTS telescope equipped with the CHIRON cross-dispersed echelle spectrometer, Apache Point Observatory (APO) with the ARCES echelle spectrograh. All the observations discussed are reported in table 5.1.

Given the late time at which the nova was firstly observed (55 days post-outburst), the spectrum did not evolve much during the following observations, but few emission lines showed important changes. The list in Williams (2012) was important to properly identify several transitions.

Hydrogen Balmer lines always present asymmetric profiles, characterized by FWZI close to 4000 km s^{-1} and a pronounced emission peak at +1000 km s^{-1}, with little variations through the different observations. Only Hδ shows a peculiar changing in profile appearance, with the asymmetry going from the red to the blue wing. Unfortunately the optically thick phase of the nova was completely missed and we cannot measure

the maximum velocity for the absorption on the P Cyg profile, but we can confidently assume that it was close to ~ 4000 km s^{-1}.

Neutral helium appeared in several transitions: the weak singlet 6678Å showing a double peak; asymmetric profiles, similar to Balmer lines, for 5876Å and 7065Å; a weak but changing 4471Å lines, seen firstly as a double peak but then showing a pronounced emission on the negative velocity wing; 4713Å transition is visible but blends with other lines. He II line 1640Å is weak but clear in STIS spectrum, showing a (noisy) double peak profile. He II 4686Å is also present but strongly blended with N III 4640Åon the blue wing and with He I 4713Å on the red wind, but a superposition with He II 1640Å, for the November spectrum, shows a good agreement between the UV and optical transitions.

UV carbon transitions were present: weak C II 1334Å resonance doublet; weak and blended C II] 2323Å doublet; badly exposed C III] 1909Å were present and showing a profile similar to other intercombination lines; C IV 1548, 1550Å resonance lines were strong and it is possible to reconstruct the profile artificially blending two Hβ-looking profiles properly scaled.

Nitrogen lines crowd the spectra with four different ionization stages. In STIS spectrum, N V 1240Å, N IV] 1486Å and N III] 1750Å (this one being poorly exposed) were observed, while in optical [N II] 5755Å is very clear ([N II] 6548, 6583Å were always blended with Hα), N III 4638Å and other weaker transitions from N II and N III were present, some heavily blended with other species: N II 5001, 5679, 5938, 6346Å and N III 4517Å.

Also oxygen showed lines from four ionization stages. STIS spectrum reveal O I 1302Å weak but broad emission, O IV 1401Å (a wavelength position were Si IV 1402Å is usually expected but the centroid line does not agree with that transition), O II] 1663Å multiplet, O III 2320, 3050Å. Another possible line from O IV was present at 2975Å. Optical spectra showed forbidden lines from neutral, singly and doubly ionized oxygen: [O I] 6300, 6364Å (the 5577Å transition was never observed), [O II] 7319, 7330Å doublet, [O III] 4363, 4959, 5007Å. O I 8446Å is present, with a profile similar to [O I] 6300Å. O IV 5292Å was weak but detected.

[F III] 2930Å is surprisingly strong: this emission line, which is actually a doublet well resolved for RS Oph (Shore et al. 1996, this comparison allowed the correct identification), is not commonly observed and it was not recognized during V1974 Cyg outburst.

Being an ONe nova, neon lines are strong in both UV and wavelength spectra (and IR). Ultraviolet transitions from [Ne IV] 1602Å and [Ne V] 1574Å are actually detected only in ONe novae. Optical neon lines show different profiles according to their relative ionization, as above mentioned for helium lines: [Ne III] 3869, 3968Å are similar to [N II] and [O III], while [Ne IV] 1602, 2423, 4714, 4725 and Ne IV] 2974Å show narrower features.

Heavy elements transitions are also present. Mg II 2800Å doublet is the strongest feature in the near UV, but its components are blended. Sulfur shows up with the [S II] 4077Å and doublet 6716, 6730Å, all lines being badly blended with other species (e.g. Hδ and He II 6683Å) but confidently there. Argon is probably present, showing a weak

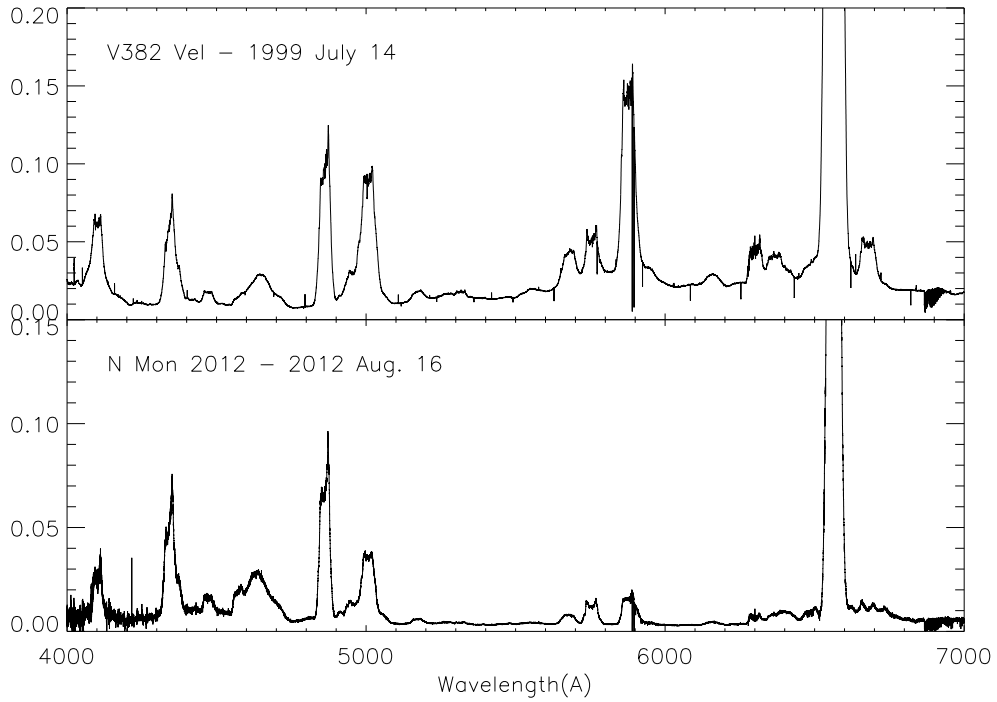

Figure 5.3: Comparison between the first high resolution spectrum with NOT/FIES (bottom) of N Mon 2012 and the 1999 July 14 spectrum with FEROS of V382 Vel (top). The remarkable similarities between these spectra made possible the identification, even before the appearance of neon lines.

emission from [Ar III] 7135Å. Iron lines are fundamental to trace the ionization stage of the ejecta in time. [Fe VII] 6086Å is present in late spectra, probably along with [Fe X] 6374Å, which perhaps suffers a complex blend with [O I] 6364Å, and [Fe XIV] 5303Å.

Extinction and distance

The determination of the interstellar reddening for N Mon 2012, eventually found to be E(B-V)=0.85, has been pursued using multiple indicators. A first estimate from Munari et al. (2012) suggested E(B-V)$\sim$0.3, using Na I interstellar line calibrations (Munari & Zwitter, 1997). However, UV interstellar lines observed with HST/STIS spectrum, although poorly exposed, reveal high positive velocity absorption, a feature also revealed in high resolution spectra from NOT for Na I lines. The radial velocity of the profiles are in agreement with H I 21cm profile from the LAB Survey, characterized by a line of sight H I column density of 5×10^{21} cm^{-2}. This value, using the E(B-V)/N_H calibration (Guever & Oezel, 2009), suggests an $E(B-V) = 0.85 \pm 0.05$. Another indication of severe interstellar extinction is the complete saturation of the Lyα (fig. 5.4). The comparison between Nova Mon and V1974 Cyg, conducted at the same UV development phase, brings a very confident distance of 3.6 kpc: the derivation is discussed in the next chapter. A lower limit on the bolometric luminosity is then $L > 9.8 \times 10^3 L_{\odot}$.

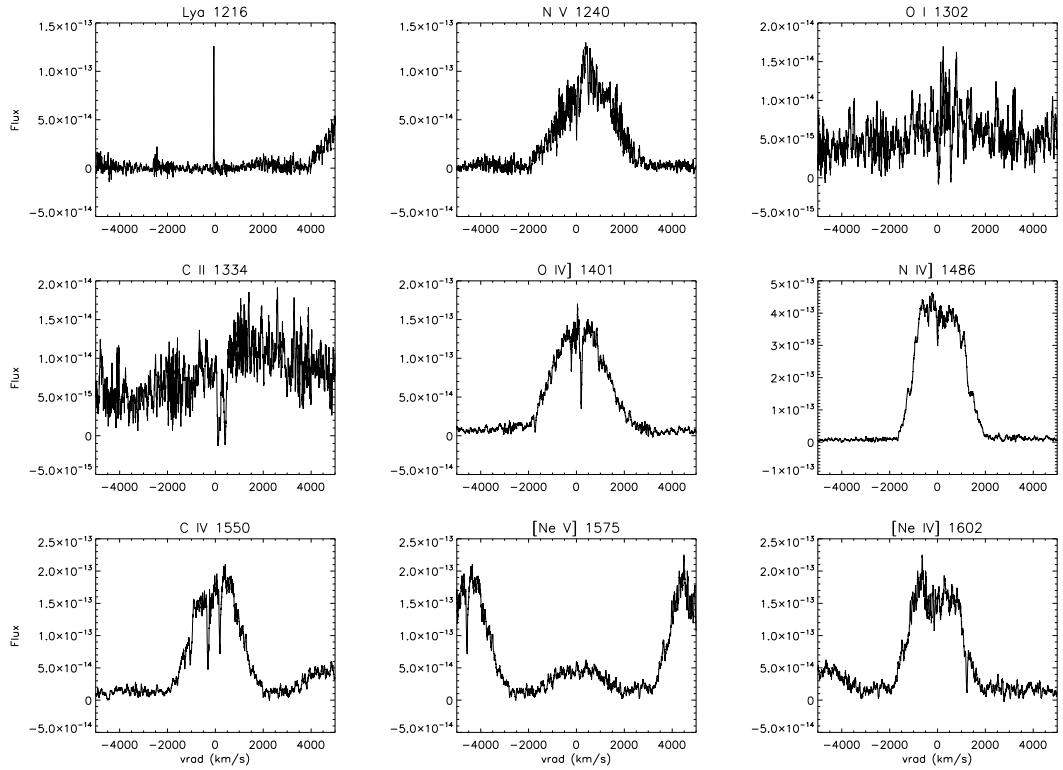

Figure 5.4: UV emission lines observed with HST/STIS on 2012 Nov. 20, day 151 after outburst.

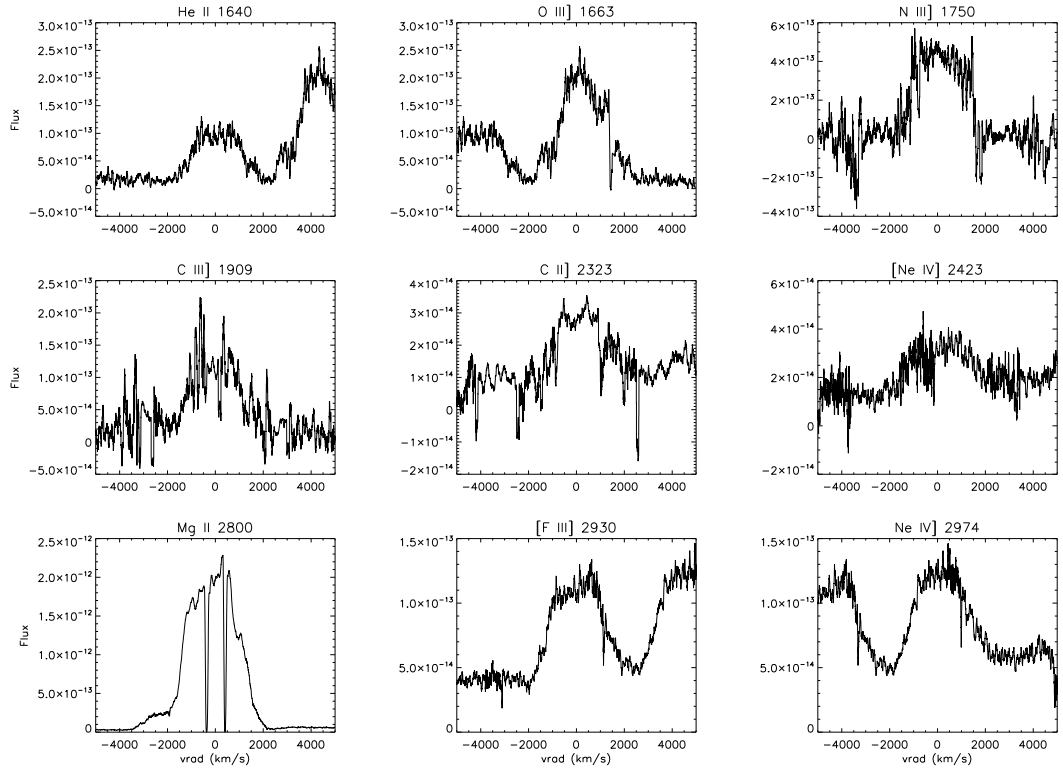

Figure 5.5: Continued from fig. 5.4.

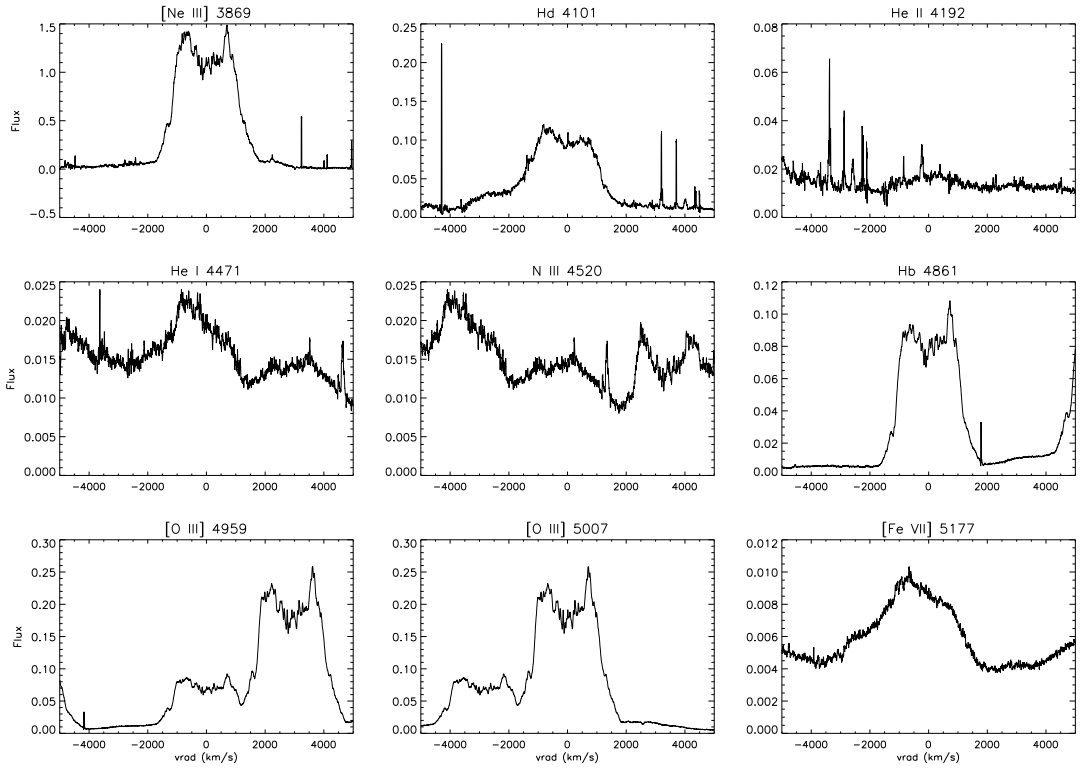

Figure 5.6: A selection of the optical emission lines observed with NOT/FIES on 2012 Nov. 21, day 152 after outburst.

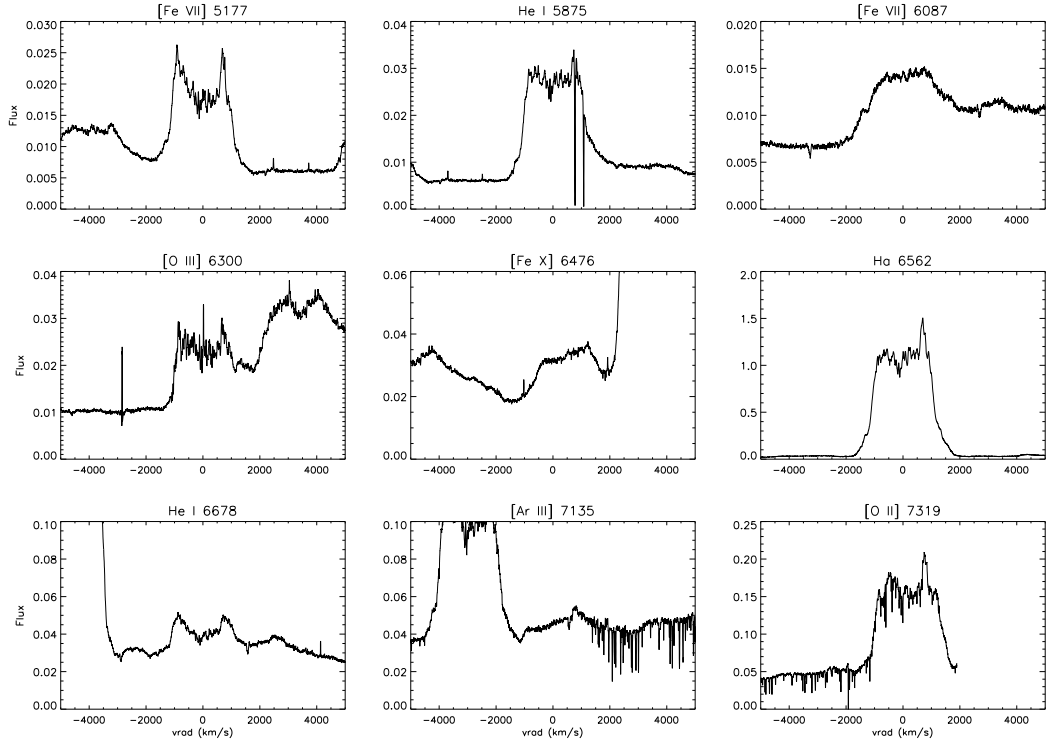

Figure 5.7: Continued from fig. 5.6.

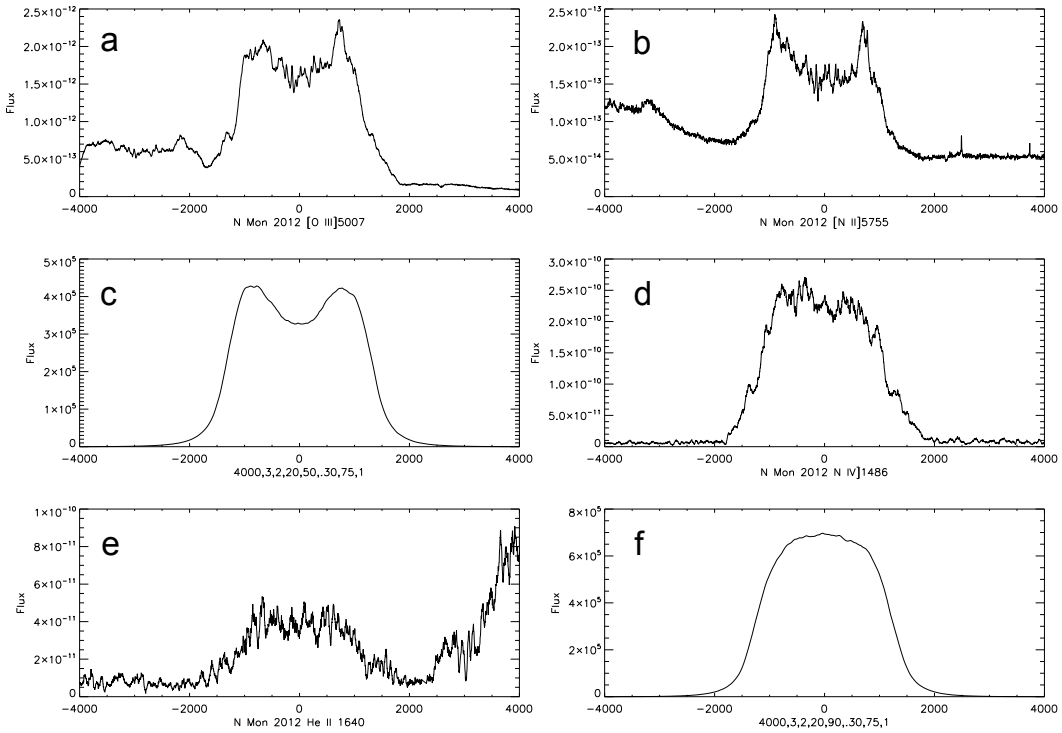

Figure 5.8: Emission lines observed on 2012 Nov. 20-21 with relative model profiles. a) [O III] 5007Å b) [N II] 5755Å c) Model profile with parameters v_{max} = 4000 km s^{-1}, θ_o=20^o, θ_i=50^o, $\Delta R/R$=0.3, i=75^o d) N IV] 1486Å e) He II 1640Å f) Model profile with parameters v_{max} = 4000 km s^{-1}, θ_o=20^o, θ_i=90^o, $\Delta R/R$=0.3, i=70^o. (Shore et al., 2013b)

Bipolarity of the ejecta

The Monte Carlo procedure applied for T Pyx nebular emission lines was also used for Nova Mon 2012. For this model, we had observational constraints from O'Brein et al. (2012) who managed to resolve the lobes of ejecta, suggesting an intermediate angle of view between the orbital plane and the lobes, hence a wide range of values for the model parameters generates line profiles similar to the ones observed. However, as T Pyx modeling suggested, forbidden lines transitions are modeled with more confined cones with respect to intercombination and permitted lines (fig. 5.8) and high ionization states transitions seem to form with augmented inner angles lobes. By the way, the most important evidence for bipolar ejecta is confirmed by a direct comparison with past ONe novae. The profile modeling gives reasonable results for the inner and outer radii: $R_{in} = 1.5 \times 10^{15}$cm, $R_{out} = 6.0 \times 10^{15}$cm.

Electron density and mass of the ejecta

The same procedure involving the [O III] lines diagnostics used for T Pyx nebular stage has been applied here. Unfortunately in this case we could not use the [N II] iso-electronic lines as simultaneous diagnostics, so we imposed the temperature to be $T_e = 10^4$ K. The electron density derived for Nov. 2012 spectrum is $n_e \approx 3 \times 10^7$ cm^{-3} in the inner region (fig. 5.10), with weak variations up to $|v_{rad}| < 1500$ km s^{-1}.

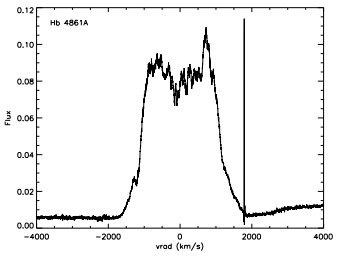

(a) Hβ on Nov. 21 2012.

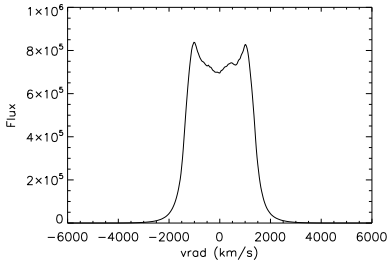

(b) Model profile with parameters v_{max} = 4000 km s^{-1}, θ_o=5^o, θ_i=60^o, $\Delta R/R$=0.3, i=70^o.

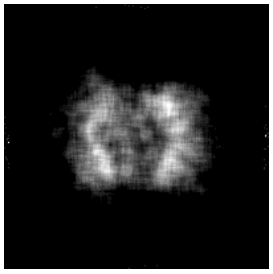

(c) Pseudo-image of the ejecta corresponding to the parameters used for the profile simulation (the image is cut at 30% of the peak flux).

Figure 5.9: Line profile modeling for recombination lines for Nov. 2012 spectrum.

To estimate the mass of ejecta, we used $H\beta$ diagnostics (as already done for T Pyx, see appendix for details). The measured integrated Hβ flux on Nov. 21 was 2.3×10^{-11} erg s^{-1} cm^{-2}, which becomes 4.0×10^{-10} when corrected for extinction. For the proposed distance, the line luminosity was $L(H\beta) = 8\times10^{36}$ erg s^{-1}. The electron density being $n_e \approx 3\times10^7$ cm^{-3} at an inner radius of 1.7×10^{15}cm ($v_{max} = 4000$ km s^{-1}), and $T_e = 10^4$ K, it gives a volume of 8×10^{45}cm^{-3}. Therefore, the filling factor is $f \approx 0.3$. This value is slightly higher than the one proposed by Vanlandingham et al. (2005), $f = 0.1$. Moreover, the fragmentation of the profiles suggests even lower values of f. In the end, we proposed the mass of the ejecta to be $M_{ej} \leq 2\times10^{-4} f M_\odot$, hence $M_{ej} \lesssim 6\times10^{-5}$.

Ionic abundances

To verify that Nova Mon 2012 is part of a homogeneous subclass of objects, we used the measured ejecta parameter (n_e, R_{in}, R_{out}, f, L) of Nova Mon and the abundances derived in Vanlandingham et al. (2005) for V1974 Cyg and Shore et al. (2003) for V382 Vel 1999 to predict the integrated line fluxes with the *CLOUDY* photoionization code. Because the X-ray source was active, we could use confidently the code. However, this was not an attempt to fit a photoionization model with the observations, but rather a way to identify quantitatively any clear abundance difference. The abundance set (logarithm of the number relative to H) was He=-1.00, C=-3.61, N=-2.52, O=-2.34, F=-6.54, Ne=-2.32, Na=-5.69,Mg=-3.70, Al=-4.20, Si=-4.75, S=-4.79, Ar=-5.40. The heavier elements were fixed at solar values. The source luminosity and effective temperature were estimated from reports of the Swift fluxes and spectra (Nelson et al., 2012) and our estimate of the luminosity. This model gives $\chi^2/(dof) = 68.5/29$, with the greatest contribution to the χ^2 coming from few not well fitted lines. The result is then consistent with the hypothesized chemical homogeneity of this subclass.

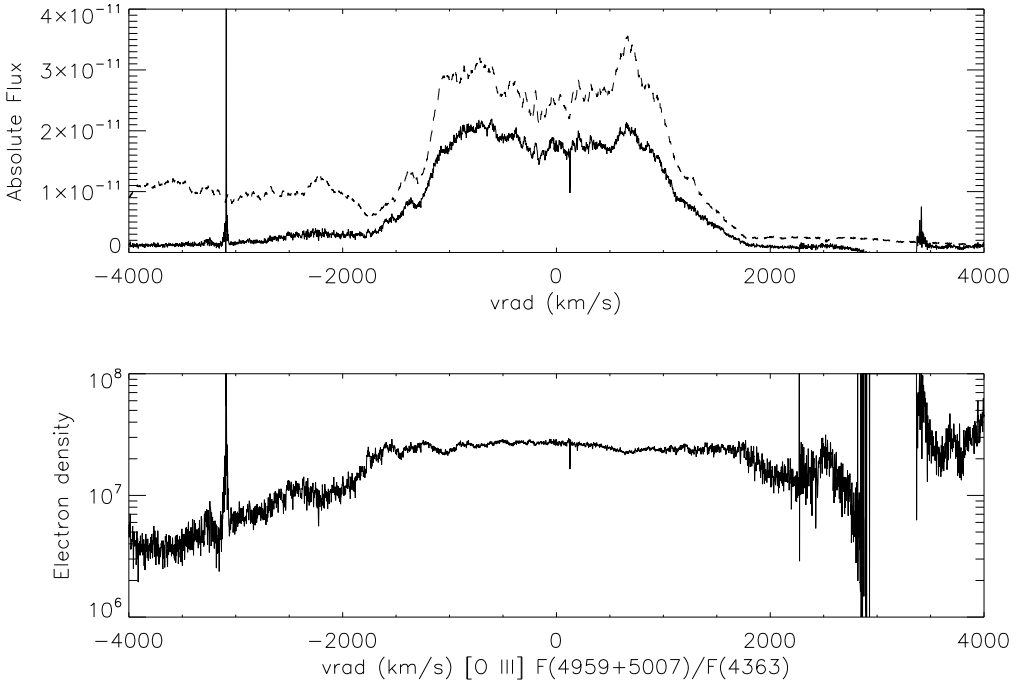

Figure 5.10: Top: November 2012 [O III] lines, 4363Å (dashed) after Hγ removal, 4959+5007Å (solid). Bottom: electron density evaluated with the flux ratio. (Shore et al., 2013b)

Chapter 6

"The Fabulous Four"

6.1 Past ONe novae

Thanks to an impressive series of observational campaigns, lasting for 18 years, conducted with IUE, along with high resolution spectroscopic data from HST and ground-based observatories, many ONe novae from the 1980s to nowadays were followed with very high cadence, shedding light on the evolution of this subclass in all wavelength regions. Although HST high resolution spectrographs have enormously improved our knowledge on the details of novae evolution (e.g. the C IV and N V absorption features in T Pyx late spectra, an unprecedented observation, IUE observed 36 CNe and 20 old novae, with a totally 1975 spectra collected: such an impressive campaign was fundamental to explore the ultraviolet spectral evolution of novae. This large database is public on the MAST archive and reviewed in the INES Atlas (Cassatella et al., 2004a).

ONe novae generally show more luminous outbursts, with faster ejecta, thus shorter t_2 (t_3) timescale, and neon overabundances with respect to CO novae, which generally present solar Ne abundance. ONe novae, as already mentioned, are also weak dust producers. Of course, exceptions are present. Novae V838 Her and V4160 Sgr were characterized by unusually fast ejecta (up to $\sim$7000 km s^{-1}) and overabundances of sulfur and low oxygen: it was suggested (Schwarz et al., 2007) that the peak temperature during the TNR was so high, up to 5×10^8K, that oxygen nuclei underwent efficient α-capture. Nova CP Cru 1996, thus defined as ONe nova, showed a Ne/O ratio close to 0.5 (rather than usual $\sim$3), suggesting that it could represent a link between the subclasses (Lyke et al., 2003). Nova QU Vul 1984 was another mysterious ONe nova (Schwarz, 2002): it showed the usual overabundance of Ne, Mg and Al, but ejected roughly 6×10^{-4}M$_\odot$, an order of magnitude greater than common ONe novae, and was a proficient dust producer, with a dust-to-gas ratio of 0.1%, a process typically associated with CO novae.

Because of the great similarities between the novae spectra, it was possible to connect V382 Vel with N Mon 2012. A more extended comparison with other two ONe novae extensively investigated with IUE, HST and ground observations, V1974 Cyg and Nova LMC 2000, revealed outstanding similarities between these novae.

First, the bipolar lobes modeling procedure has been extended to V1974 Cyg (which

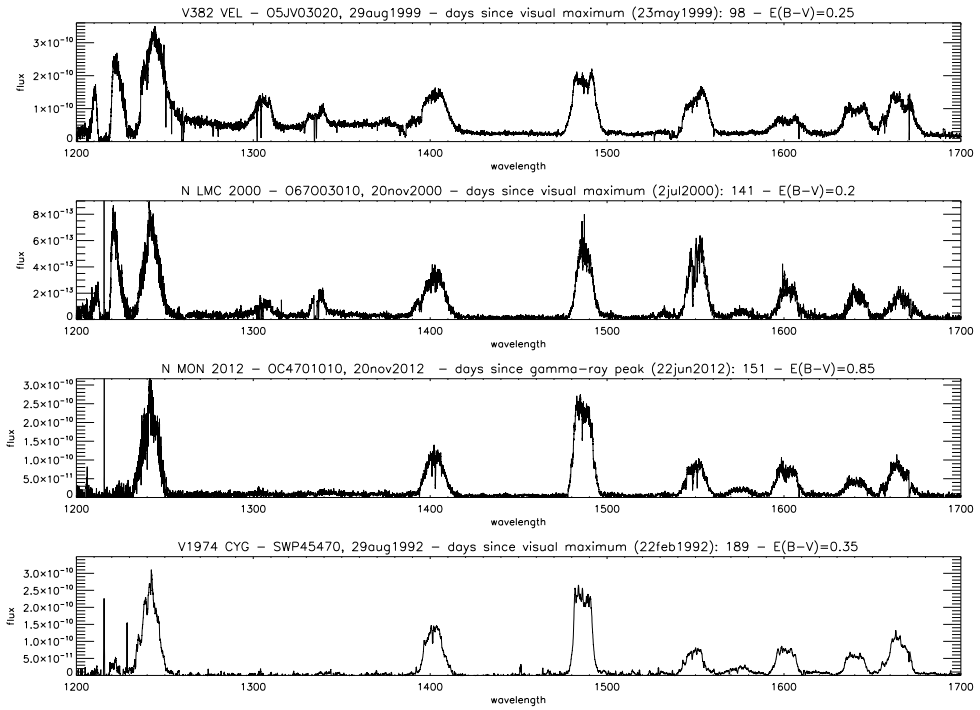

(a) Wavelength range 1200-1700Å.

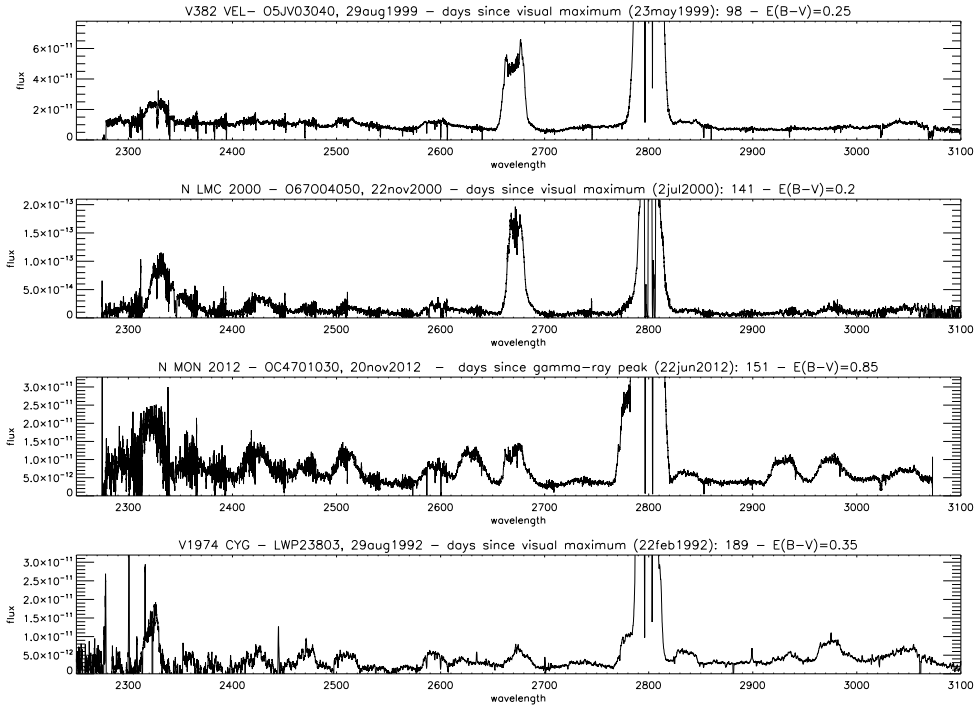

(b) Wavelength range 2200-3100Å.

Figure 6.1: ONe novae - late spectra sequence. The development of the spectra, from early (top) to late (bottom) phase, is marked by the fading of O I 1302Å, C II 1334,1335Å, Al II 2667Å, lines and the appearance of [Ne V] 1575Å. The Mg II 2800Å doublet is strong in all epochs. The N V 1240Å to N IV] 1486Å ratio decreases, The data from V1974 Cyg were observed with IUE in high dispersion mode, while V382 Vel 1999, N LMC 2000, and Nova Mon 2012 were observed with HST/STIS. (Shore et al., 2013b)

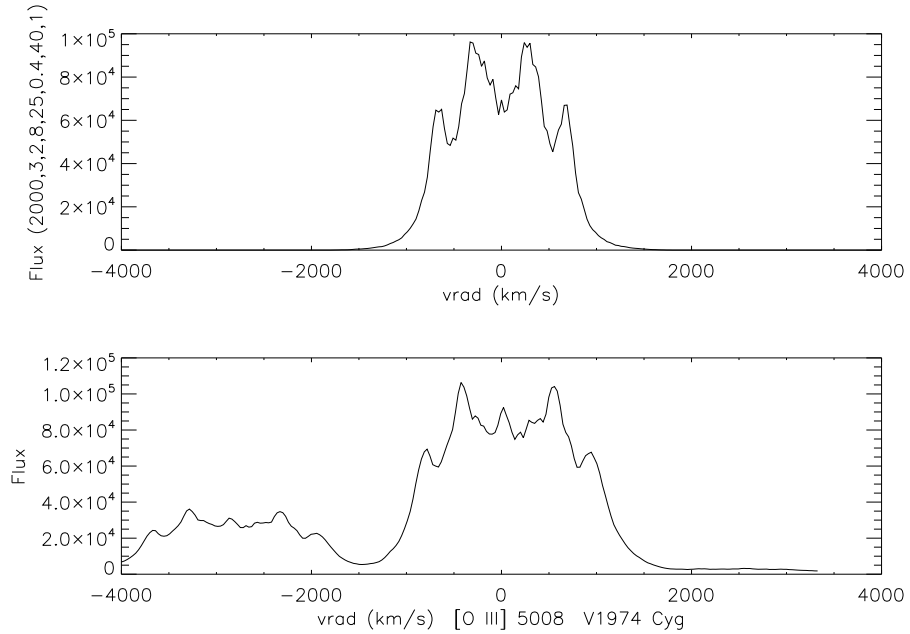

Figure 6.2: Modelled spectrum for [O III] 5007Å from V1974 Cyg on 1992 Sep. 25. The model parameters are v_{max} = 2000 km s^{-1}, θ_o=8^o, θ_i=25^o, $\Delta R/R$=0.4, i=40^o. (Shore et al., 2013b)

bipolar ejecta were spatially resolved, Shore et al., 1997) and V382 Vel, highlighting a very good agreement between simulated and observed line profiles.

Comparing N Mon 2012 ultraviolet spectra, finally unreddened with the extinction value previously discussed, with the long series of IUE observations for V1974 Cyg (E(B-V)=0.36$\pm$0.05), an unprecedented result appeared: the continuum flux from the day 165 V1974 Cyg spectrum overlaps, without scaling, the N Mon 2012 one, with emission lines fluxes also being similar. The spectra overlaps also in the optical, where we used a spectrum a medium resolution spectrum obtained at Perkins 1.8m Lowell Observatory, courtesy of R. M. Wagner, details in Austin et al. (1996). The comparisons are showed in figures 6.5 and 6.6. This suggests that these two novae, although affected by different interstellar extinctions, are equally distant from us. From these considerations, the proposed distance to Nova Mon is 3.6$\pm$0.3 kpc. This distance determination is an unprecedented result.

6.2 New Cosmologically Significant Standard Candles

The uniform spectroscopic behavior of the ONe novae subclass was already known in the 1980s (Starrfield et al., 1986) and the recent HST spectra confirm unambiguously this observational evidence. What we observed is in fact a strong confirmation of a unique spectral development sequence in UV and optical wavelength.

Each individual nova develops spectroscopically at its own rate, which is likely dependent only on the ejected mass and abundances. However, the continuum emission appears to be the same if we compare two novae at the same spectroscopic stage. To characterize the spectral development sequence, we have to follow the evolution of sev-

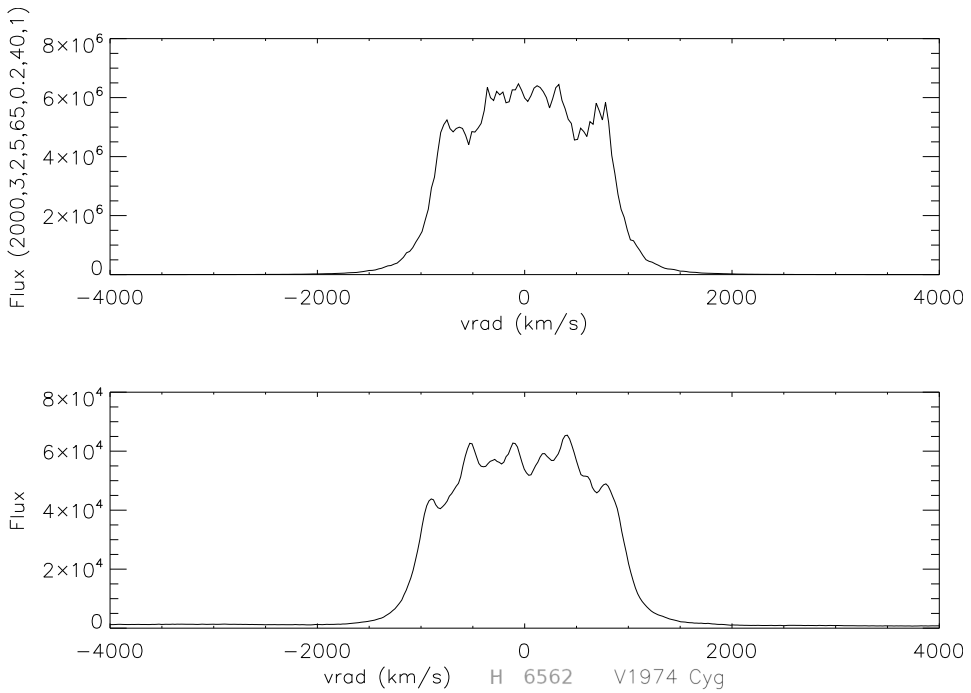

Figure 6.3: Modelled spectrum for Hα from V1974 Cyg on 1992 Sep. 25. The model parameters are v_{max} = 2000 km s^{-1}, θ_o=5^o, θ_i=65^o, $\Delta R/R$=0.2, i=40^o. (Shore et al., 2013b)

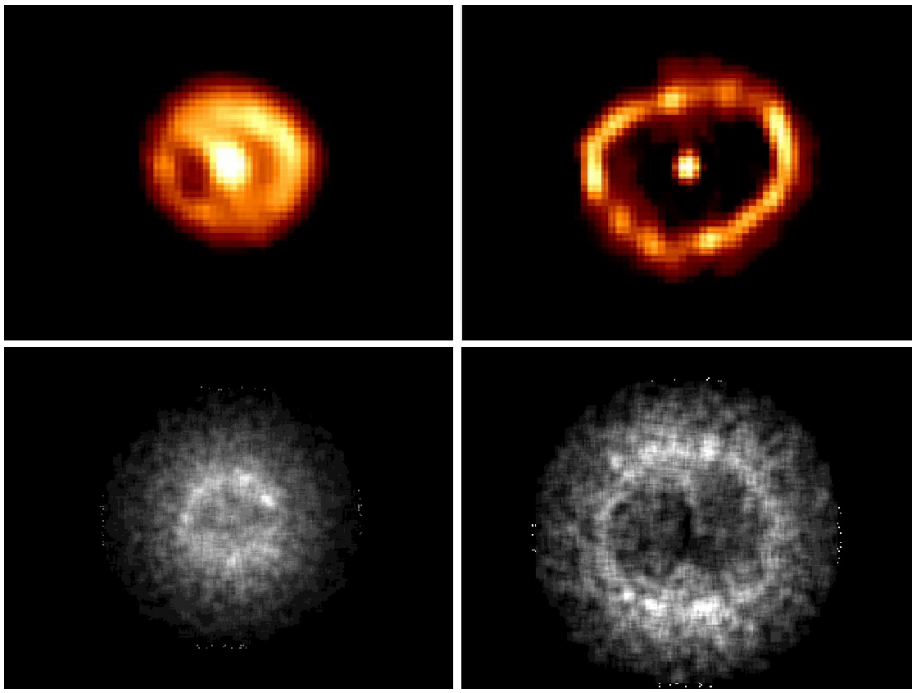

Figure 6.4: Top: V1974 Cyg remnant on days 467 (left) and 726 (right) after the outburst, as in fig. 4.27; bottom: pseudo-images of the ejecta corresponding generated with the parameters v_{max} = 2000 km s^{-1}, θ_o=10^o, θ_i=80^o, $\Delta R/R$=0.3, i=35^o (left) and v_{max} = 2000 km s^{-1}, θ_o=10^o, θ_i=60^o, $\Delta R/R$=0.5, i=35^o (right). (Shore et al., 2013b)

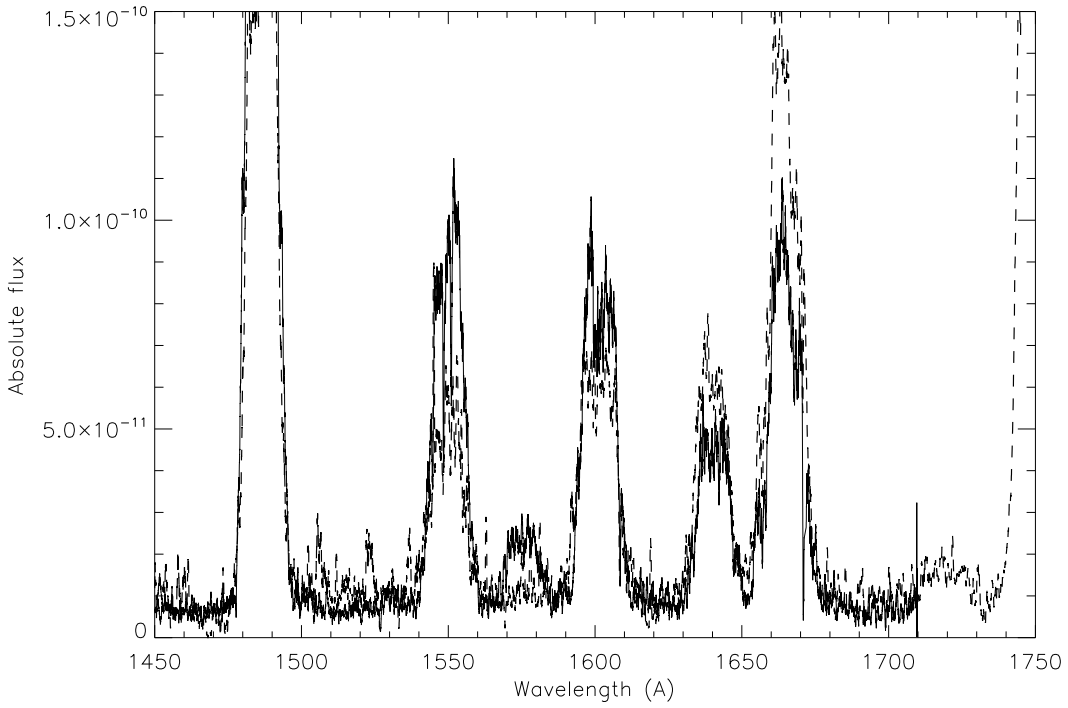

Figure 6.5: Comparison between V959 Mon 2012 Nov. 20 STIS spectrum (solid) with V1974 Cyg 1992 Sep. 25 IUE spectrum (dashed). The fluxes are corrected for the relative extinctions and binned to V1974 Cyg resolution. (Shore et al., 2013b)

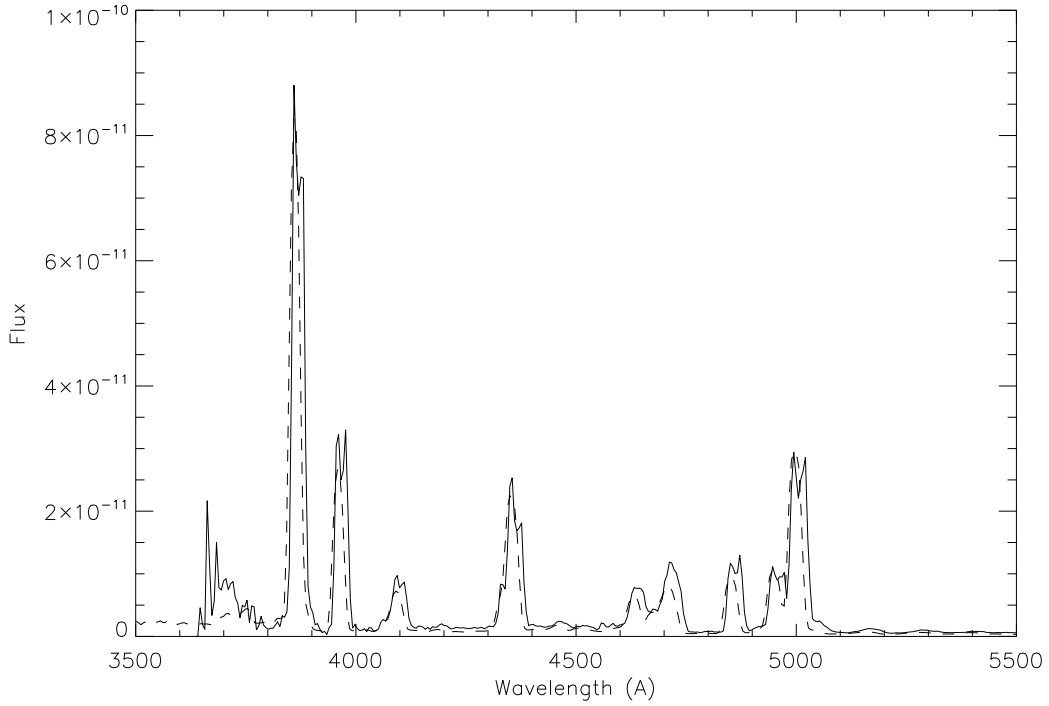

Figure 6.6: Comparison between V959 Mon 2012 Nov. 21 NOT spectrum (solid) with V1974 Cyg 1992 Sep. 25 (dashed). The fluxes are corrected for the relative extinctions and binned to V1974 Cyg resolution. (Shore et al., 2013b)

eral crucial transitions: the disappearance of emission from O I 1302Å and C II 1335Å, which hints at the complete ionization of the ejecta; the appearance of neon lines, i.e. [Ne IV] 1602Å [Ne V] 1575Å, a perfect signature of high Ne abundance; the emission from [Fe VII] 6086Å, which signals the active SSS.

From the discussed properties, we may finally suggest this subclass of novae to be a potential new class of Standard Candles. The basic hypothesis of this technique is the common physical characteristics of the WD. Once the spectra are properly dereddened, with extinctions being estimated without any assumption on distance, and the phase of the spectral development is established, comparing the continuum and line fluxes, we can estimate the relative distances: with UV spectra for only four ONe novae, the uncertainty on the relative distances is 20%.

Chapter 7

Conclusions

During the last two years, with multi-wavelength observations, γ-rays with Fermi/LAT, X-Ray with Swift, UV with Hubble Space Telescope, and optical with several international observatories, and the important contribution of archival data, it was possible to investigate long-standing problems and discover new techniques and processes about classical and recurrent novae.

My work was concentrated on two novae, T Pyxidis 2011 and V959 Monocerotis 2012, but the analysis included many other systems in order to explore all the different properties of the nova phenomenon and make important statements about their classification.

We followed the spectroscopic development of T Pyx with unprecedented temporal extension, with UV observations by HST from the early phase of the explosion to the late quasi-quiescent state, two years after the outburst. It has been possible to study in great details the evolution of the ionization structure of the ejecta, and the analysis on the interstellar medium, although not related to the evolution of the outburst, was very important to properly distinguish the interstellar features in the spectra from those coming from the nova ejecta. With a simple, 3D Monte-Carlo model, we also confidently modeled the geometry of the ejecta, during the nebular phase of the outburst, comparing observed and simulated line profiles: we suggest that a bipolar ejection occurred, and it is important to emphasize how this behavior seems general to many. Few questions about this famous nova remain answered: while the white dwarf mass is plainly very high, close to the Chandrasekhar limit, what is its eventual fate? Will it be a Supernova type Ia? Why its outbursts cadence is irregular?

The energetic γ-ray emitter V959 Monocerotis, although observed only during the nebular phase, has been fundamental to help us understanding the spectroscopic development of the ONe subclass. Through the comparison with other ONe novae, it was possible to determine the distance of this system and to propose a potential new class of distance calibrators. However, new important questions need answer: what is the mechanism leading to high energy γ emission? Why the ejecta geometry is, if not exactly bipolar, unambiguously non-spherical?

Today, another nova is already being intensively followed: with the recent outburst of Nova Del 2013, on August 14th 2013, the fourth nova to be detected by Fermi/LAT,

several mid and high resolution optical spectra have already been collected.

Finally, it is interesting to make an analogy between the evolution of T Pyx (or any CN) outburst and the cosmological re-ionization and Lyα forest development. In both pictures, an initially expanding completely ionized gas undergoes a massive recombination event. Expansion proceeds steadily, optical depth decreases and an ionization wave, driven by the hot central source, travels outward. The expansion rate, local opacity and ionizing source strength establish the local ionization conditions of the gas: the inner, denser regions can more easily recombine, while the outer portions remain highly ionized. Once the ionizing sources are off, the ionization conditions of the gas are frozen and recombination is driven by the expansion rate and the local particle density. The basic point of this analogy is to emphasize the universality of the physical processes that we observe for novae, which are in fact typical of expanding media, here-hence to encourage further investigation for any astrophysical problem.

Publications

Cheung, C. C., Shore, S. N., De Gennaro Aquino, I., Charbonnel, S., Edlin, J., Hays, E., Corbet, R. H. D. & Wood, D. L. 2012, *Possible Association of the Gamma-ray Transient Fermi J0639+0548 with Nova Mon 2012*, ATel #4310, `www.astronomerstelegram.org/?read=4310`

Shore, S. N., Schwarz, G. J., De Gennaro Aquino, I., Augusteijn, T., Walter, F. M., Starrfield, S. & Sion, E. M. 2013, *The spectroscopic evolution of the recurrent nova T Pyxidis during its 2011 outburst. II. The optically thin phase and the structure of the ejecta in recurrent novae*, A&A, **549**, A140, `http://dx.doi.org/10.1051/0004-6361/201220337`

Shore, S. N., De Gennaro Aquino, I., Schwarz, G. J., Augusteijn, T., Cheung, C. C., Walter, F. M. & Starrfield, S. 2013, *The spectroscopic evolution of the γ-ray emitting classical nova Nova Mon 2012. I. Implications for the ONe subclass of classical novae*, A&A, **553**, A123, `http://dx.doi.org/10.1051/0004-6361/201321095`

De Gennaro Aquino, I., Shore, S. N., Schwarz, G. J., Mason, E., Starrfield, S. & Sion, E. M., *The spectroscopic evolution of the recurrent nova T Pyxidis during its 2011 outburst III. The ultraviolet development from iron curtain through the post-X-ray turnoff*, A&A, submitted on 26th August 2013.

Appendix A

Spectroscopic diagnostic tools

The multi-wavelength study of astrophysical sources requires a deep knowledge of the opacity physical mechanisms. It is not intended here to discuss all the radiative and atomic physics processes governing the formation and shaping of spectra but to describe only specific problems faced during the development of this work.

A classic reference covering the basic theory behind radiative processes in astrophysical gases is Spitzer (1978), while a detailed and complete modern overview regarding nebulae is Osterbrock & Ferland (2006).

A.1 Absorption line spectrum

The life of a photon in a gas is described through radiative transfer. The presence of atoms and molecules in the medium affects the motion and energy of the photons.

The one dimensional radiative transfer equation is

$$\frac{dI_\nu}{dl} = -k_\nu I_\nu + \rho j_\nu \tag{A.1}$$

where I_ν is the intensity so that $I_\nu d\nu d\omega dA dt$ is the energy of those photons which during a time interval dt pass through the area dA, whose frequency lies within the element $d\nu$ about ν, within the solid angle ω, dl is the length of the cylinder with base dA, k_ν is the absorption coefficient, hence $k_\nu I_\nu dl dA d\nu d\omega dt$ is the energy absorbed from a beam of intensity I_ν, ρ is the density, and j_ν is the emissivity per unit mass, so that the energy emitted by the volume $dldA$ is $\rho j_\nu dl dA d\nu d\omega dt$. We introduce the *optical depth* τ_ν

$$d\tau_\nu = -\rho k_\nu dl \tag{A.2}$$

define as $\tau_\nu = 0$ at the observed, so, if k_ν is positive, τ_ν increases towards the source.

We now introduce atomic transitions, called *bound-bound* or *line* transitions. In a simple two atomic states gas, with the n_i and n_j the lower and upper levels separated by the energy $h\nu_{ij}$, the radiation probability for an electron to spontaneously go from level j to level i is A_{ji}. However, electrons may be stimulated to go from one level to the other, hence the Einstein coefficients for stimulated emission (downward transition)

probability B_{ji} and the stimulated absorption (upward transition) probability B_{ij}. A simple relationship ties together this three coefficients

$$g_i B_{ij} = g_j B_{ji} = \frac{c^3}{8\pi h \nu_{ij}^3} g_j A_{ji} \tag{A.3}$$

where g_i and g_j are the statistical weights of levels i and j.

If this two level gas is just a simple absorber, we forget about j_ν in the radiative transfer equation, which becomes, once used the optical depth definition and integrated along the line of sight

$$I_\nu = I_\nu(0) e^{-\tau_\nu} \tag{A.4}$$

where $I_\nu(0)$ is the *continuum intensity*, i.e. the intensity at a frequency far from the transition frequency. We can express k_ν as $k_\nu = n_j s_\nu = n_j s \phi(\Delta\nu)$, where $s = \int s_\nu d\nu$, i.e. the integrated absorption cross section integrated over the line, and $\phi(\Delta\nu)$ is the *line profile*, which is a function of $\Delta\nu = \nu - \nu_{ij}$, and describes the frequency distribution of s_ν. If we then define the *column density* N_i by $N_i = \int n_i ds$, and integrate the radiative transfer equation along the line of sight, we obtain

$$\tau_\nu = N_j s \phi_a(\Delta\nu) \tag{A.5}$$

where $\phi_a(\Delta\nu)$ is an average of $\phi(\Delta\nu)$ along the line of sight. If we then integrate over frequency we have

$$N_j = \frac{1}{s} \int \tau_\nu d\nu. \tag{A.6}$$

Leaving the details about its derivation, for a Gaussian profile s is defined as $s = h\nu_{ij} B_{ij}/c$, but usually the *oscillator strength* f_{ij} is used, so that

$$s = \frac{\pi e^2}{m_e c} f_{ij}. \tag{A.7}$$

A.1.1 Line profiles

An atomic transition line profile has an intrinsic broadening due only to the finite lifetime of the exited level. The derivation of the intrinsic profile of a transition line comes naturally when solving the classic equation of motion for a damped harmonic oscillator interacting with an electric field: the resulting cross section, known as *Lorentzian profile*, is

$$\phi_{Lor}(\Delta\nu) \propto \frac{\gamma}{(\Delta\nu)^2 + (\gamma/2)^2} \tag{A.8}$$

where γ is the *radiation damping constant*, $\gamma = 2\pi e^2/3 m_e c \lambda^2$.

However, the line profile may be broadened by several broadening mechanisms. If we just consider Doppler broadening, so that $\phi_a(\Delta\nu)$ equals $P(v)dv$, i.e. the fraction of atoms whose radial velocities lies within the velocity range dv, and recall the usual

formula

$$\frac{v}{c} = \frac{\Delta\nu}{\nu_{ij}} \tag{A.9}$$

we have a simple description of $\phi_a(\Delta\nu)$

$$\phi_a(\Delta\nu) = \frac{c}{\nu_{ij} b \sqrt{\pi}} e^{-v^2/b^2} \tag{A.10}$$

where b is the velocity spread, defined as $b^2 = 2kT/m$, i.e. the thermal collision broadening.

The Gaussian profile doesn't change if we add an average velocity shift. It does change however, if we add disordering to the particles through *turbulence*: the main effect is to add random momentum to the particles (the mean velocity doesn't change), broadening the line and reducing the optical depth.

The Gaussian and the Lorentzian profiles act together to shape the line profile: the result is the *Voigt* profile, i.e. the convolution of the atomic velocity distribution with the intrinsic profile. The only parameter that characterizes the Voigt profile is the ratio between the radiation damping broadening and the Doppler broadening, expressed in the same units, $a = (\Delta\lambda)_{damp}/(\Delta\lambda)_{Dopp}$. In figure A.1 we can see the main differences between Gaussian and Lorentzian profiles alone and the combined effect of the Voigt profile: for the same central intensity, the high velocity dispersion is much higher for the Lorentzian profile (which actually as an infinite velocity dispersion); the Voigt profile, increasing the damping parameter a, develops more saturated wings and less saturated cores.

A.1.2 Measuring column densities

From the absorption lines in a spectrum we can understand several physical and chemical properties of the gas along the line of sight. When looking towards a bright source, we must consider the possibility that not all the photons observed originate from that specific source nor that the photons "missing" near an absorption line where absorbed by the same parcel of gas. In the non-realistic approximation of complete interstellar void between us and a star, the absorption lines observed in the spectrum must originate in the atmosphere or the circumstellar environment of the object. On the other hand, the spectrum obtained looking towards a very bright source embedded in a non-completely optically thick cloud will reasonably be populated by many absorption lines coming from the gas on the line of sight. In a real case, one will observe the atmospheric absorption lines of the star plus many other interstellar features (ground observatories will observe also Earth atmosphere spectral contaminations).

For example, close OB stars are perfect candidates to study the ISM through absorption line measurements, since their atmospheres are almost featureless in ultraviolet and optical spectrum.

The *curve of growth* technique (the first appearance in literature goes back to Unsöld et al., 1930) has been used for decades to estimate the column densities of ions which

showed absorption lines in UV/optical/IR. It is extremely useful when the spectral resolution is not sufficiently high to fully resolve the line profile, i.e. when the instrumental spread function is larger or comparable to the intrinsic width of the line. In this case, it is customary to determine the *equivalent widths* of a line, which measures the fraction of energy removed from the spectrum by that transition. This measurement is unaffected by the instrumental resolution.

Specifically, the equivalent width W_λ of the transition at λ wavelength

$$W_\lambda = \int_{\lambda 1}^{\lambda 2} \Big[1 - \frac{I}{I_c}\Big] d\lambda = \int_{\lambda 1}^{\lambda 2} \Big[1 - e^{-\tau(\lambda)}\Big] d\lambda \tag{A.11}$$

If the optical depth is small enough so that we can expand $e^{-\tau}$, and assume that only Doppler broadening is relevant, we have a direct relationship between W_λ and N_i

$$\frac{W_\lambda}{\lambda} = \frac{\pi e^2}{m_e c^2} N_i \lambda f_{ij}. \tag{A.12}$$

This relationship is valid when the optical depth is very small, in the so called *linear* part of the curve of growth, because W_λ/λ is proportional to $N_i \lambda f_{ij}$. However, when optical depth increases (for the same transition, this happens only because of N_i increasing), saturation effects of the Gaussian profile only slightly enlarge the line, hence slightly increasing the equivalent width: $W_\lambda \lambda \propto ln(N_i \lambda f_{ij})$, in the so called *flat* portion of the curve of growth. For very strong lines, the damping wings of the profiles, i.e. the Lorentzian wings of the Voigt profile, become important: in this regime, the *square-root* section of the curve of growth, $W_\lambda/\lambda \propto \sqrt{N_i f_{ij} \gamma \lambda^2}$.

A simulated curve of growth is displayed in fig. A.2.

A.2 Emission line spectrum

A multitude of astrophysical sources present spectra characterized by line emission: planetary nebulae, the solar corona, novae ejecta etc.

Emission lines are the outcome of several different physical processes responsible for populating excited states, mainly collisions and radiative excitation. The complete physical description of the processes leading to line emission is definitely more complicated than absorption line processes, so all the mathematical details will be avoided in favor of physical arguments.

A.2.1 Recombination lines

In sufficiently dense ionized gas, free electrons can be captured by ionized atoms in high energy atomic levels, a process called *recombination*.

In thermal equilibrium, ionization and recombination rates are balanced and (considering for simplicity only hydrogen) electrons, protons, and neutral H populations are described by the *Saha equation*.

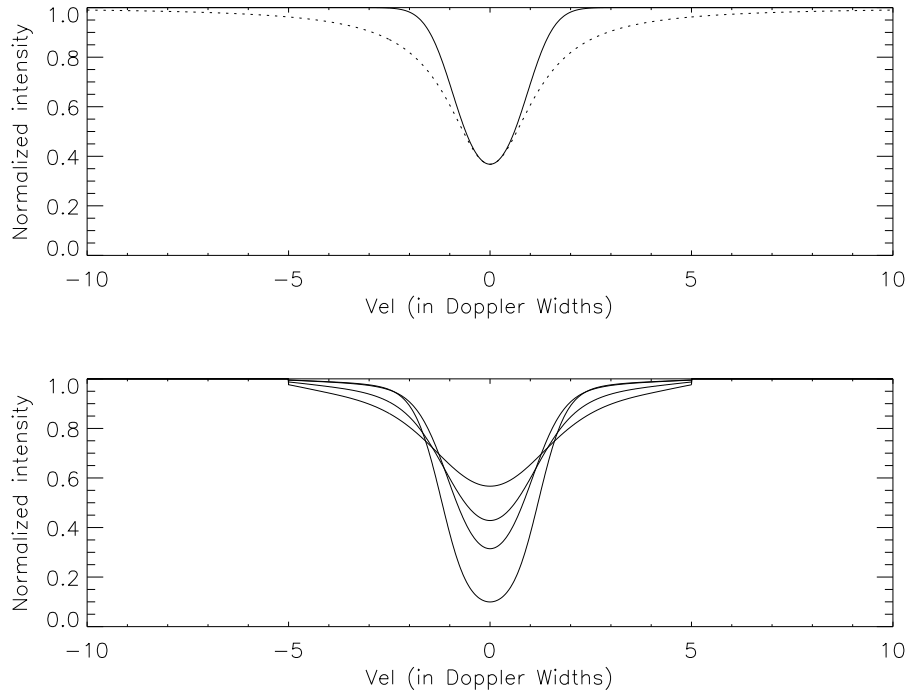

Figure A.1: Top panel: Gaussian (solid) and Lorentzian (dots) profile with identical central intensity (note the broadening of the wings on the Lorentzian profile); bottom panel: Voigt profiles with increasing (from top to bottom) values of a, the main effect is to broaden the line relative to the Gaussian core.

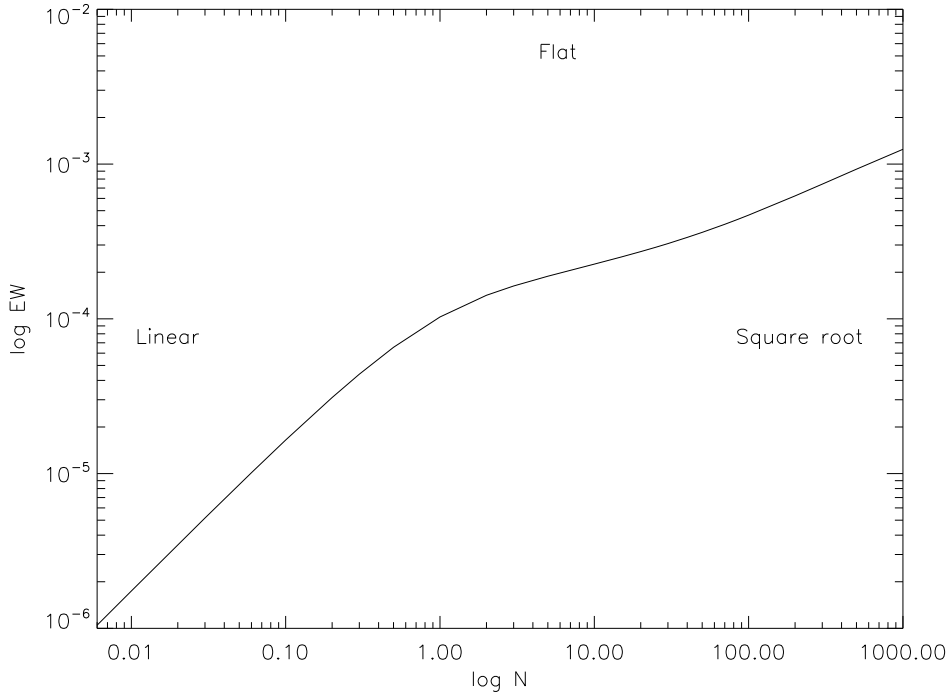

Figure A.2: Curve of growth model. In real measurements, the x-axis, here indicated simply as the logarithm of N, must be shifted to account for the additional term $logf\lambda$; the y-axis must also be shifted by the amount $-log\lambda$. Damping parameter a=0.3.

When electrons follow the atomic level "ladder", they emit photons observable as emission lines. For H, transitions involving the n=1 (ground) as final state are called *Lyman* series, observable in the UV range; the *Balmer* series, optical lines, involve transition towards n=2 state; the infrared *Paschen* series for n=3 state and so on.

Hα/Hβ

An important diagnostic tool using recombination line is the ratio between the integrated emission of Hα and Hβ Balmer lines to estimate the extinction. It is assumed that the main effect of dust grains to photons emitted by the nebula is to remove them from the line of sight, and the scattering of photons into the light beam is negligible. Being the reddening wavelength dependent, the effect on Hα photons will be different than for the Hβ photons. The source is assumed completely optically thin.

If we measured the integrated flux of the lines, and know the intrinsic ratio of the lines for our astrophysical objects, then we can estimate E(B-V) with

$$\frac{I(H\alpha)}{I(H\beta)} = \frac{F(H\alpha)}{F(H\beta)} 10^{1.33\,E(B-V)[f(H\alpha)-f(H\beta)]} \tag{A.13}$$

where I and F are the intrinsic (unreddened) and observed fluxes of the lines, and $f(\lambda)$ is the reddening curve.

Hβ flux

In nebular gases diagnostics, the luminosity of the $H\beta$ line is used to determine several physical properties of the emitting gas.

Suppose that the investigated nebula is an homogeneous sphere with an electron density n_e at temperature T_e and the emitting volume is characterized by a filling factor f. The observed flux from $H\beta$ is

$$F_{H\beta} = \frac{4\pi R^3}{3} \frac{1}{d^2} \alpha^{eff}_{H\beta}(T_e) n_e^2 h\nu_{H\beta} f \tag{A.14}$$

where R is the radius of the sphere, d the distance, and $\alpha^{eff}_{H\beta}(T_e)$ is the effective recombination rate of the transition, which values is $\sim 10^{-14}$ cm^{-3} s^{-1}. From n_e we can then estimate the hydrogen mass of the volume

$$M = \frac{4\pi R^3}{3} m_H n_e f. \tag{A.15}$$

A.2.2 Forbidden lines diagnostics

The temperature and electron density in a nebula may be determined studying the intensity ratios of several pairs of lines that fit certain physical approximations.

[N II] and [O III] diagnostics

Without going into the details of the calculations, it is possible to measure the temperature of a rarefied, not completely ionized gas, if we observe emission lines from the same ion involving different upper levels with substantial excitation energy difference. For O III, the excited (collisionally) state $2s^2 2p^2\ ^1S_0$ de-excites through a magnetic dipole transition to the $^3P_1$ level (λ2321Å) or an electric-quadrupole transition to the $^1D_2$ level (λ4363Å); the latter subsequently de-excites mainly via two magnetic dipole transitions to the $^3P_2$ (λ5007Å) or to the $^3P_1$ (λ4959Å). But the $^1D_2$ is populated faster by collisional excitation from the ^3P level than by radiative de-excitation of the ^1S level, so that the rate of $1^D - 3^P$ "jumps" depends strongly on T.

The ratio of the fluxes from the [O III] lines 4363, 4959, 5007Å is a confident "thermometer" for nebular sources. The underlying hypothesis are the low optical depth of medium and low densities, up to $n_e \sim 10^5$ cm^{-3}, but the complete derivation requires careful considerations on the excitation and de-excitation processes.

The relationship is then

$$\frac{j_{4959} + j_{5007}}{j_{4363}} = \frac{7.90}{1 + 4.5 \times 10^{-4} n_e / T^{1/2}} e^{3.29 \times 10^4 / T} \tag{A.16}$$

The derivation is identical if we study the iso-electronic transition, involving the same atomic levels, of [N II] 6548, 6583, and 5755Å lines

$$\frac{j_{6548} + j_{6583}}{j_{5755}} = \frac{8.23}{1 + 4.4 \times 10^{-3} n_e / T^{1/2}} e^{2.5 \times 10^4 / T} \tag{A.17}$$

Combining both tools, we can simultaneously constrain n_e and T_e.

[O II] diagnostics

To measure the average electron density in a nebula, we have to measure the effect of collisional de-excitation.

If we observe two lines of the same ion, emitted by different levels with nearly the same excitation energy, the relative excitation rates to the levels must depend strongly on the ratio of collision strengths. In the end, if two levels have different radiative transition probabilities or different collision de-excitation rates, the relative of populations of the two levels, hence the ratio of the intensity of the lines, will depend on density.

The ratio of the [O II] lines 3729 and 3726Å as well as the iso-electronic transitions from [S II] 6716 and 6731Å are suitable transitions for this diagnostics.

Bibliography

Abdo, A. A. et al. (Fermi-LAT collaboration) 2010, *Science*, **329**, 817

Anupama, G. C. 2008, *ASP Conf. Series*, **401**, 31

Anupama, G. C. & Kamath, U. S. 2012, *Bull.Astr.Soc.India*, **40**, 161

Arp, H. C. 1956, *AJ*, **61**, 15

Ashok, N. M. & Banerjee, D. P. K. 2003, *A&A*, **409**, 1007

Asplun, M., Grevesse, N, Sauval, A. J. & Scott, P. 2009, *ARA&A*, **47**, 481

Austin, S. J. et al. 1996, *AJ*, **111**, 869

Bode, M. F. 2010, *Astr.Nach.*, **331**, 160

Brand, J. & Blitz, L. 1993, *A&A*, **275**, 67

Casanova, J., José, J., Garcia-Berro, E., Shore, S. N. & Calder, A. C. 2011, *Nature*, **478**, 490

Cassatella, A., Gonzalez-Riestra, R. & Selvelli, Pierluigi 2004a, *INES Guide No. 3 - Classical Novae*, ESA SP-1283

Cassatella, A., Lamers, H. J. G. L. M., Rossi, C., Altamore, A. & Gonzalez-Riestra R. 2004b, *A&A*, **420**, 571

Catchpole, R. M. 1969, *MNRAS*, **142**, 119

Chesneau, O. et al. 2011, *A&A*, **534**, L11

Cheung, C. C. 2013, *4th Fermi Symposium proceedings*, *arxiv* **1304.3475**

Cheung, C. C. et al. (Fermi/LAT collaboration) 2012a, *ATel 4224*

Cheung, C. C. et al. 2012b, *ATel 4310*

De Gennaro Aquino, I. et al. 2013, *A&A*, **submitted, 2013 Aug. 26th**

Della Valle, M. & Livio, M. 1995, *ApJ*, **452**, 704

Della Valle, M., Pasquini, L., Daou, D., & Williams, R. E. 2002, *A&A*, **390**, 155

Duerbeck, H. W. 2008, in *Classical Novae*, 2nd Ed. (Eds. Bode, M. F. & Evans, A.) Cambridge University Press, Chapter 1

Duerbeck, H. W. & Seitter, W. C. 1979, *ESO Messenger*, **17**, 3

Friedman, S. D. et al. 2011, *ApJ*, **727**, 33

Fujimoto, M. Y. 1982, *ApJ*, **257**, 752

Geisel, S. L., Kleinmann, D. E. & Low, F. J. 1970, *ApJ*, **161**, L101

Gil-Pons, P., García-Berro, E., José, J., Hernanz, M. & Truran, J. W. 2003, *A&A*, **407**, 1021

Guever, T & Oezel, F. 2009, *MNRAS*, **400**, 2050

Hachisu, I., Kato, M. & Schaefer, B. 2003, *ApJ*, **584**, 1008

Hays, E., Cheung, C. C. & Ciprini, S. (Fermi/LAT collaboration) 2013, *ATel 5302*

Hartmann, J. 1926, *Astr.Nach*, **226**, 203

Hauschildt, P. H., Wehrse, R., Starrfield, S., Shaviv, G. 1992, *ApJ*, **393**, 307

Hauschildt, P. H., Starrfield, S., Shore, S. N., Allard, F. & Baron, E. 1995, *ApJ*, **447**, 829

Herbig, G. H. 1995, *ARA&A*, **33**, 19

Hernanz, M. & Sala, G. 2002, *Science*, **298**, 393

Hernanz, M. & Tatischeff, V. 2012, *Balt.Astr.*, **21**, 62

Hillebrandt, W. & Niemeyer, J. C. 2000, *ARA&A*, **38**, 191

Hutchings, J. B. 1970, *PASP*, **82**, 603

Hutchings, J. B. 1972, *MNRAS*, **158**, 177

Iben, I., Jr. 1991, *ApJS*, **76**, 55

Iijima, T. 2012, *A&A*, **544**, A26

Jenkins, E. B. 1986, *ApJ*, **304**, 739

Jenkins, E. B. & Tripp, T. M. 2006, *ApJ*, **637**, 548

José, J. 2010, *PoS*, **NIC XI**, 050

José, J. & Hernanz, M. 1998, *ApJ*, **494**, 680

José, J. & Shore, S. N. 2008, in *Classical Novae*, 2nd Ed. (Eds. Bode, M. F. & Evans, A.) Cambridge University Press, Chapter 6

Joy, A. H. 1943, *PASP*, **55**, 283

Kalberla, P. M. W. et al. 2010, *A&A*, **512**, A14

Kato, M. & Hachisu, I. 1994, *ApJ*, **437**, 802

Krautter, J. 2008, in *Classical Novae*, 2nd Ed. (Eds. Bode, M. F. & Evans, A.) Cambridge University Press, Chapter 10

Kuulkers, E. et al. 2011, *ATel 3285*

Law, W. Y. & Ritter, H. 1983, *A&A*, **123**, 33

Lyke, J. et al. 2003, *AJ*, **126**, 993

Leavitt, H. S. & Pickering, E. C. 1913, *Harvard College Obs. Circ.*, **179**, 1

McLaughlin, D. B. 1935, *Publ.AAS*, **8**, 145

McLaughlin, D. B. 1942, *ApJ*, **95**, 428

McLaughlin, D. B. 1954, *ApJ*, **119**, 124

Morton, D. C. 2003, *ApJS*, **149**, 205

Munari, U., Dallaporta, S. & Valisa, P. 2012, *ATel 4320*

Munari, U. & Zwitter, T. 1997, *A&A*, **318**, 269

Nelson, T. et al. 2012, *ATel 4590*

O'Brien, T. J. & Bode, M. 2008, in *Classical Novae*, 2nd Ed. (Eds. Bode, M. F. & Evans, A.) Cambridge University Press, Chapter 12

O'Brien, T. J. et al. 2012, *ATel 4408*

Ögelman, H., Beuermann, K., & Krautter, J. 1984, *ApJ*, **287**, L31

Osterbrock, D. E., & Ferland, G. J. 2006, *Astrophysics of Gaseous Nebulae and Active Galactic Nuclei*, 2nd edition (University Science Books)

Paczynski, B. 1971, *ARA&A*, **9**, 183

Patterson, J. et al. 2013, *arXiv* **1303.0746**

Payne-Gaposchkin, C. H. 1957, *The Galactic Novae* (North-Holland Pub. Co.; Interscience Publishers)

Paresce, F., Livio, M., Hack, W. & Korista, K. 1995, *A&A*, **299**, 823

Defense Atomic Support Agency, Project Officer's Interim Report #ADA955694 1992, *STARFISH Prime*

Sahman, D. I. et al. 2013, *MNRAS*, **433**, 1588

Schaefer, B. E. 2005, *ApJ*, **621**, L53

Schaefer, B. E. 2010, *ApJS*, **187**, 275

Schaefer, B. E., Pagnotta, A. & Shara, M. M. 2010, *ApJ*, **708**, 381

Schatzman, E. 1951, *Ann.Astrophys.*, **14**, 294

Schwarz, G. J. 2002, *ApJ*, **577**, 940

Schwarz, G. J., Shore, S. N., Starrfield, S. & Vanlandingham, K. 2007, *ApJ*, **657**, 453

Schwarz, G. J. et al. 2001, *MNRAS*, **320**, 103

Schwarz, G. J. et al. 2011, *ApJS*, **197**, 31

Selvelli, P., Cassatella, A., Gilmozzi, R. & González-Riestra, R. 2008, *A&A*, **492**, 787

Selvelli, P., González-Riestra, R., Gilmozzi, R. & Cassatella, A. 2010, *MmSAI*, **81**, 388

Sembach, K. R. & Savage, B. R. 1992, *ApJS*, **83**, 147

Shara, M. M. et al. 1997, *AJ*, **114**, 258

Shara, M. M., Moffat, A. F. J., Williams, R. E., & Cohen, J. G. 1989, *ApJ*, **337**, 720

Shore, S. N. 2008, in *Classical Novae*, 2nd Ed. (Eds. Bode, M. F. & Evans, A.) Cambridge University Press, Chapter 9

Shore, S. N. et al. 2003, *AJ*, **125**, 1507

Shore, S. N. et al. 2012, *A&A*, **540**, 55

Shore, S. N. et al. 2013a, *A&A*, **549**, A140

Shore, S. N. et al. 2013b, *A&A*, **553**, A123

Shore, S. N. et al. 2013c, *ATel 5282*

Shore, S. N., Augusteijn, T., Ederoclite, A., & Uthas, H. 2011, *A&A*, **533**, L8

Shore, S. N., Kenyon, S. J., Starrfield, S. & Sonneborn, G. 1996, *ApJ*, **456**, 717

Shore, S. N., Sonneborn, G., Starrfield, S., Riestra-Gonzalez, R. & Ake, T. B. 1993, *ApJ*, **106**, 2408

Shore, S. N., Starrfield, S., Ake, T. B. & Hauschildt, P. H. 1997, *ApJ*, **490**, 393

Shore, S. N., Starrfield, S. & Sonneborn, G. 1996, *ApJ*, **463**, L21

Sokoloski, J. L, Crotts, A. P. S., Lawrence, S. & Uthas, H. 2013, *ApJ*, **770**, L33

Spitzer, L. Jr. 1978, *Physical Processes in the Interstellar Medium*, (John Wiley & Sons)

Starrfield, S., Sparks, W. M. & Truran, J. W. 1986, *ApJ*, **303**, L5

Starrfield, S., Truran, J. W., Sparks, W. M. & Kutter, G. S. 1972, *ApJ*, **176**, 169

Starrfield, S. in *Realm of Interacting Binary Stars* (Dordrecht: Kluver), editors Sahade, J., McClusky, G. & Kondo, Y. 1993, **209**

Strope, R. J., Schaefer, B. E. & Henden, A. A. 2010, *AJ*, **140**, 34

Tatischeff, V.& Hernanz, M. 2007, *ApJL*, **663**, L101

Unsöld, A., Struve, O. & Elvey, C. T. 1930, *Zs.Ap.*, **1**, 314

Uthas, H. 2011, Ph. D. thesis (University of Southampton)

Uthas, H., Knigge, C. & Steeghs, D. 2010, *MNRAS*, **409**, 237

Vanlandingham, K. M., Schwarz, G. J., Shore, S. N. & Starrfield, S. 2001, *ApJ*, **121**, 1126

Vanlandingham, K. M., Schwarz, G. J., Shore, S. N., Starrfield, S. & Wagner, R. M. 2005, *ApJ*, **624**, 914

Waagan, E., Linnolt, M. & Pearce, A. 2011, *IAUC 9205*

Walker, M. F. 1954, *PASP*, **66**, 230

Walter, F. M., Battisti, A., Towers, S. E., Bond, H. E. & Stringfellow, G. S. 2012, *PASP*, **124**, 1057

Warner, B. 2002, in *Classical Nova Explosions*, editors Hernanz, M. & José, J., *AIP Conf.Proc.*, **637**, 3

Warner, B. 2008, in *Classical Novae*, 2nd Ed. (Eds. Bode, M. F. & Evans, A.) Cambridge University Press, Chapter 2

Welty, D. E. & Fowler, J. R. 1992, *ApJ*, **393**, 193

Williams, R. E. 1982, *ApJ*, **261**, 170

Williams, R. E. 1992, *AJ*, **104**, 725

Williams, R. E. 2012, *AJ*, **144**, 98

Williams, R. E., Mason, E., Della Valle, M. & Ederoclite, A. 2008, *ApJ*, **685**, 451

Williams, R. E., Phillips, M. M. & Hamuy, M. 1994, *ApJS*, 90, 297

Zwicky, F. 1936, *PASP*, **48**, 191